Quantum magnetism probed with muon-spin relaxation

Andrew J. Steele
Christ Church

a thesis submitted for the degree of

Doctor of Philosophy

University of Oxford
Trinity Term 2011

Quantum magnetism probed with muon-spin relaxation

Andrew J. Steele
Christ Church, Oxford
Trinity term 2011

Abstract of thesis submitted for the degree of Doctor of Philosophy

This thesis presents the results of muon-spin relaxation (μ^+SR) studies into magnetic materials, and demonstrates how these results can be exploited to quantify the materials' low moments and reduced dimensionality.

Dipole-field simulations, traditionally used to estimate likely muon sites within a crystal structure, are described. A novel Bayesian approach is introduced which allows bounds to be extracted on magnetic moment sizes and magnetic structures—previously very difficult using μ^+SR—based on reasonable assumptions about positions in which muons are likely to stop. The simulations are introduced along with relevant theory, and MμCalc, a platform-independent program which I have developed for performing the calculations is described.

The magnetic ground states of the isostructural double perovskites Ba_2NaOsO_6 and Ba_2LiOsO_6 are investigated with μ^+SR. In Ba_2NaOsO_6 long-range magnetic order is detected via the onset of a spontaneous muon-spin precession signal below $T_c = 7.2(2)$ K, while in Ba_2LiOsO_6 a static but spatially-disordered internal field is found below 8 K. Bayesian analysis is used to show that the magnetic ground state in Ba_2NaOsO_6 is most likely to be low-moment ($\approx 0.2\mu_B$) ferromagnetism and not canted antiferromagnetism. Ba_2LiOsO_6 is antiferromagnetic and a spin-flop transition is found at 5.5 T. A reduced osmium moment is common to both compounds, probably arising from a combination of spin–orbit coupling and frustration.

Results are also presented from μ^+SR investigations concerning magnetic ordering in several families of layered, quasi–two-dimensional molecular antiferromagnets based on transition metal ions such as $S = \frac{1}{2}$ Cu^{2+} bridged with organic ligands such as pyrazine. μ^+SR allows us to identify ordering temperatures and study the critical behaviour close to T_N, which is difficult using conventional probes. Combining this with measurements of in-plane magnetic exchange J and predictions from quantum Monte Carlo simulations allows assessment of the degree of isolation of the 2D layers through estimates of the effective inter-layer exchange coupling and in-layer correlation lengths at T_N. Likely metal-ion moment sizes and muon stopping sites in these materials are identified, based on probabilistic analysis of dipole-fields and of muon–fluorine dipole–dipole coupling in fluorinated materials.

Acknowledgements

Thanks are due to my supervisor, **Stephen Blundell**, for his wisdom in helping me to find the right trees to bark up; my officemates in Room 104, **Tom Lancaster** and **Paul Goddard**, for many useful discussions (and many entertaining but useless ones); the muon posse for making experiments (more) bearable: **Francis Pratt** (especially for filling up The Beast at midnight), **Isabel Franke** (who deserves particular mention for tolerating an entire *aller-retour* by train to Switzerland and fortnight in Beijing), **Jack Wright** (for advice on making the perfect bacon sandwich) and **Peter 'Peter Baker' Baker** (and his impossibly strong hands); the skilled synthesisers of samples for this thesis, **Jamie Manson**, **John Schleuter** and the magic-fingered **Prabhakaran**; **Bill Hayes**, for tea-time stories, wise words and proofreading; my corridormates, for countless distractions and occasional assistance: **Graeme Johnstone** (and his green laser), **Alice Taylor** (and her green logbook of 'Friday experiments'), **Peter 'Babbers' Bumkevich** (in Soviet Russia, cups hide you) **Saman Ghannadzadeh** (particularly for help with pulsed-field measurements), **Heather Lewtas** (as the maiden user of MμCalc), **Johannes Möller** (for proofreading and bug-finding), **Ben Williams** and **Stephen Gaw**; me mates **Tom Fuller** (the other Headline Superhero), **Rebekah Smith** and **Elizabeth Tidy**; the parents who engendered me, **Nick and Louise Steele**; and finally, **Rosalind West**, who has kept me insane throughout, and looks sweet upon the seat of a bicycle made for two.

No thanks are due to **the PPMS**, without whose ^{3}He insert this thesis would have been completed several months sooner.

Publications

[1] Andrew J. Steele, Peter J. Baker, Tom Lancaster, Francis L. Pratt, Isabel Franke, Saman Ghannadzadeh, Paul A. Goddard, William Hayes, D. Prabhakaran and Stephen J. Blundell. Low-moment magnetism in the double perovskites Ba_2MOsO_6 (M = Li, Na). *Physical Review B* **84**, 144416 (2011). DOI:10.1103/PhysRevB.84.144416 arXiv:1103.1039.

[2] Tom Lancaster, Francis L. Pratt, Stephen J. Blundell, Andrew J. Steele, Peter J. Baker, Jack D. Wright, Isao Watanabe, Randy S. Fishman and Joel S. Miller. Local magnetism in the molecule-based metamagnet $[Ru_2(O_2CMe)_4]_3[Cr(CN)_6]$ probed with implanted muons. *Physical Review B* **84**, 092405 (2011). DOI:10.1103/PhysRevB.84.092405.

[3] Andrew J. Steele, Tom Lancaster, Stephen J. Blundell, Peter J. Baker, Francis L. Pratt, Chris Baines, Marianne M. Conner, Heather I. Southerland, Jamie L. Manson and John A. Schlueter. Magnetic order in quasi–two-dimensional molecular magnets investigated with muon-spin relaxation. *Physical Review B* **84**, 064412 (2011). DOI:10.1103/PhysRevB.84.064412 arXiv:1104.3505.

[4] Jamie L. Manson, Saul H. Lapidus, Peter W. Stephens, Peter K. Peterson, Kimberly E. Carreiro, Heather I. Southerland, Tom Lancaster, Stephen J. Blundell, Andrew J. Steele, Paul A. Goddard, Francis L. Pratt, John Singleton, Yoshimitsu Kohama, Ross D. McDonald, Rico E. Del Sesto, Nickolaus A. Smith, Jesper Bendix, Sergei A. Zvyagin, Jinhee Kang, Changhoon Lee, Myung-Hwan Whangbo, Vivien S. Zapf and Alex Plonczak. Structural, electronic, and magnetic properties of quasi-1D quantum magnets $[Ni(HF_2)(pyz)_2]X$ (pyz = pyrazine; $X = PF_6^-, SbF_6^-$) exhibiting Ni–FHF–Ni and Ni–pyz–Ni spin interactions. *Inorganic Chemistry* **50**, 13, 5990–6009 (2011). DOI:10.1021/ic102532h.

[5] Jamie L. Manson, Michelle L. Warter, John A. Schlueter, Tom Lancaster, Andrew J. Steele, Stephen J. Blundell, Francis L. Pratt, John Singleton, Ross D. McDonald, Changhoon Lee, Myung-Hwan Whangbo and Alex Plonczak. $[Cu(HF_2)_2(pyrazine)]_n$: a rectangular antiferromagnetic lattice with a spin exchange path made up of two different FHF^- bridges. *Angewandte Chemie International Edition* **50**, 7 (2011). DOI:10.1002/anie.201006653.

[6] Michael J. Pitcher, Tom Lancaster, Jack D. Wright, Isabel Franke, Andrew J. Steele, Peter J. Baker, Francis L. Pratt, William Trevelyan Thomas, Dinah R. Parker, Stephen J. Blundell and Simon J. Clarke. Compositional

control of the superconducting properties of LiFeAs. *Journal of the American Chemical Society* **132**, 30, 10467–10476 (2010). DOI:10.1021/ja103196c.

[7] Tom Lancaster, Stephen J. Blundell, Francis L. Pratt, Isabel Franke, Andrew J. Steele, Peter J. Baker, Zaher Salman, Christopher Baines, Isao Watanabe, Stefano Carretta, Grigore A. Timco and Richard E. P. Winpenny. Relaxation of muon spins in molecular nanomagnets. *Physical Review B* **81**, 140409 (2010). DOI:10.1103/PhysRevB.81.140409.

[8] Dinah R. Parker, Matthew J. P. Smith, Tom Lancaster, Andrew J. Steele, Isabel Franke, Peter J. Baker, Francis L. Pratt, Michael J. Pitcher, Stephen J. Blundell and Simon J. Clarke. Control of the competition between a magnetic phase and a superconducting phase in cobalt-doped and nickel-doped NaFeAs using electron count. *Physical Review Letters* **104**, 057007 (2010). DOI:10.1103/PhysRevLett.104.057007.

[9] Jamie L. Manson, Kevin H. Stone, Heather I. Southerland, Tom Lancaster, Andrew J. Steele, Stephen J. Blundell, Francis L. Pratt, Peter J. Baker, Ross D. McDonald, Pinaki Sengupta, John Singleton, Paul A. Goddard, Changhoon Lee, Myung-Hwan Whangbo, Michelle M. Warter, Charles H. Mielke and Peter W. Stephens. Characterization of the antiferromagnetism in $Ag(pyz)_2(S_2O_8)$ (pyz = pyrazine) with a two-dimensional square lattice of Ag^{2+} ions. *Journal of the American Chemical Society* **131**, 13, 4590–4591 (2009). DOI:10.1021/ja9005223.

Contents

Chapter 1

Introduction

Magnetism is a field encompassing profound fundamental questions and cutting-edge technological applications. In the absence of a reliable universal description of the bulk behaviour of atoms in crystalline solids, empirical research into magnetic materials continues to be of great importance. Furthermore, the limits on our understanding inevitably mean that future technological developments may well arise at least partly serendipitously, lending further weight to the case for a wealth and diversity of experimentation.

This thesis concentrates on a selection of magnetic materials with unusual properties, ranging from the strangely weak magnetism in a pair of osmium compounds, to the quasi–low-dimensional magnetism in molecular magnetic systems, where the magnetic interactions in three-dimensional crystals are significantly stronger in two-dimensional planes than they are between those planes. Molecular magnetism in particular offers a rich playground for both fundamental physicists and aspiring technologists: based on the complex chemistry of carbon, molecular materials can be created with an increasing degree of control, iterating towards bespoke design of magnets to test specific theories, or to dovetail precisely into desired applications.

The unifying theme of this thesis is the study of these novel materials using muon-spin relaxation, or μ^+SR. Muons are short-lived exotic particles rather like heavy, positively-charged electrons, and their use as probes in magnetic systems provides unique insight into the physics of many materials. Muons can be created fully spin-polarised, and embedding them within a material allows its local properties to be studied by following how the muon-spin relaxes during its brief existence. One of the chief difficulties with μ^+SR is that where exactly the muon will choose to embed is *a priori* unknown, making quantitative interpretation of some of the results impossible. However, work in this thesis seeks to partially circumvent this restriction by making reasonable assumptions about where a muon is *likely* to sit, and consequently making probabilistic estimates of magnetic moments or structures.

1.1 Thesis structure

Chapter 2, Muon-spin rotation and relaxation: The μ^+SR technique is described, providing background together with a brief overview of theoretical and experimental considerations. Aspects relevant to this thesis are emphasised.

Chapter 3, Dipole-field simulation: Dipole-field simulations for locating muon sites are explained, along with the mathematical tools underpinning them (Ewald summation, magnetic propagation vectors). A novel Bayesian method allowing muons to be used to extract bounds on magnetic properties is introduced.

Chapter 4, Low-moment magnetism in Ba_2MOsO_6 (M = Li, Na): A pair of unusual osmate compounds are investigated, with μ^+SR results being used to ascertain the magnitude of probable low magnetic moments in both.

Chapter 5, Introduction to two-dimensional molecular magnetism: Introductory material is provided for the following two chapters, introducing two-dimensional magnetism and the molecular compounds which we will use as model systems to probe it.

Chapter 6, Quasi–two-dimensional molecular magnets $[Cu(HF_2)(pyz)_2]X$: Magnetism in a family of copper-based molecular compounds is explored with μ^+SR, with a combination of Fμ oscillations and Bayesian dipole field simulations being used to extract the moments on the copper ions.

Chapter 7, Other quasi–two-dimensional molecular magnets: A short review of related two-dimensional molecular magnets investigated with μ^+SR is provided.

Chapter 2

Muon-spin rotation and relaxation

In *muon-spin rotation and relaxation* (known together as μ^+SR) [1] we take spin-polarised muons and fire them into a sample of interest, and the time-evolution of their spins is then monitored. μ^+SR is often compared to nuclear magnetic resonance (NMR) or electron spin resonance (ESR), with which it was named in analogy. However, a fortunate accident of nature, the parity-violating weak interaction, allows muons to be created in fully spin-polarised ensembles, and removes the requirement for a radio-frequency or microwave pulse to perturb the system to allow a measurement to be made. Thus, it is incorrect to refer to conventional μ^+SR as a resonance experiment, although there does exist a technique known as *muon-spin resonance*, another μ^+SR, which does employ electromagnetic pulses to excite spins of muons, or those in the sample [2, 3, 4].

In the following, I describe the principles of a μ^+SR experiment: the muon is introduced in Sec. 2.1; then, the experimental method is explored in Sec. 2.2, from production of the particles, through guiding to and implantation in the sample, to decay, and then detection of the decay products. The idealised experimental set-up is laid out in 2.3; this is followed by an overview of the kinds of relaxation functions used in this thesis, given in Sec. 2.4; and finally, some practical considerations are given in Sec. 2.5.

Full reviews of μ^+SR can be found in Refs. 1, 5, 6, 7, 8.

2.1 The muon

Muons are charged leptons—elementary particles belonging to the same family as electrons. The muon's properties are identical to those of the electron, except that it is around 200 times heavier; like the electron, its antimatter and matter incarnations carry a charge $\pm e$, respectively, and both carry a spin $S = \frac{1}{2}$. It is unstable, with a mean lifetime of 2.2 µs, making the muon the longest-lived unstable subatomic particle with the exception of the neutron; the muon lifetime exceeds that of pions or kaons, the next most stable subatomic particles, by one hundred times [9]. Its properties are summarised in 2.1. The only practical comparable

property	value
mass, m	1.8835×10^{-28} kg
	$105.66\,\mathrm{MeV/c^2}$
	$207 m_\mathrm{e}$
	$0.11 m_\mathrm{p}$
charge, q	$+1.602 \times 10^{-19}$ C
	$+e$
spin, S	$1/2$
magnetic moment, μ	$4.4904 \times 10^{-26}\,\mathrm{J\,T^{-1}}$
	$0.004\,88 \mu_\mathrm{B}$
	$8.891 \mu_\mathrm{N}$
gyromagnetic ratio, γ	$135.53\,\mathrm{MHz\,T^{-1}}$
mean lifetime, τ	2.197 µs

Table 2.1: The properties of the positive muon, μ^+. In the table, c is the speed of light, m_e is the electron mass, m_p is the proton mass, e is the elementary charge, μ_B is the Bohr magneton and μ_N is the nuclear magneton.

	γ	$\mathrm{e^-}$	μ^+	n	$^8\mathrm{Li^+}$
m	0	m_e	$207 m_\mathrm{e}$	$1840 m_\mathrm{e}$	$14\,600 m_\mathrm{e}$
q	0	$-e$	$+e$	0	$+e$
S	1	$1/2$	$1/2$	$1/2$	2
μ	0	$-1.0011 \mu_\mathrm{B}$	$4.88 \times 10^{-3} \mu_\mathrm{B}$	$-1.713 \times 10^{-3} \mu_\mathrm{B}$	$9.02 \times 10^{-4} \mu_\mathrm{B}$
γ	0	$28.02\,\mathrm{GHz\,T^{-1}}$	$135.5\,\mathrm{MHz\,T^{-1}}$	$183.3\,\mathrm{MHz\,T^{-1}}$	$6.26\,\mathrm{MHz\,T^{-1}}$
τ	∞	$> 4.6 \times 10^{26}$ y	2.197×10^{-6} s	885 s	1.2 s

Table 2.2: The properties of the positive muon, μ^+, compared to other common probes in condensed matter physics, the neutron, n, electron, $\mathrm{e^-}$, photon, γ, and $^8\mathrm{Li^+}$, an ion commonly used in βNMR [10]. Values are quoted in terms of the electron mass m_e, the elementary charge e, and the Bohr magneton μ_B. Data are from Refs. 9, 11.

probes for condensed matter physics are light atomic nuclei which undergo β-decay [10], for example ^{8}Li. However, these ions can only be implanted near the surface and constitute a significantly larger defect in a crystal than a muon [10]. A review of the properties of common condensed matter probes is available in Table 2.2.

Muons are produced naturally by interactions between high-energy particles with the atomic nuclei of gases in the upper atmosphere. In fact, there are around 10 000 muons passing through every square metre of the Earth's surface every minute [9], and consequently several passing through you every second as you read this. These natural muons—dubbed *cosmic rays*—were the first to be observed in 1936 [12]. The fact that so many survive the journey from their production high in

the atmosphere at around 15 km altitude [9] (roughly 50 μs at the speed of light, and thus over 20 muon lifetimes), is a demonstration of relativistic time-dilation. This was confirmed in 1963, by identical muon-counting experiments atop Mount Washington and near sea level in Cambridge, Massachusetts, which found that the ratio of count rates was commensurate with the predictions of relativity [13].

2.2 The μ⁺SR experiment

The first μ⁺SR experiment [14] was performed in 1957. Its purpose was not to examine a condensed matter system, but to test the Lee–Yang proposal that the weak interaction violated parity [15]. This further corroborated the proposal, and demonstrated the principles that underpin all muon spectroscopy: without parity violation, we could neither produce our spin-polarised muons in the first place, nor glean anything useful about them from their decay.

Facilities producing muons for condensed matter exist at only a few locations around the world. The work contained in this thesis was performed primarily at ISIS, the synchrotron at the Rutherford Appleton Lab, Didcot, UK, and the Swiss Muon Source (SμS) fed by the cyclotron at the Paul Scherrer Institut, Villigen, Switzerland.

The following section outlines the principles of a μ⁺SR experiment, starting with the particle physics processes which lead to muon production, then describing successively the processes by which a muon is guided to the sample, embeds within it, interacts once embedded, and finally, the physics of muon decay which allows us to make measurements of its interactions.

2.2.1 Muon production

The mass of the muon makes it impossible to produce one by nuclear fission, fusion or decay; the only way to produce muons is in a particle accelerator. A beam of high-energy protons is collided with a thin production target of a light element (taking ISIS as an example, 800 MeV protons are collided with graphite). Pions are then produced by collision between the protons and nucleons in the target's atomic nuclei by processes such as

$$\begin{aligned} \mathrm{p} + \mathrm{p} &\rightarrow \mathrm{p} + \mathrm{n} + \pi^{+}, \\ \mathrm{p} + \mathrm{n} &\rightarrow \mathrm{p} + \mathrm{p} + \pi^{-}, \end{aligned} \tag{2.1}$$

where p denotes proton, n neutron and $\pi^{\pm}$ denote the positive and negative pion, respectively. This process stops a few percent of the protons, leaving the rest of the beam largely undeviated such that it can be used for other applications, often neutron production, downstream.

Charged pions comprise a down quark and an up antiquark, or vice-versa. They are the lightest charged hadrons, and consequently must decay via the weak interaction into leptons, which they do with a mean lifetime 26 ns. Conservation of

lepton number requires that an appropriate neutrino (ν) be produced, giving rise to the reaction

$$\pi^+ \rightarrow l^+ + \nu_l \,, \tag{2.2}$$

where $l = \mu$, e; a muon or an electron. An accident of the weak interaction and conservation of angular momentum results in $l = \mu$ being preferred over $l = e$ with a ratio of approximately 8000:1. A further upshot of conserving angular momentum is that the muons produced are fully spin-polarised.

The muons used for experiments in this thesis are positively charged antimuons. Negative muons μ^- usually fall into low atomic orbitals in extreme proximity to atomic nuclei. An order of magnitude estimate can be made by evaluating the Bohr radius with the muon mass substituted for the electron mass,

$$a_\mu \approx \frac{4\pi\epsilon_0\hbar^2}{m_\mu e^2} = a_0\frac{m_e}{m_\mu} = 26\,\text{pm} \tag{2.3}$$

where ϵ_0 is the permittivity of free space, $\hbar$ is the reduced Planck constant, m_e is the electron mass and e is the fundamental electric charge. The muonic Bohr radius a_μ is then related to the electronic Bohr radius a_0 by the ratio of electron and muon masses. This results in a high probability density very near to the nucleus, and is a useful probe of nuclear charge distribution, or can be used to decrease the electric potential barrier which inhibits nuclear fusion [16]. However, condensed matter physics is more concerned with electronic behaviour, and hence it is better to use μ^+ which come to rest in areas of high electron density.

Most muons used in condensed matter are so-called *surface muons*, produced from pions at rest in the surface of the production target. Conservation of energy and momentum allows the kinetic energy E_k of the muon to be simply evaluated:

$$E_k = \left(\frac{m_\pi^2 - m_\mu^2}{2m_\pi}\right)c^2 = 4.119\,\text{MeV}, \tag{2.4}$$

where $m_{\pi,\mu}$ are the pion and muon masses, respectively, and c is the speed of light. The momentum of these surface muons is $p_{\text{surface}} = 29.79\,\text{MeV}/c$. Alternatively, production can proceed via the *decay channel*, where pions which decay in flight are utilised to create muons with higher energy. This gives rise to a higher-energy beam which penetrates deeper into material before stopping, but with a broader energy and momentum distribution (typically $70 < p_{\text{decay}} < 130\,\text{MeV}/c$ [6]), and spin-polarisation $< 100\%$.

2.2.2 Muon beams

Muons are guided from the production target to the sample down an evacuated beampipe by a series of electromagnetic devices. As well as correctly guiding muons, it is important to discard as many other particles which may be produced at

the target as possible; this reduces both spurious counts in experimental detectors and sample radiation damage.

Dipole steering magnets are used to alter the course of the muons. Because the g-factor of the muons is very nearly 2 ($g_\mu = 2.002\,332$), magnetic fields rotate the muons' spin and trajectory at very nearly the same rate, ensuring that this manipulation does not affect the relative direction of their spin and motion. The radius of curvature r in a magnetic field B is a function of particle charge q and momentum p,

$$r = \frac{p}{qB}\,. \tag{2.5}$$

This also allows particles with a specific p/q ratio to be selected by placing a slit after the bending magnet, removing all uncharged particles such as neutrons and photons, and all negatively-charged particles such as electrons and negative muons, but positively-charged particles, such as positrons or positive pions, may pass if they have the correct momentum.

Particles can also be selected by velocity using a crossed-field separator, which employs perpendicular electric and magnetic fields. The magnetic field applies a force Bqv perpendicular to both the particle velocity and the magnetic field, whilst the electric field of magnitude E applies a force Eq parallel to its field direction. Particles will continue undeflected if these forces are equal and, since only one depends on velocity, a single value of this is isolated. Applied to a beam in conjunction with momentum selection, positive particles other than muons are removed.

Quadrupole focusing magnets are used to focus a beam travelling with a given momentum in the z-direction along one direction in the xy-plane, whilst defocusing the beam in the remaining perpendicular direction. It is only possible to focus in one dimension in the xy-plane in a single quadrupole, but a series of units with alternating polarity can be used to give a net focussing effect. These can be used to collect muons near the production target, and to focus the beam onto the sample.

There are sometimes multiple instruments attached to one beamline, so electromagnetic kickers are used to direct muons to the appropriate apparatus. At ISIS, for example, the muons arrive in a pair of closely-spaced pulses (see Sec. 2.5.2), and a large electric field can be used to deflect the first into one instrument before being rapidly removed for the arrival of the second pulse, allowing it to continue undeflected into a different experimental apparatus.

Electric fields do not couple to spin and consequently only change the muon momentum. This means that the muon direction of travel is rotated with respect to its spin in an electric field. This can be unintentional—a typical beamline with separators and kickers will rotate a muon-spin by a few degrees—or it can be used to rotate the spin with respect to the detector geometry before implantation, in a *spin rotator*. This can be used to alter the experimental geometry, as examined in Sec. 2.3.

2.2.3 Muon stopping processes

The energy of a muon determines its likely penetration into matter. Extremely high-energy muons are very highly penetrating: neutrino detection experiments are often placed several miles underground in order to shield them from spurious events due to cosmic ray muons [17]. Muons used in condensed matter research have a more moderate energy in order that they will stop in samples of typical size $\lesssim 1\,\mathrm{cm}^3$.

The 4 MeV surface muons have a typical stopping range in matter of $110\,\mathrm{mg\,cm}^{-2}$, with a range width of approximately 20% [18]. The processes which bring the muon to a halt occur in several distinct stages. First, over a period of approximately 0.1 ns to 1 ns, the muon is decelerated to an energy of a few keV by ionisation of atoms and scattering with electrons. Then, during a period lasting around a picosecond, the muon rapidly captures and loses successive electrons, forming fleeting muonium states (see Sec. 2.2.4), bringing its energy down to a few eV. Finally, the muon (or muonium) thermalises, shedding almost all of its excess energy and coming to rest. Typical energies required to create a crystal vacancy are significantly larger than muon kinetic energy in the latter stages of its deceleration; the muon comes to rest ~µm from any sample damage it has caused, and these effects can be neglected. Since the stopping processes primarily involve electrostatic interactions, the muon implants with no significant reorientation of its spin. Futher information on these stopping processes can be found in Ref. 19.

The 'surface muon' nomenclature has the potential to be slightly confusing, because it refers to the position of the parent pions on the surface of the production target, rather than to the muon sites in the sample. To enable studies near the surface of samples, or involving films or thin layers, *slow muons* are created [20]. These are manufactured by taking conventional surface muons and reducing their momentum by first stopping them in a moderator, such as frozen argon, followed by subsequent re-acceleration with electric fields. Conversely, if deeper penetration into the sample is required, decay channel muons (see Sec. 2.2.1) are used instead. This can be used, for example, to allow muons to traverse a reinforced pressure cell before coming to rest in the sample contained within it.

2.2.4 Interaction with the sample

The scenario in which μ^+SR lends itself to simplest interpretation is the case of the muon interacting passively with its surroundings. In many magnetic and superconducting samples it is permissible to approximate the muon as an inert probe of local field. Muons possess a magnetic moment, and will therefore undergo Larmor precession in a magnetic field. Since the muon possesses $S = \frac{1}{2}$, it only experiences this simple dipolar coupling to its environment without the added complication of quadrupolar coupling, as seen in many NMR nuclei, or ^{8}Li.

To take the simple example of an ordered ferromagnet with a single muon site, every muon in the ensemble experiences the same single value of magnetic field. This results in a coherent precession of the muon-spins, and is known as muon-spin rotation. In more complex materials, multiple magnetically-inequivalent sites may

	Mu	H	T
mass (m_e)	208	1837	5498
reduced mass (m_e)	0.9952	0.9995	0.9998
Bohr radius (nm)	0.053 17	0.052 95	0.052 93
ionisation energy (eV)	13.540	13.598	13.603

Table 2.3: Comparison of properties of muonium (Mu = μ^+e^-), protium (^{1}H = pe^-) and tritium (^{3}H = T = $pnne^-$), illustrating that muonium can be viewed as a light isotope of hydrogen.

give rise to a number of precession frequencies, or a distribution. For example, in many materials randomly-orientated nuclear moments cause random magnetic fields at muon sites resulting in no coherent precession, but a slow depolarisation of muon spins. Further, fluctuations of the local field in the time domain can give rise to relaxation of the muon ensemble's polarisation caused by anything from critical fluctuations near a phase transition to passing 'magnetic monopoles' in spin-ice [21].

It is also possible for the muon to interact quantum-mechanically with nearby spins. In an ordered magnet, the strength of the exchange interactions and size of electronic spins means that the muon does not perturb the spin system, and simply sees the field it generates. A two-way interaction requires a spin whose coupling to its environment is much weaker, the prototypical example being a fluorine nucleus. Through a quantum-entangled dipole–dipole interaction, the muon enters a bound Fμ state (see Sec. 6.3).

As a positively-charged particle in matter, a further possibility is that the muon can capture an electron in a sample and form a hydrogen-like atom known as muonium (symbol Mu). Though the muon is a lepton, it can be considered a light proton in these circumstances. Since its mass is more than two orders of magnitude greater than an electron, but only nine times less than a proton, the atomic physics of Mu is startlingly similar to H. Some properties of muonium, hydrogen and tritium are compared in Table 2.3. The effects of muonium formation are not examined in detail in this thesis, but an overview can be found in Refs. 5, 22.

2.2.5 Muon decay

The muon decays via the three-body process

$$\mu^+ \rightarrow e^+ + \nu_e + \bar{\nu}_\mu, \tag{2.6}$$

creating a positron (antielectron), plus an electron-neutrino and a muon-antineutrino to conserve lepton number. Like muon production, this too is a weak decay and consequently violates parity. This manifests in the positron being emitted preferentially in the direction of spin of the dying muon—and the positron is the only one of these three particles which we might hope to reliably detect. Unfortunately however, the extra degree of freedom introduced by the third decay product means that this process does not enjoy the simplicity of muon production.

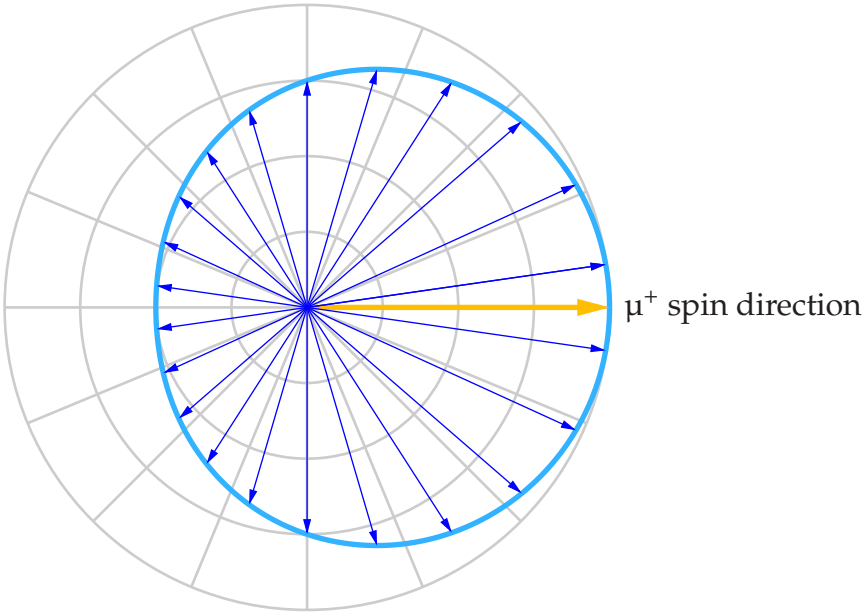

Figure 2.1: A polar plot showing the asymmetric emission directions of the positron in the aftermath of muon decay, averaged over all energies (see text). The thick yellow arrow represents the axis of the muon spin, which is also the most likely direction of positron emission.

The emerging positron can vary in both energy and the angle at which is it emitted. The angle of emission is distributed about the muon spin direction in cardioid form,

$$N(\theta) = N_0(1 + a\cos\theta). \tag{2.7}$$

For the maximum possible positron energy of 52.83 MeV, $a = 1$; integrating over all possible energies, $a = \frac{1}{3}$, leading to the less pronounced angular distribution shown in Fig. 2.1. Nonetheless, this finite asymmetry still allows muon-spin precession to be followed arbitrarily precisely, given enough data.

2.3 Experimental set-up

In order to monitor the time-evolution of muon spin direction, scintillation detectors are set up around the sample to count the outgoing positrons as a function of angle and time. The simplest experimental configuration involves just two detectors: one forward (F) and one backward (B) of the initial muon-spin direction. The difference in count rate between these is then monitored as a function of time, and divided by the total count rate to normalise with respect to the ever-decaying population of muons remaining in the sample. The experimental quantity of interest is then the *positron asymmetry*,

$$A(t) = \frac{N_\mathrm{F} - \alpha N_\mathrm{B}}{N_\mathrm{F} + \alpha N_\mathrm{B}}, \tag{2.8}$$

where α is an empirical constant to take into account any slight inequivalencies between the forward and backward detectors. These can result from efficiency

differences in the scintillators and electronics, asymmetric sample positioning, difference in solid angle coverage of the detectors, and so on. $A(t) \propto p_z(t)$; meaning that the measured quantity, $A(t)$ gives us direct access to the quantity of interest, $p_z(t)$, the component of the muon-spin polarisation along the z-axis of the apparatus. A schematic diagram of this experimental configuration is shown in Fig. 2.2 on the following page.

In an ideal apparatus, the initial asymmetry when all muon spins are polarised towards the F detector would be the energy-integrated value of a from Eq. (2.7), $A(t = 0) = a = \frac{1}{3}$. However, various factors reduce this in reality, including the limited solid-angle coverage of the detectors; the exclusion of low-energy positrons which stop in the sample, cryostat or detector wrappings; and the effects of magnetic field on positron trajectories [23, 24]. In fact, a typical initial asymmetry is around $A(t = 0) = 25\%$.

This configuration is known as the *longitudinal field* or LF configuration, where any magnetic field B_{long} is applied parallel to the initial muon spin direction. (Applying such a longitudinal field is not performed in the experiments featuring in this thesis.) The *zero-field* or ZF configuration is identical, but in the special case of no applied field. If muons were to stop in a sample with which they did not react at all, the 'null' data measured in this geometry would be a flat line at $A(t) = A_0$. In addition to this geometry, there exists the *transverse field*, or TF, configuration in which the field is applied perpendicular to the initial muon spin direction, leading to a precession of the spins around the applied field. This means that the 'null' asymmetry function in an applied field B_{trans} would be a cosine, $A(t) = A_0 \cos \gamma_\mu B_{\text{trans}} t$. In this configuration, a larger number of detectors may be used to track the muon-spin direction as it rotates.

2.4 Relaxation functions

The asymmetry spectra $A(t)$ generated in μ^+SR are typically fitted in the time-domain. The fitting function used is known as a *relaxation function*, and a diversity of forms reflects a diversity of underlying physics. In general, a muon responds to its local magnetic field $\boldsymbol{B}$ by precessing about the component of it transverse to the muon-spin direction with a Larmor frequency given by

$$\omega = \gamma_\mu B \tag{2.9}$$

where $\gamma_\mu = 2\pi \times 135.5\,\text{MHz}\,\text{T}^{-1}$ is the muon gyromagnetic ratio and $B = |\boldsymbol{B}|$ is the magnitude of the magnetic field at the muon site. Semiclassically, we can consider this as the muon-spin precessing at the end of a cone of half-angle θ, where θ is the angle between muon-spin direction and local field direction (see Fig. 2.3). The polarisation of the muon ensemble projected along the z-direction as a function of time will then be given by

$$p_z(t) = \cos^2\theta + \sin^2\theta \cos\left(\gamma_\mu B t\right). \tag{2.10}$$

In this section, we will discuss first the case where the field bathing the muon originates entirely from the behaviour of the sample (Sec. 2.4.1). Then, the effect of

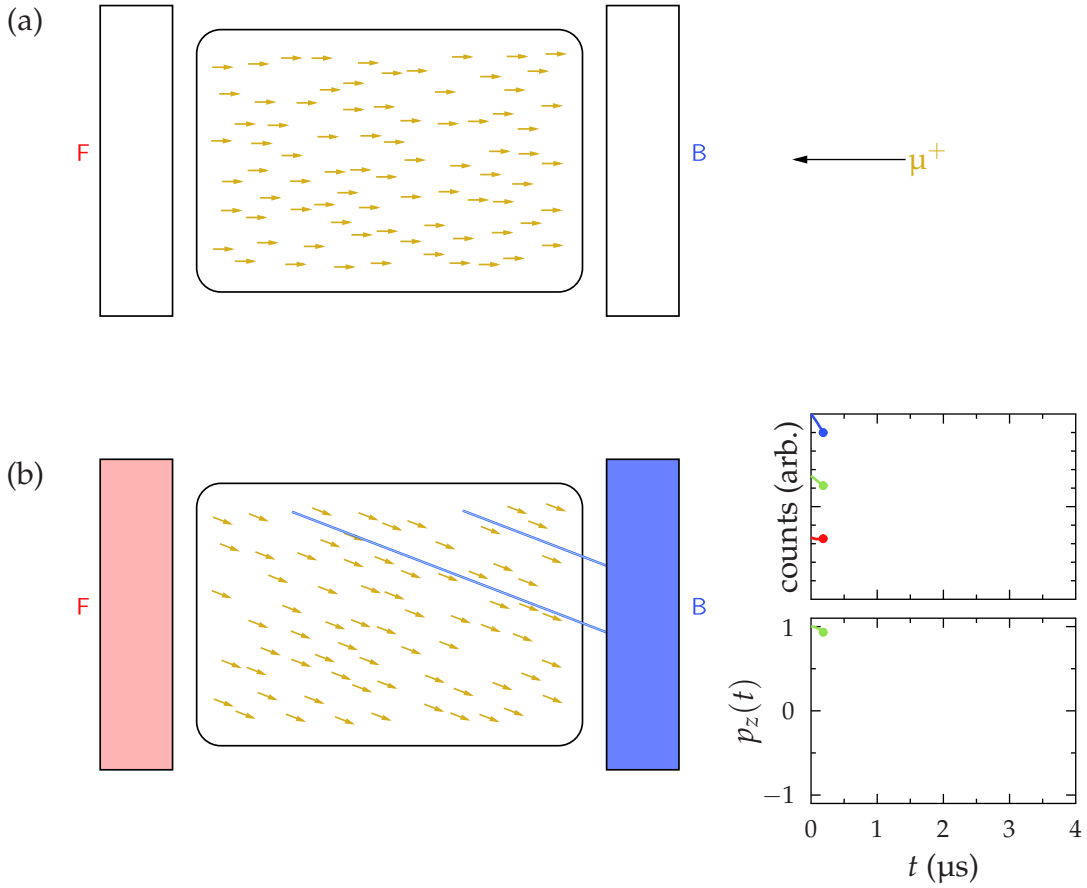

Figure 2.2: Schematic diagram showing a simple μ⁺SR experiment where muons implant in a sample and experience a uniform ***B***-field directed perpendicular to the paper. (a) At $t = 0$, one or more muons are injected into a sample from the right. Their spins, represented by the gold arrows, are directed antiparallel to their linear momentum. The muons implant at random positions throughout the sample. This image shows either a pulse of muons from a pulsed muon source, or the aggregate of many events at a continuous source. The sample is positioned between forward and backward detectors, F and B. (b) Moments later, positrons are being emitted along the direction of muon-spin; these are represented by blue lines. The upper graph on the right shows the raw count rate. This is higher in the backward detector (blue line) than the forward one (red line), with the central green line showing the average count rate. The lower graph then shows the muon polarisation along the z-direction, $p_z(t)$, obtained from Eq. (2.8).

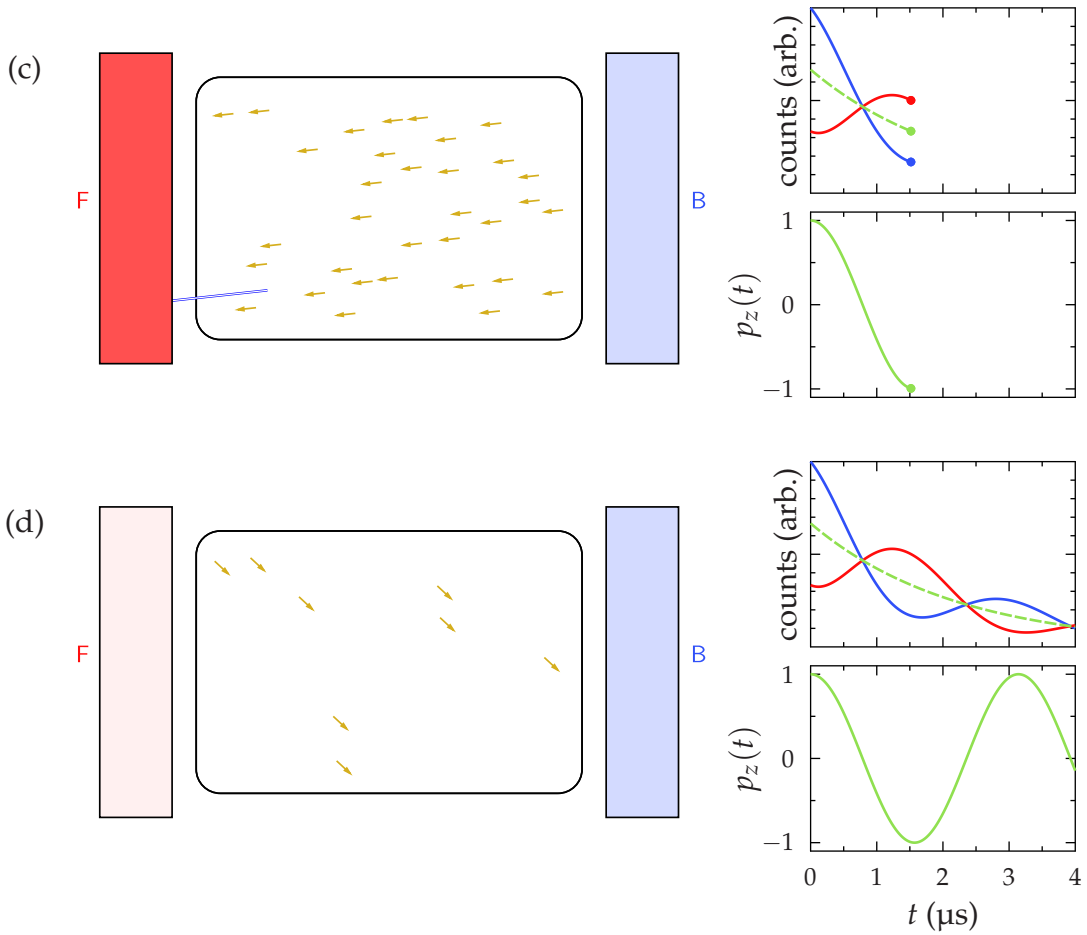

Figure 2.2: (continued) (c) A time nearly $t = \pi/\gamma_\mu B$ later, the muon-spins have precessed through almost 180°, giving rise to more counts in the forward positron detector than the backward one. The central average line has progressed, and it is now easily seen that it reflects the exponential decay of the muon population with $\tau_\mu = 2.2\,\mu s$. The asymmetry line, normalised for this decay, remains cosinusoidal. (d) At late times, only a few muons remain. The complete $A(t)$ trace to $4\,\mu s$ is shown.

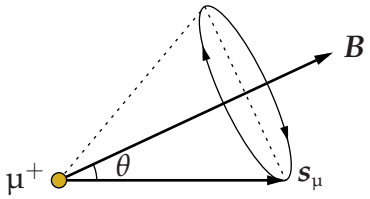

Figure 2.3: The semi-classical picture of a muon-spin, pointing along a direction $\boldsymbol{s}_\mu$, precessing around the local field $\boldsymbol{B}$.

applied magnetic field will be considered. Applying field allows us to explore the phase diagram of the sample, but also has a direct effect on the muons and thus the asymmetry spectra obtained: the case where an external magnetic field is applied perpendicular to the initial muon-spin direction is briefly explored in Sec. 2.4.2.

Fitting muon data in this thesis was performed using the Windows Muon Data Analysis (WiMDA) package [25].

2.4.1 Zero-field

In materials with spontaneous magnetic properties, μ^+SR can be used to probe samples without application of an external field. In an ordered magnet, Eq. (2.10) can give rise to spontaneous precession of the muon ensemble. Single-crystal experiments with muons are not considered in this thesis, and consequently we take a *powder average*, imagining that an infinite number of randomly-aligned crystallites make up the sample under study. This is not a significant experimental hindrance because the precession frequency depends only on the magnitude of the local field, with only the amplitude of that precession depending on the direction. Taking a powder average over Eq. (2.10) yields

$$p_z(t) = \frac{1}{3} + \frac{2}{3}\cos\left(\gamma_\mu B t\right), \tag{2.11}$$

due to the $\frac{1}{3}$ of crystallite orientations in which the local field will lie parallel to the initial muon-spin components. Thus, the onset of magnetic order can be seen by two effects: firstly, the presence of oscillations, and secondly the emergence of a $\frac{1}{3}$*-tail*, a baseline at long times below which the spectra do not relax. An example of spectra above and below a magnetic transition in $[Cu(HF_2)(pyz)_2]BF_4$, a material discussed in Chapter 6, is shown in Fig. 2.4.

For a single muon site which is magnetically equivalent throughout the crystal, this results simply in a cosinusoidal oscillation in asymmetry. In more complex static fields, the resulting asymmetry function is somewhat like a cosine Fourier transform of the local fields at the muon sites, but taking care to perform an appropriate angular average. A simple case which illustrates the importance of angular averaging in μ^+SR spectra is that of a random local field at the muon site, normally-distributed about a mean of zero. This might occur, for example, in a

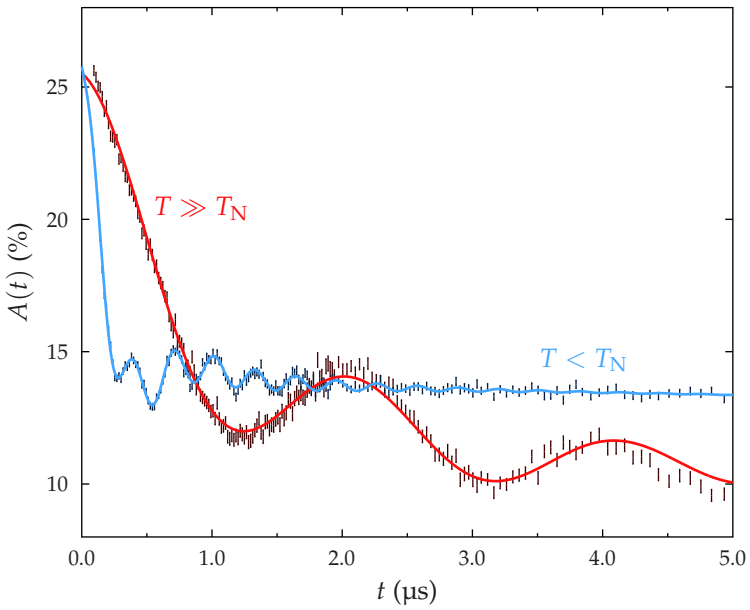

Figure 2.4: Example $A(t)$ spectra with fits above ($T = 25\,\mathrm{K}$) and below ($T = 0.3\,\mathrm{K}$) the magnetic transition temperature $T_N = 1.4\,\mathrm{K}$ for $[Cu(HF_2)(pyz)_2]BF_4$. The two spectra are approximately equal in initial asymmetry, but the presence of oscillations and '$\frac{1}{3}$-tail' observed unambiguously identify the ordered phase. The slow oscillation observed for $T > T_N$ is due to muon–fluorine dipole–dipole oscillations (see Sec. 6.3).

spin-glass. The muon polarisation then follows the *Kubo–Toyabe function*,

$$p_{KT}(t) = \frac{1}{3} + \frac{2}{3}\left(1 - \Delta^2 t^2\right) e^{-\Delta^2 t^2/2}, \tag{2.12}$$

where $\Delta = \sqrt{\gamma_\mu^2 \langle (B - \langle B \rangle^2) \rangle}$ is the *field width* (the second moment of the field distribution, whose mean is $\langle B \rangle$, in frequency units), shown in Fig. 2.5. Note that this is not simply a Gaussian, as a naïve Fourier transform might lead us to imagine, though at early times it is well approximated by one. After an initial depolarisation, with the $p_z(t)$ reaching a minimum at $\Delta t = \sqrt{3}$, the $\frac{2}{3}$ of muon-spin components perpendicular to their local field dephase entirely, leaving the $\frac{1}{3}$-tail of parallel spin components.

Another prototypical relaxation function occurs in materials with an incommensurate magnetic structure, resulting in a field at the muon site which varies sinusoidally with the unit cell in which the muon stops. This distribution of local fields results in the muon relaxation following a Bessel function [26, 27].

As well as static field distributions, the muon ensemble can be relaxed by dynamics present within the sample. This will usually give rise to an exponential relaxation of the form $e^{-\lambda t}$. In the *fast-fluctuation limit*, where $1/\tau \gg \Delta$ (i.e. the fluctuation rate, given as the reciprocal of the correlation time τ, results in much faster depolarisation than the distribution of fields, Δ), then the relaxation rates are expected [28] to vary as $\lambda \propto \Delta^2 \tau$. This is the case in most magnetic materials,

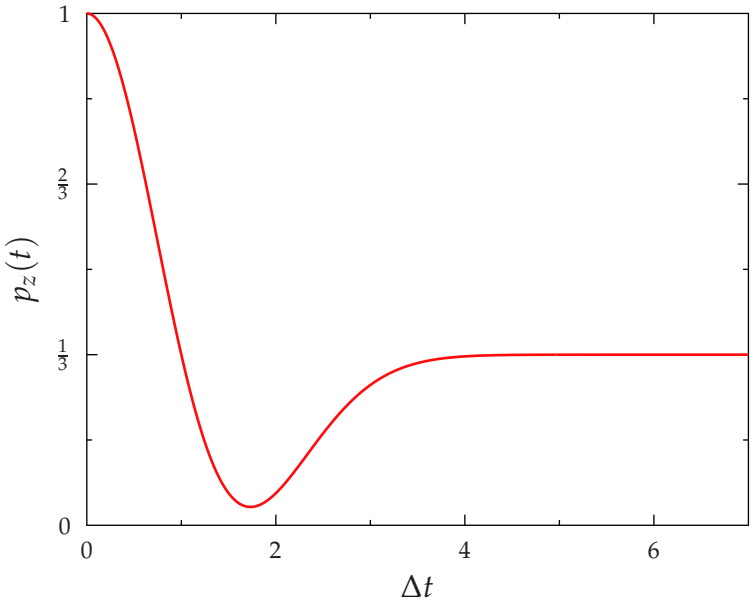

Figure 2.5: The Kubo–Toyabe function in zero field [Eq. (2.12)].

where the effect of variation in field within a set of muon sites is small compared to the fluctuations in those fields caused by the dynamic behaviour of local moments.

2.4.2 Transverse field

As mentioned in Sec. 2.3, the asymmetry function in an applied transverse field (TF), B_{trans}, with muons stopped in an entirely inert sample would be a cosine. In a real sample, the cosine may have its frequency slightly shifted from that which would be expected in the applied field, and is modulated by a relaxing envelope dependent on the physics of the system being probed. This gives rise to the general TF relaxation function

$$A(t) = A_0 \cos(\omega t)\, R(t), \tag{2.13}$$

where A_0 is the initial asymmetry, $\omega \approx \gamma_\mu B_{\text{trans}}$ is the angular frequency of the oscillation, and $R(t)$ is some function describing the relaxation.

In a magnetic system, transverse fields small relative to the internal fields in the sample give rise to complex behaviour. Firstly, we must account for any change in internal field brought about by magnetisation in the sample but, further, these internal fields must be vector-summed with the field applied. In large applied field, the internal fields act as a small correction to the external field and thus, in a powder sample, we can consider the TF relaxation function as a cosine with $\omega = \gamma_\mu B_{\text{trans}}$ and a relaxation governed by the magnitude of the internal fields. This method is used to investigate the B–T phase diagram in a molecular system in Sec. 6.2.

Another typical use of the TF geometry is to probe superconductivity. Type II superconductors below their critical temperature T_c enter the mixed state when an external field $B_{c1}(T) < B < B_{c2}(T)$ is applied. This state is characterised by a vortex lattice of magnetic flux quanta, with a typical lattice spacing of order nm. Since

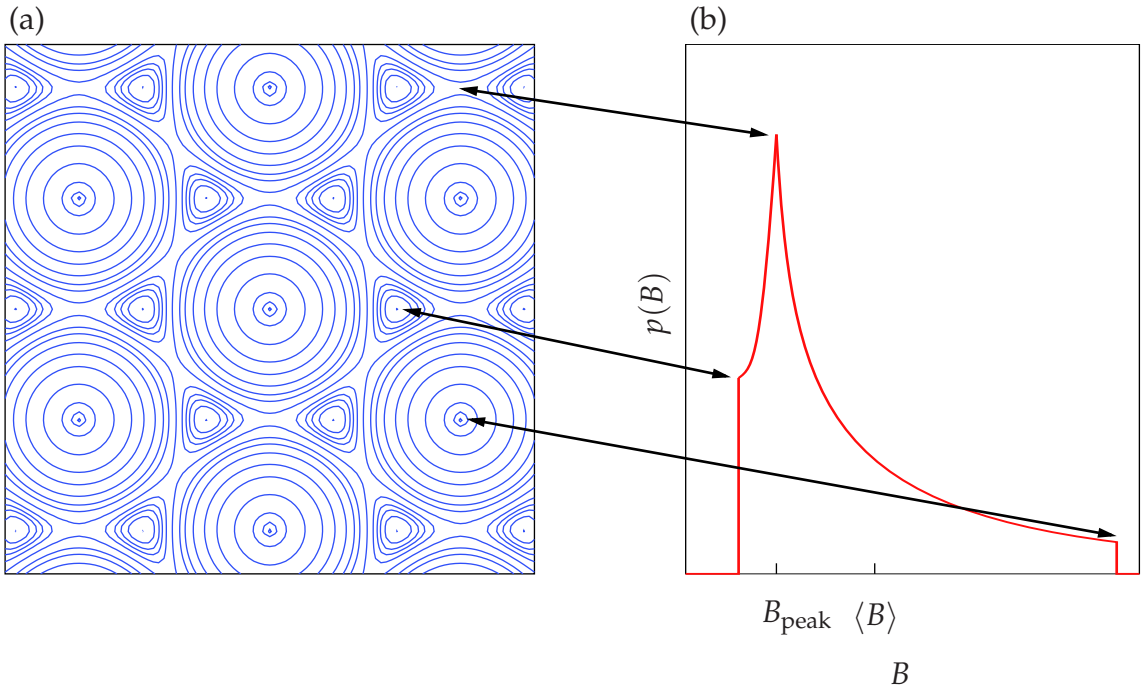

Figure 2.6: (a) A schematic diagram of the magnetic field in the superconducting vortex lattice, and (b) the distribution of fields arising from this. Arrows link corresponding points on the two diagrams: the maximum and minimum fields at the vortex cores and furthest from them, respectively; and the modal field, at an intermediate position. Diagram follows Ref. 1.

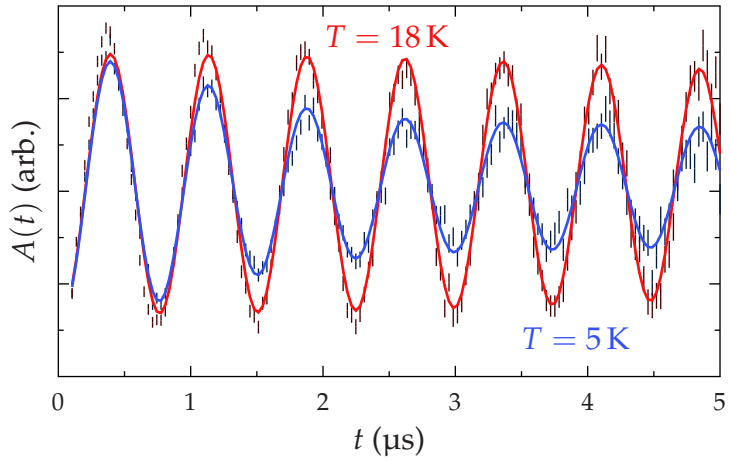

Figure 2.7: μ^+SR spectra for $LiFe_{0.99}Ni_{0.01}As$ above and below the superconducting transition temperature $T_c = 13.4\,\text{K}$ in a transverse field of 10 mT. Relaxation of the spectrum taken at 5 K results from the distribution of local magnetic fields arising from the superconducting vortex lattice. Data taken from Ref. 29.

muons can stop at any set of crystallographically-equivalent sites, they decorate this lattice on a significantly smaller length scale, and can be considered to sample the entire vortex lattice. This results in the muons sampling a distribution of magnetic fields, highest at the centre of the vortices and lowest at positions furthest away from them. Thus, whilst $R(t) \approx 1$ in a sample above the superconducting transition, the asymmetry function below the transition is given by the cosine Fourier transform of the new field distribution. This gives rise to a relaxing cosine which, in general, will have a frequency which differs slightly from the applied B_{trans} by the *diamagnetic shift*. This is shown schematically in Fig. 2.6, and with data taken by the author on Ni-doped LiFeAs in Fig. 2.7.

2.5 Experimental considerations

2.5.1 Continuous beam sources

Muon sources can be divided into two classes: continuous sources, where the muons arrive in a quasi-continuous stream; and pulsed sources (see Sec. 2.5.2). In a continuous source, a single muon is in the sample at any given time. Muons arrive intermittently and implant in the sample. Veto detectors positioned behind the sample can be used to flag up muons which have flown past the sample and not implanted. The clock starts when a muon enters the detection apparatus, and stops when a decay positron is incident on one of the detectors. However, if a second muon arrives before a positron is detected, it is impossible to know which of the two subsequent decay positrons came from which muon, and both events must be discarded.

The requirement that only one muon be present at any given time restricts both the event rate and the low-frequency resolution of a continuous source. Since a muon may arrive and interrupt your experiment, increasing the rate of muon production eventually reduces the event rate of your experiment, because many events must be discarded. Similarly, increasing the time window over which each event is recorded in an attempt to increase the low-frequency resolution also increases the probability that a new muon will arrive and interrupt an event; thus, event rate and low-frequency resolution are in competition with one-another. A further consequence of a continuous source is high background; muons which neither embed in the sample nor set off the veto detector can result in spurious counts, especially at long times. In fact, this sets a practical limit of around 10 µs on experimental counting.

2.5.2 Pulsed sources

A pulsed muon source delivers muons in large bunches rather than individually. All the muons implant in the sample approximately simultaneously, starting the experimental clock, and positron emission is timed with respect to the arrival of the pulse.

The chief disadvantage of a pulsed source is that a resolution limit is imposed on precession frequencies by the width of the pulse. The ambiguity in muon arrival time means that, roughly speaking, if the magnetic field being measured is such that the first muons to arrive have undergone one spin rotation by the time the last muons arrive, then those in between will find themselves at every intermediate stage in the precession, and any signal will be washed out. More precisely, a frequency resolution function can be extracted by taking the Fourier transform of the incoming pulse. In the simplest case of a single broad pulse, a monotonic reduction in signal amplitude occurs up to some cut-off frequency above which muon precession cannot be reliably observed.

In spite of this restriction, it may still be possible to detect a transition to long-range magnetic order where frequencies are too high to resolve. Significant reductions in initial asymmetry below the transition are often observed because a reduced value of $A(t)$ corresponding approximately to the average value of the invisible oscillations is seen. Conversely, asymmetry at long times can increase due to the effect of the $\frac{1}{3}$-tail, described in Sec. 2.4.1. It is also often possible to observe discontinuous variations in relaxation rates with temperature.

The limit on the rate of data acquisition at pulsed sources is imposed by the finite detector *dead time* (often around 10 ns). This is the time after detection of a positron during which further positrons will not be acknowledged. Consequently, rather than using just two detectors as in an idealised μ^+SR experiment, large numbers of individual detectors are used. In LF configuration, these are grouped to act as two highly segmented detectors. For example, the MuSR spectrometer at ISIS has some 64 detectors split into two banks of 32, while the new CHRONUS instrument has 606 individual positron counters [30]!

2.5.3 Sample mounting

Samples are mounted in such a way as to minimise the effect of mounting on the resulting asymmetry spectra. Large samples are usually mounted on a backing plate which will capture those few muons which do not implant in the sample. Small samples will often be mounted in a *flypast* configuration, where the sample is mounted on prongs with no backing; muons which do not implant in the sample thus fly past. At a continuous muon source, a veto counter detects this and discounts any positron detected as a result of this. At a pulsed source, a long flypast tube allows those muons which miss or pass through the sample to decay far from the positron counters. Small samples also sometimes require a quantity of *degrader* to be placed in front of them, to slow the muons to the cusp of stopping before they penetrate the sample, ensuring that they do not pass straight through.

When the sample is mounted on a backing plate, the materials most often used are silver (Ag) and haematite (Fe_2O_3). Silver has very little effect on muons: it is very weakly diamagnetic, does not superconduct under ordinary conditions, and possesses very small nuclear moments ($\sim -0.1\mu_N$). Thus, silver induces neither precession nor depolarisation of the muon spin ensemble. Haematite is sometimes used, for precisely the opposite reason: large, random internal magnetic fields all but instantly depolarise any muons which land in it.

Regardless of experimental geometry, samples are often wrapped in silver (Ag) foil packets. In ZF and LF experiments, samples are normally mounted on silver backing plates or prongs. In TF experiments, haematite is used preferentially to remove a background non-relaxing cosinusoidal signal which would reduce the sensitivity of the experiment to effects in the sample.

2.5.4 Experimental determination of background terms

Many relaxation functions contain a *background term* of the form A_{bg} or $A_{\mathrm{bg}}\mathrm{e}^{-\lambda_{\mathrm{bg}}t}$ to account for a static or nearly-static offset common to all spectra. This often arises from muons stopping in the silver sample holder or cryostat tails because a sample either does not cover the full area of the muon beam, or is too thin to stop every incident muon. This underlying background must be identified by evaluating the constant α (in Eq. (2.8)) to find the *full asymmetry*, and then subtracting the *relaxing asymmetry* arising from the sample, leaving the background. It is possible to extract α by measuring a spectrum in transverse field mode when the sample is in a benign phase, i.e. paramagnetic, non-superconducting, *etc.*, and then adjusting α until the spectrum is symmetric about the x-axis.

In addition to this, however, the background can also be affected by applied or stray magnetic fields (which alter the paths of both incident muons and decay positrons), detector efficiency, and so on. In practice, this means that backgrounds can vary slightly during the course of an experiment. However, it is often unnecessary to precisely constrain the background term where the quantity of interest is an oscillation frequency or a relatively fast relaxation. Consequently, unless a detailed analysis of slow relaxations or relative amplitudes is to be performed, it is often sufficient to use a phenomenological background term $A_{\mathrm{bg}}\mathrm{e}^{-\lambda_{\mathrm{bg}}t}$ which is allowed to vary slightly between experimental runs. Its magnitude is roughly constant, and any relaxation associated with it is typically found to be $\sim 0.01\,\mathrm{MHz}$; significant deviation from these conditions means it is probably incorrect to have identified this term as entirely background. If well-behaved, however, the significance of the background term is limited, and its behaviour is largely ignored in this thesis. For example, in Ba_2NaOsO_6 (see Sec. 4.3.1), the background relaxation contributes around a third of the total signal in all runs, with a relaxation rate $\lambda_{\mathrm{bg}} \approx 0.03\,\mathrm{MHz}$, which is typical and thus disregarded.

Chapter 3

Dipole-field simulation

The criticism most often levelled at μ^+SR is that the experimenter usually does not know the muon site precisely. The electrostatic potential inside crystals is difficult to evaluate and, even if it were known, the muon inevitably alters this charge distribution wherever it comes to rest, making the problem harder still. One possible solution in ordered magnetic materials is to reverse-engineer the problem by working out the magnetic fields inside the crystal, and looking to see where these match those observed experimentally. The parameters extracted empirically are the muon precession frequencies, which are directly proportional to the local field at the muon sites. If this local field is calculated at all sites in the crystal, the places where the values are close to those actually observed give the locations where muons might stop.

In this chapter, dipole field simulation is taken beyond this traditional application of the technique. The observed frequency is not the only known parameter in this problem: reasonable assumptions can be made about the kinds of sites where a muon might stop, the sizes of the magnetic moments, or reasonable magnetic structures. Given bounds on a subset of these, the limits on the others can be extracted using Bayes' theorem.

First, dipole fields for single dipoles and then arrays are explored in Sec. 3.1; we will then examine Ewald summation as a method for rapidly calculating potentials and fields in infinite crystals in Sec. 3.2.1, followed by the alternative of using a Lorentz sphere of dipoles in Sec. 3.2.2; then, non-dipolar contributions to the field at the muon site are examined in Sec. 3.3. These tools can then be used to perform dipole-field simulations, which are explained in their traditional form in Sec. 3.4, and with our novel Bayesian approach in Sec. 3.5. A brief overview of MµCalc, my software for evaluating dipole fields, is given in Sec. 3.6, followed finally by suggestions for future work in Sec. 3.7. Supplementary to this chapter, details of the mathematics behind Ewald summation are given in Appendix A, and the magnetic propagation vector formalism is introduced in Appendix B, providing a very general way to describe periodic magnetic structures.

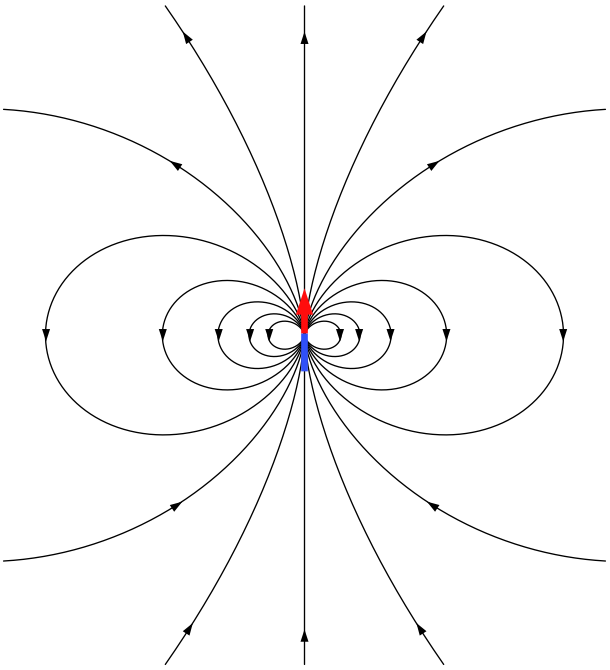

Figure 3.1: The field of a single ideal dipole. Field lines run from north (the upper, red pole) to south (the lower, blue one).

3.1 Dipole fields

3.1.1 The field from a single dipole

Gauss's law famously states that it is not possible for single magnetic monopoles to exist independently:

$$\nabla \cdot \boldsymbol{B} = 0. \tag{3.1}$$

Though there are no free magnetic charges, magnetic dipoles proliferate throughout nature. They can be envisaged as tiny loops of current or as pairs of magnetic charges with infinitesimal separation. The field around a magnetic dipole runs from its north pole to its south, in a configuration similar to the familiar pattern observed when iron filings are sprinkled in the vicinity of a bar magnet. The field of an ideal dipole is shown in Fig. 3.1.

The dipole field can be expressed in vector notation,

$$\boldsymbol{B}(\boldsymbol{r}) = \frac{\mu_0}{4\pi r^3}\left[3(\boldsymbol{\mu}\cdot\hat{\boldsymbol{r}})\hat{\boldsymbol{r}} - \boldsymbol{\mu}\right], \tag{3.2}$$

where μ_0 is the permeability of free space; $\boldsymbol{r}$ is the position at which we wish to evaluate the dipole field, with respect to a magnetic moment, a vector $\boldsymbol{\mu}$, at the origin; and $\hat{\boldsymbol{r}}$ is the unit vector along the direction of $\boldsymbol{r}$. Alternatively, the field can be written in terms of the *dipolar tensor*,

$$\begin{aligned} B^\alpha(\boldsymbol{r}) &= D^{\alpha\beta}\mu^\beta \\ &= \frac{\mu_0}{4\pi r^3}\left(\frac{3r^\alpha r^\beta}{r^2} - \delta^{\alpha\beta}\right)\mu^\beta \end{aligned} \tag{3.3}$$

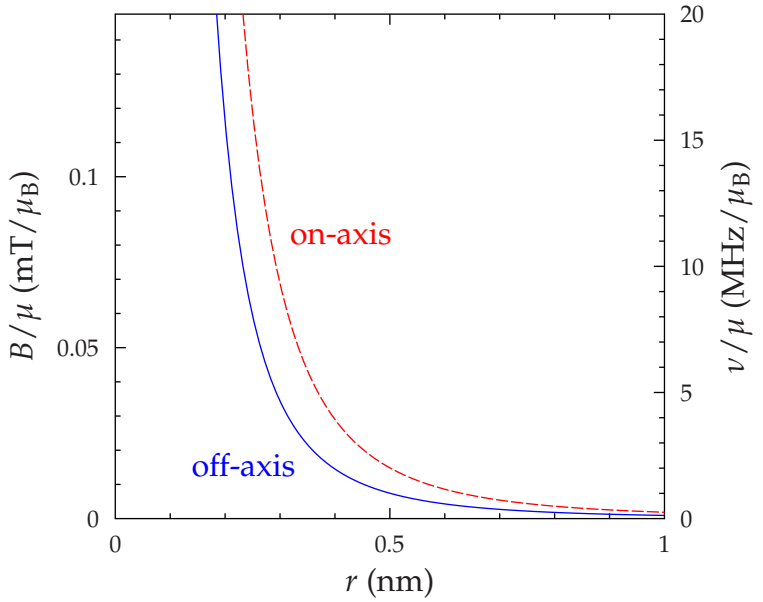

Figure 3.2: The field from a point dipole of unit moment as a function of distance. The blue, solid line represents the field perpendicular to the dipole axis, whilst the red, dashed line shows the field along the axis, which is larger by a factor of two. The graph is in units which are approximately appropriate for μ^+SR, where a muon will embed itself a few nanometres from magnetic moments of order a few Bohr magnetons. The left-hand y-axis is thus the field expected per Bohr magneton, μ_B. The right-hand y-axis shows the precession frequency which would be observed in a muon spin-rotation experiment, obtained by multiplying the field by the muon gyromagnetic ratio, $\gamma_\mu/2\pi = 135.5\,\mathrm{MHz\,T^{-1}}$.

where $\delta^{\alpha\beta}$ is the Kronecker delta, and the Einstein summation convention is applied.

The field strength falls off rapidly with distance, with Coulomb's familiar inverse square law being replaced by an inverse cube relationship. The field is also twice as strong along the axis of the dipole as it is perpendicular to that axis. The strength of the dipole field B is thus a function of the dipole moment μ, distance from it r, and the angle made with its axis, θ:

$$B(\mu, r, \theta) = \frac{\mu_0}{4\pi}\frac{\mu}{r^3}\sqrt{1+3\cos^2\theta}\,. \tag{3.4}$$

A graph of this strength as a function of distance in units appropriate for μ^+SR is shown in Fig. 3.2.

3.1.2 The field from arrays of dipoles

The dipolar field experienced by a muon embedded in a crystal, $\boldsymbol{B}_{\mathrm{dipole}}$, is a function of the muon site $\boldsymbol{r}_\mu$ and comprises the vector sum of fields from all dipoles inside the crystal. Thus, we perform the sum

$$\boldsymbol{B}_{\mathrm{dipole}}(\boldsymbol{r}_\mu) = \sum_i \frac{\mu_0}{4\pi r^3}\left[3(\boldsymbol{\mu}_i\cdot\hat{\boldsymbol{r}})\hat{\boldsymbol{r}} - \boldsymbol{\mu}_i\right], \tag{3.5}$$

where μ_0 is the permeability of free space, and $\boldsymbol{r} = \boldsymbol{r}_i - \boldsymbol{r}_\mu$ is the relative position of the muon and the i^{th} ion with magnetic moment $\boldsymbol{\mu}_i$. Two examples of dipole fields summed over a number of dipoles in two dimensions are shown in Fig. 3.3.

The field distributions resulting from arrays of dipoles show two general features. Firstly, when near to any given dipole, its field tends to dominate; in Fig. 3.3, the field arrows are almost identical near any given spin in the grids of (b) or (c) as they are close to the isolated spin in (a). Secondly, there are usually points of cancellation at positions of high symmetry, where the total field from the dipoles sums to zero. The impact on a muon is thus contingent on its site with respect to the magnetic ions in a crystal: a muon sufficiently close to an ion will be largely indifferent to the surrounding magnetic structure. However, since magnetic ions are often positively charged and thus repel muons, the interaction of many dipoles is usually relevant in dipole-field calculations for μ^+SR.

Strictly, dipole sums should be evaluated over all magnetic moments in the crystal, but the intractability of this sum for $\sim 10^{23}$ moments inside an entire crystal necessitates truncating it somehow. Two possible methods to make this sum tractable are Ewald summation, explained in the next section, and use of Lorentz spheres (see Sec. 3.2.2). Truncating the sum also gives rise to additional fields due to finite-size effects (see Sec. 3.3.1).

In general, distributed spin-density requires treating this sum as an integral over the space inside the crystal [31]. However, in many cases it should be acceptable to approximate the moments as point dipoles attached to a given atomic site. This approximation inevitably holds for the dipoles further from the muon, and remains plausible for nearby dipoles in magnetic insulators where the magnetic ions are small. A further assumption usually made is that the crystal is in a magnetic ground state, and the moments are fully, statically ordered throughout the crystalline bulk. In order to compare the fields extracted from these simulations, it is therefore necessary to extrapolate from experimental data the muon precession frequency at zero temperature.

3.2 Dipole sums

3.2.1 Ewald summation

Ewald summation [32] is a method of rapidly evaluating potentials, fields, *etc*. within an infinite lattice. It offers significant reductions in the computing time required to perform such calculations by deftly dividing labour between a sum in real space, with charges or dipoles artificially screened to overcome long-range interactions, and a sum in reciprocal space which accounts for those long-range interactions neglected in the real-space sum. In the case of calculating the electrostatic potential in crystals, Ewald summation allows evaluation of a sum which, in real space, is potentially infinite in length. The reduced range of dipole-field interactions ($\sim 1/r^3$ as opposed to $\sim 1/r$) necessarily makes gains more modest. An overview of the mathematics of Ewald summation is given in Appendix A. Ewald summation has been previously used in dipole-field simulations for μ^+SR, in e.g. Ref. 31.

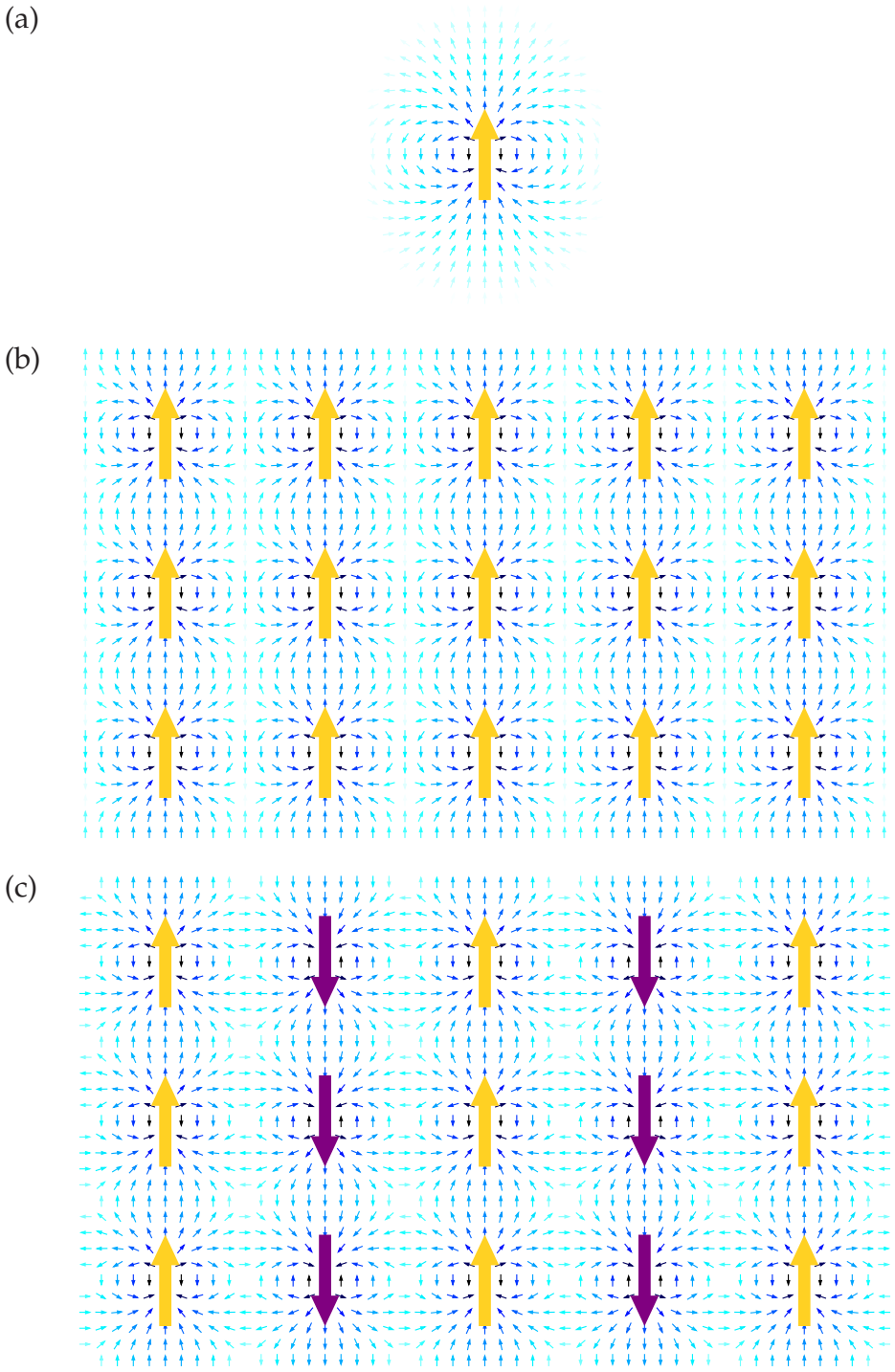

Figure 3.3: Dipole fields emanating from a grid of magnetic dipoles in the plane of the page. The large arrows are dipole moments. Small arrows show the dipole field, pointing along its direction and coloured on a logarithmic scale according to its magnitude; lighter colour indicates weaker field. Fields are shown from (a) a single dipole; (b) a square grid of dipoles aligned ferromagnetically; (c) a square grid of dipoles aligned antiferromagnetically. In both of the latter cases, points of cancellation are evident.

3.2.2 Lorentz spheres

An alternative method of summing dipolar fields [33] is to discard those moments outside a relatively small Lorentz sphere centred at $\boldsymbol{r}_\mu$, and subsequently apply an appropriate correction, the Lorentz field $\boldsymbol{B}_L$, to account for fields from the disregarded dipoles (see Sec. 3.3.1). The approximation is valid for dipole fields in contrast to electrostatic potentials due to their more rapid attenuation with distance.

The size of sphere required to obtain an accurate answer can be obtained by performing trial calculations at various cut-off radii until the value converges; such a convergence test is illustrated in Fig. 3.4. This typically requires $\lesssim 10,000$ moments to converge to within less than $< 1\%$ of the true value (significantly higher precision than that to which frequencies are commonly determined in μ^+SR). This kind of calculation can be completed in minutes or hours if evaluating fields at even a few million points.

3.2.3 Ewald or Lorentz?

Calculating dipole fields using Ewald's method is significantly more mathematically complex than using Lorentz spheres, and ultimately it was the latter, simpler method which was implemented in the software developed for this thesis. Though using Lorentz spheres is in theory more computationally expensive, the speed penalty paid for this choice is relatively insignificant in traditional dipole-field analyses, as opposed to the Bayesian dipole-field analysis techniques described in Sec. 3.5. In a typical conventional dipole calculation, fields might be evaluated at positions on a grid comprising a few thousand points which is then examined by eye for suitable field values. Calculating such a grid typically only takes a matter of minutes, and thus is not a rate-limiting step in a μ^+SR data analysis workflow. The Bayesian technique, by contrast, usually entails calculating fields at tens of millions of randomly-generated points in order to obtain a smooth curve, then repeating this for a variety of different magnetic structures. This can take days on contemporary desktop computers, and it would certainly be worth revisiting Ewald summation in an attempt to optimise these calculations.

Future work examining how to constrain muon positions in Bayesian dipole-field simulations should certainly attempt to do so using electrostatic potentials since they would be expected to provide an estimate of minimum-energy positions for muons to come to rest. As is shown in Appendix A, Ewald summation is almost essential to achieving reliable convergence of electrostatic potential calculations within crystal lattices, and could well therefore have a rôle in muon site determination.

3.3 Other magnetic fields at the muon site

A muon passively precessing in its local environment experiences a total magnetic field comprising the vector sum of several different components [7]:

$$\boldsymbol{B} = \boldsymbol{B}_0 + \boldsymbol{B}_{\text{dipole}} + \boldsymbol{B}_L + \boldsymbol{B}_{\text{demag}} + \boldsymbol{B}_{\text{hyperfine}} + \boldsymbol{B}_{\text{trans}} + \boldsymbol{B}_{\text{diamag}}. \tag{3.6}$$

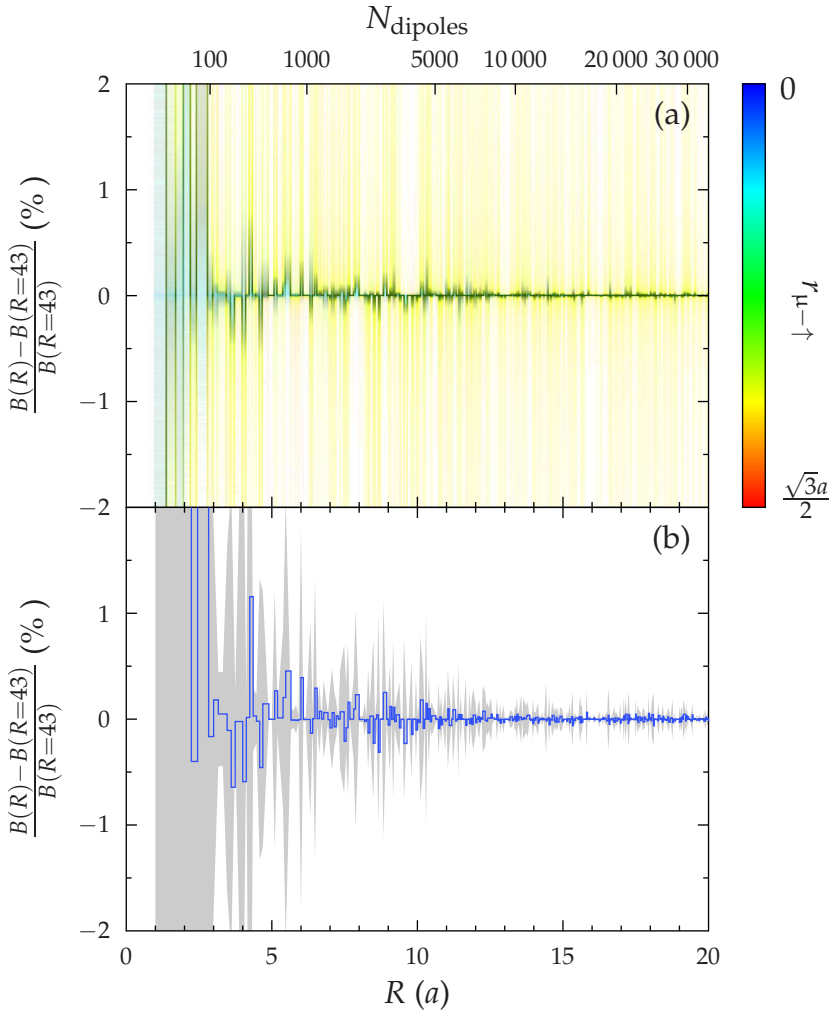

Figure 3.4: The convergence of values of magnetic field towards the true value in a hypothetical primitive cubic antiferromagnet with increasing Lorentz sphere radius R, in terms of the cubic lattice parameter a (the upper x-axis shows the number of dipoles N_{dipoles} contained in a sphere of radius R). The 'correct' value of the magnetic field is ascertained by performing a dipole-field calculation with a very large Lorentz sphere with a radius $R = 43a$, and convergence towards that value has been evaluated at 100 000 randomly-chosen points within the unit cell. A colour map in (a) shows how rate of convergence varies with proximity to a spin, $r_{\mu-\uparrow}$. Blue points are closest to spins, with green intermediate and red farthest. Colour density indicates the number of points, but the scale is non-linear to enhance visibility of the regions of slow convergence. (b) Aggregate values: the central blue line indicates the average error on the evaluated field values, whilst the grey shaded region indicates plus or minus the root mean square error. Note that the y-axis scale only extends to $\pm 2\%$: field values rapidly converge to an error of $< 1\,\%$ for spheres with radii $R \gtrsim 5a$.

- $\boldsymbol{B}_0$ is any external field applied during the experiment.
- $\boldsymbol{B}_{\text{dipole}}$ is the dipole field resulting from a summation of all dipolar fields inside the crystal, as described previously.
- $\boldsymbol{B}_{\text{L}}$ is the *Lorentz field*, and arises from those dipoles outside the Lorentz sphere.
- $\boldsymbol{B}_{\text{demag}}$ is the *demagnetising field* resulting from the finite size of the sample. It is a contribution from those dipoles at the sample surface, and consequently depends on sample shape.
- $\boldsymbol{B}_{\text{hyperfine}}$ is the *contact hyperfine field* arising from any spin density overlapping with the muon site.
- $\boldsymbol{B}_{\text{trans}}$ is the *transferred hyperfine field*, due in metals to the Ruderman–Kittel–Kasuya–Yosida (RKKY) interaction [34].
- $\boldsymbol{B}_{\text{diamag}}$ is the *diamagnetic field*, and results from supercurrents screening applied magnetic field. It is thus specific to superconductors, and will not be explored here.

3.3.1 Lorentz and demagnetising fields

In crystals without a net magnetisation, dipole-field simulations are significantly simplified because parts of the crystal far from the muon do not exert a net field on the muon site. The Lorentz and demagnetising fields are zero in such systems. However, in many ferro-, ferri- or canted antiferromagnetic systems, magnetisation $\boldsymbol{M} \neq \boldsymbol{0}$ and it is necessary to include these corrections in order to obtain a correct estimate of the field at the muon site.

The Lorentz sphere, Lorentz field and demagnetising field are shown in the schematic diagrams in Fig. 3.5. First, in Fig. 3.5 (a), a Lorentz sphere of dipoles is shown, representing the initial dipole sum as described in Sec. 3.2.2. The moments outside a spherical void in an infinite crystal will result in an additional Lorentz field $\boldsymbol{B}_{\text{L}}$ proportional to and parallel with the net magnetisation $\boldsymbol{M}$,

$$\boldsymbol{B}_{\text{L}} = \frac{\mu_0 \boldsymbol{M}}{3}, \tag{3.7}$$

where μ_0 is the permeability of free space. This effect is illustrated in Fig. 3.5 (b).

The demagnetising field $\boldsymbol{B}_{\text{demag}}$ is a finite-size effect caused by moments at the sample surface. A magnetic field runs between unpaired magnetic poles at the surfaces, and will usually act to reduce the sample magnetisation; this tendency to oppose the magnetisation gives rise to its name. The demagnetising field in a planar sample is a particularly simple case, and is shown in Fig. 3.5 (c). Here, each face is entirely composed of magnetic poles of the same sign, and field will run from 'plus' to 'minus', creating a field precisely opposite the magnetisation. In general, however, this field varies with sample shape and position inside the sample, and is very difficult to calculate for an arbitrarily-shaped object (see e.g. Ref. 34).

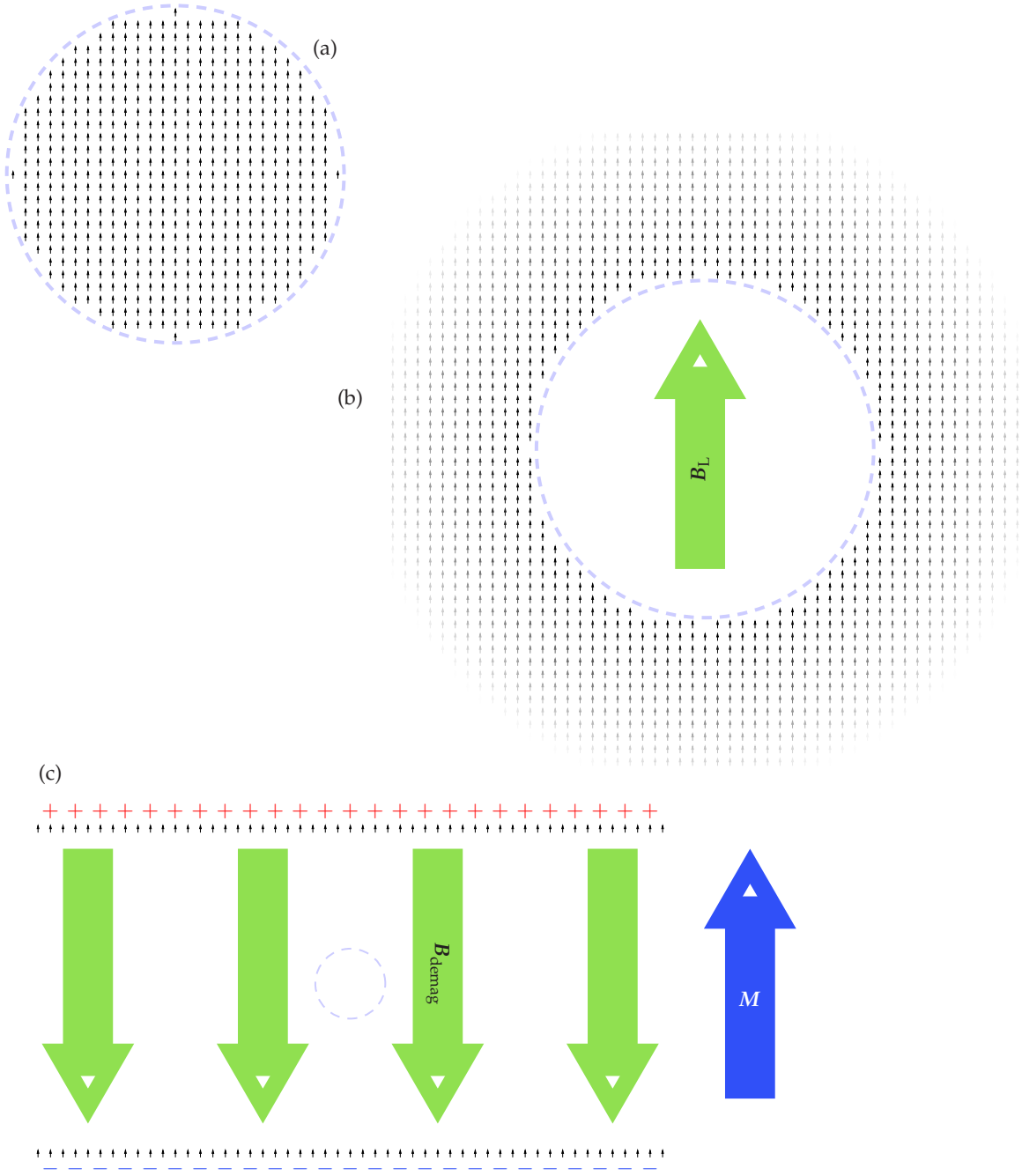

Figure 3.5: Schematic representation of the Lorentz and demagnetising fields. The small black arrows represent individual atomic dipoles. (a) The Lorentz sphere of dipoles used to calculate the approximate dipole field inside a sample. (b) The dipoles outside the Lorentz sphere, extending to infinity, exert a Lorentz field $\boldsymbol{B}_{\mathrm{L}}$ inside that sphere. (c) In real, non-infinite samples, surface effects result in a demagnetising field, $\boldsymbol{B}_{\mathrm{demag}}$, due to the effect of unpaired magnetic poles at the sample surface. Here, in an infinite planar sample, north is represented by + and south by $-$, and the demagnetising field runs from plus to minus, opposite to the sample magnetisation. The + and $-$ signs represent positive and negative divergences of $\boldsymbol{H}$ created by the boundary of the sample magnetisation: since $\nabla \cdot \boldsymbol{B} = 0$, $\nabla \cdot \boldsymbol{H} = -\nabla \cdot \boldsymbol{M}$.

However, it can be explicitly calculated for various special cases. For example, the demagnetising field in ellipsoids is given by

$$\boldsymbol{B}_{\text{demag}} = -\mu_0 \mathsf{N} \boldsymbol{M}\,, \tag{3.8}$$

where N is the demagnetising tensor. If the magnetic field lies along one of the ellipse's principal axes, N can be diagonalised, giving

$$\mathsf{N}_{\text{ellipsoid}} = \begin{pmatrix} N_x & 0 & 0 \\ 0 & N_y & 0 \\ 0 & 0 & N_z \end{pmatrix}. \tag{3.9}$$

In the doubly special case of a sphere, $N_x = N_y = N_z = \frac{1}{3}$, allowing the demagnetising field to be expressed in terms of a scalar demagnetising factor N,

$$\boldsymbol{B}_{\text{demag}} = -\mu_0 N \boldsymbol{M}\,,$$

where $N = \frac{1}{3}$ for uniformly-magnetised spheres. A very long cylindrical rod orientated in the z-direction exhibits $N_x = N_y = \frac{1}{2}$, $N_z = 0$, because if the magnetisation points along the direction of the rod, the monopoles created will be at infinity, and thus exert no influence. Similarly, for an infinite, flat plate perpendicular to z [as shown in Fig. 3.5 (c)], $N_x = N_y = 0$, $N_z = 1$.

As well as systems where $\boldsymbol{M} = \boldsymbol{0}$, the Lorentz and demagnetising fields can be neglected in perfectly spherical samples because the two are equal in magnitude but opposite in sign. In most cases, the two fields will cancel to some extent, and an order of magnitude upper bound can be extracted by computing $\mu_0 \boldsymbol{M}$.

3.3.2 Hyperfine fields

Hyperfine fields result from the overlap between a muon wavefunction and any spin-density at the muon site. The hyperfine field at the muon position $B_{\text{hyperfine}}(\boldsymbol{r}_\mu)$ is given by [8, 35]

$$B_{\text{hyperfine}}(\boldsymbol{r}_\mu) = \frac{2\mu_0}{3\mu_B}\left[n^{\uparrow}(\boldsymbol{r}_\mu) - n^{\downarrow}(\boldsymbol{r}_\mu)\right], \tag{3.10}$$

where μ_0 is the permeability of free space, μ_B is the Bohr magneton, and $n^{\uparrow,\downarrow}(\boldsymbol{r}_\mu)$ are the densities of spin up and down electrons at the muon site, respectively. Hyperfine fields have the potential to be very large: a muon overlapping with a single, spin-up electron occupying a volume equal to the Bohr radius cubed would experience a hyperfine field

$$B_{\text{hyperfine}} = \frac{2\mu_0}{3\mu_B}\frac{1}{a_0^3} = 52.4\,\text{T}, \tag{3.11}$$

giving rise to a muon precession frequency $\nu = \gamma_\mu B_{\text{hyperfine}} = 7100\,\text{MHz}$! The density of spin-polarised electrons overlapping with a muon will usually be somewhat lower than this.

In spite of this relatively simple definition, the hyperfine field is difficult to ascertain. Knowledge of the local spin-density at the muon site firstly presupposes knowledge of the muon site, which is itself usually unknown. Even then, conventional calculations or experiment will usually ignore the perturbation from the muon in the system; for example, measuring the spin-density throughout the unit cell from neutron diffraction only gives information on the system in the absence of a muon.

Some information about the hyperfine field can be gleaned from muon experiments by measuring the *Knight shift* [8], which is the shift in muon precession frequency from that expected in an applied field B_0 in a sample in the paramagnetic state. The magnetisation induced in the sample by the applied field manifests as an imbalance in the density of spin-up and -down electrons at the muon site, resulting in a hyperfine field which modifies the applied field. However, translating this into the hyperfine field experienced in the ordered state is non-trivial. Firstly, the Knight shift is affected by other components of the local field, such as the field from the atomic dipoles associated with the degree of magnetisation induced. Secondly, the ordering of the spins induced by applied field may differ in configuration or direction from that in a state of spontaneous magnetic order. For example, the magnetisation in spontaneous order will be along the material's easy axis, whereas the magnetisation in field will be parallel to that field. Further, in materials which experience order other than ferromagnetic, the spins will not all align coparallel with one-another as they do in field in the paramagnetic state, adding further complexity to evaluating the likely spin-density at the muon site.

Hyperfine fields present the largest potential pitfall in analysis of local fields at muon sites, because of this difficulty in evaluation and their potential to be large. However, in magnetic insulators, and especially those where the magnetic species are small in spatial extent, positively-charged and thus repulsive to muons, and have a small and/or reduced magnetic moment, the quantity of spin-density expected at the muon site would be small.

3.4 Dipole-field analysis

Dipole-field analysis has traditionally been used to isolate possible muon sites by stipulating that the muon must stop at a position with a dipole field compatible with the precession frequencies observed in experiment. First, dipole fields are calculated at all positions on a grid inside the unit cell. Choosing a grid with a prime number of elements in each direction limits the potential for sampling artefacts. Then, fields which differ by more than some tolerance from those actually observed in the μ^+SR spectra are discarded, and positions are sought where the correct field is observed, and the muon may plausibly stop due, for example, to proximity to some negative ion.

Further information can be inferred by attempting to model the charge distribution inside the unit cell, with sophistication ranging from examination of sites with the correct field for proximity to negative ions [36]; to analogy with similar structures [37]; to phenomenological attempts to map the electric potential inside

the crystal [38, 39]; to attempts to evaluate the electronic structure of the crystal with computational methods such as density functional theory.

The electronic structure of a crystal obeys the symmetry of the lattice and consequently, if a muon stops in a given position, it should stop in all crystallographically-equivalent positions. This provides another opportunity to interrogate dipole-field simulations because many transitions to long-range magnetic order will create a magnetic unit cell larger than the crystallographic one—in the language of Appendix B, they will have a nonzero magnetic propagation vector. Thus, it is possible for crystallographically-equivalent sites to be magnetically-inequivalent and, were muons to stop in such a site, multiple frequencies would be observed. Thus, when performing dipole-field simulations, it is important to check that the proposed muon site does not give rise to any additional frequencies not present in the $A(t)$ spectra [37]; or, conversely, the presence of multiple frequencies in some materials can be explained by this effect [40, 41].

The largest limitation of dipole-field analysis in this form is that, for it to be effective, the magnetic structure of the material must be known. If it is not, the muon position will be wrong, and quantifying the uncertainty is difficult. Because the magnetic structure is assumed, this process for determining the muon site is also circular, and the muon site does not in itself give any information about sample properties. Its use is as a (binary) consistency check: the absence of appropriate fields in plausible sites would be relatively solid evidence that the assumed magnetic structure was in error.

It is, in fact, quite common for the magnetic structure to be unknown. This can either be because the muon results precede studies to determine the magnetic structure (e.g. using neutron scattering), or because such studies would be difficult due to ferromagnetism, small moments, large concentrations of hydrogen *etc*. Changing magnetic structures can often result in a dramatic alteration of muon precession frequency at a given site: in the most extreme case, the muon could sit at a point of cancellation in an alternative structure, having previously occupied a site of nonzero field. On top of this, moment sizes are often not known precisely, and muon precession frequency scales with these. It is to quantify the uncertainty resulting from unknown muon sites and ill-constrained magnetic structures that we approach dipole-field analysis with Bayesian inference.

3.5 Bayesian dipole-field analysis

Bayesian inference is a method which allows calculation of what can be reasonably deduced given what is actually known. This section will explore its application to combining dipole-field simulation with μ^+SR results. First, we examine probability distributions of dipole fields, taking specifically the example of antiferromagnet MnO; then Bayes' theorem is introduced; and finally the two are combined into Bayesian dipole-field analysis.

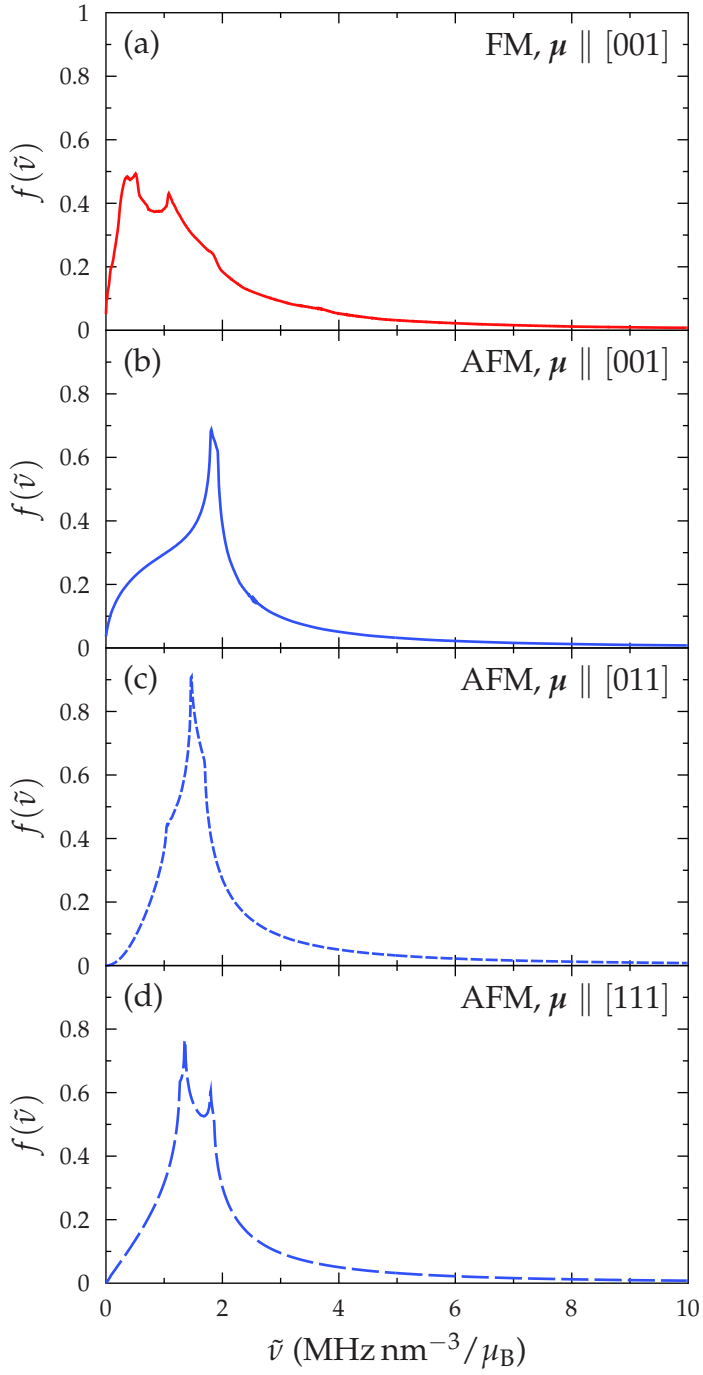

Figure 3.6: Dipole-field distributions inside a number of model systems, after Ref. 42. Moments on a simple cubic lattice are aligned (a) ferromagnetically along the crystal axis [001]; (b) antiferromagnetically with propagation vector $\boldsymbol{k}_0 = (\pi, \pi, \pi)$ with moments pointing along [001]; (c) antiferromagnetically with $\boldsymbol{k}_0$, moments along [011]; and (d) antiferromagnetically with $\boldsymbol{k}_0$, moments along [111].

3.5.1 Dipole-field distributions

Given that the muon site is *a priori* unknown, we might assume that it can stop in one of many possible locations inside a crystal. One possibility is to relax all assumptions about possible muon sites, and to assume that the muon stops everywhere [42]. This might actually be appropriate in some physical systems; for example, in complex single-molecule magnets where there are many hundreds of atoms per unit cell, muons may stop in a large number of magnetically-inequivalent muon sites. Graphs in Fig. 3.6 show the probability density function (pdf) of dipole fields in a variety of different magnetic structures on a simple cubic lattice. The x-axes are in terms of the scaled frequency $\tilde{\nu} = \left(\gamma_\mu a^3/2\pi\mu\right) B$, to facilitate comparison with general experimental data. Common features include the distributions' asymmetry; a $\tilde{\nu}^{-2}$ tail, corresponding to those muons stopping very near to a magnetic ion; and sharp Van Hove singularities [43], with positions corresponding to field values at points of high symmetry. These features are analogous to those in the magnetic field distributions found in the superconducting vortex lattice, described briefly in Sec. 2.4.2.

In materials with a unit cell containing fewer atoms, the assumption of uniform muon distribution is problematic. Instead, muons are likely to stop at a small number of sites of high electron density, and often gravitate towards interstitial positions to minimise their electrostatic energy. It is then rational to evaluate the dipole-field distribution over a constrained set of sites using known or likely muon positions. An obvious constraint is to add a cut-off radius around positive ions within which muons will not stop. The effect of this to first order is often to truncate the $\tilde{\nu}^{-2}$ tail, because many magnetic centres are cationic. As the cut-off is increased in materials containing other positive species, there will be more complex effects on the pdf contingent on the location of other positive ions relative to the dipole-field distribution. It is also sensible to apply a cut-off proximity to negative ions, as there will come a point when electrons cannot successfully screen the muon from the effects of the positive nuclear charge.

A simple constraint in oxides is that muons usually stop around 0.1 nm from an O^{2-} ion [44, 45]. Thus, we might examine sites where $r_{\mu^+\text{–}O} = 0.10(01)$ nm (this approach is used in Ba_2MOsO_6 in Chapter 4). Alternatively, the muon site may be able to be determined directly from data taken above the transition to long-range magnetic order, e.g. by the examination of Fμ dipole–dipole oscillations in muon spectra (an example of this in the $[M(HF_2)(pyz)_2]X$ series of molecular magnets is discussed in Chapter 6). Another possibility is that, in simple structures the muon's position can be assumed to be at mid-points between ions identified by inspection; for example, in materials with the rock salt structure, muons tend to stop at the body-centre of the simple cubic lattice, placing them equidistant between attractive negative and repulsive positive ions [37, 46].

It is important to emphasise that these distributions are not to be identified with a distribution of fields at the muon site. (Dipole-field simulations can be used in conjunction with calculations of likely muon thermal ellipsoids to identify on-site field distributions [38], but this is not investigated here.) The extent of the muon wavefunction is likely to be comparable with that of a proton in a similar material

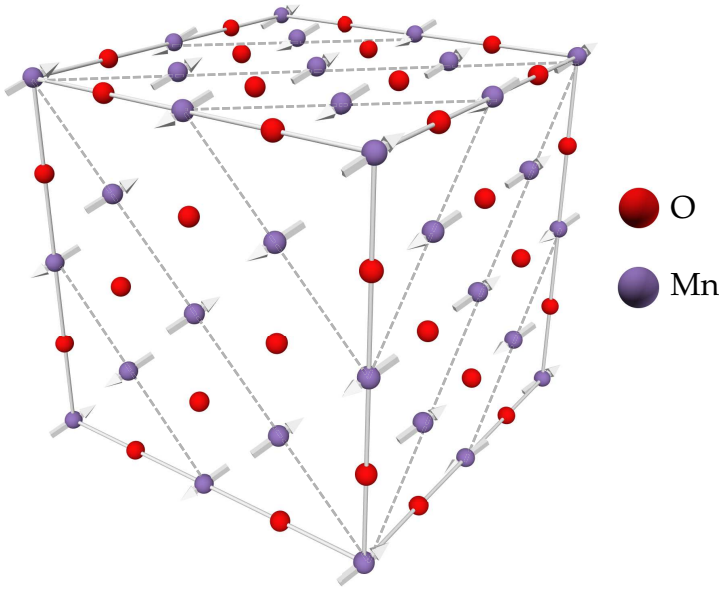

Figure 3.7: Schematic structure of MnO in the magnetically ordered phase. The structure shown is a face-centred cubic simplification of the actual structure (see text). Arrows indicate the direction of the Mn spins (along $[1\,1\,\bar{2}]$ in this crystal system), while dotted lines indicate the $[1\,1\,1]$ planes of ferromagnetism.

MnO
$Fm\bar{3}m$
$a = b = c = 0.4426\,\text{nm}$ [47]
$\alpha = \beta = \gamma = 90°$
Mn^{2+} @ $(0,0,0)$, $\mu = 5.65\mu_B$ [48]
O^{2-} @ $(0.5,0,0)$
$\boldsymbol{m}_1 = \frac{\mu}{\sqrt{6}}(1,1,-2)$, $\boldsymbol{m}_2 = \frac{\mu}{\sqrt{6}}(-1,-1,2)$ [48]
$\boldsymbol{k} = (\pi,\pi,\pi)$

Table 3.1: Manganese(II) oxide structural parameters for a simplified version of the structure based on a face-centred cubic lattice. The basis vector $\boldsymbol{m}_1$ applies to the Mn at $(0,0,0)$, whilst $\boldsymbol{m}_2$ concerns the symmetry-equivalent Mn sites at $(0,0.5,0.5)$, $(0.5,0,0.5)$ and $(0.5,0.5,0)$; the propagation vector $\boldsymbol{k}$ applies to all Mn atoms.

and therefore will tend to be relatively small, especially at low temperatures. It is therefore usually relatively unproblematic to approximate muon sites as definite and point-like: possibly small in comparison to variations in the dipole field; almost certainly small compared to hypothetical 0.02 nm-thick spherical shells around negative ions.

3.5.2 An example: MnO

Manganese(II) oxide is considered an archetypal antiferromagnet. In 1949, neutron scattering from MnO was used to detect the first incontrovertible experimental evidence for antiferromagnetism [47]. It comprises $S = \frac{5}{2}$ Mn^{2+} ions and $S = 0$ O^{2-} ions arranged in a rock salt structure. Below $T_N = 118\,K$, the material enters a state of long-range magnetic order; the size of the unit cell doubles as the Mn moments antialign, with ferromagnetic sheets of Mn along $[1\,1\,1]$ planes. A simplified picture of the MnO magnetic unit cell is shown in Fig. 3.7, and the parameters associated with this approximate structure can be seen in Table 3.1.

With hindsight, MnO is not as perfect an archetype as might be supposed. Rather than being a Heisenberg antiferromagnet on a cubic lattice, the transition to long-range magnetic order is associated with a degree of structural distortion—a stretching along the $[1\,1\,1]$ direction in the original stucture—which reduces the symmetry to rhombohedral [49]. Neutron scattering allows the moment direction to be constrained; the Mn spin vectors lie within the ferromagnetic planes [49]. Modelling recent high-resolution total scattering neutron data with reverse Monte Carlo simulations suggests further small deviations from an idealised structure, reducing the symmetry to monoclinic, and suggesting that the moment direction lies along the $[1\,1\,\bar{2}]$ direction specifically (again referred to the simplified face-centred cubic structure) [48]. Even above the transition, MnO behaves somewhat anomalously; there is good evidence [50] that it exhibits significant spin correlations up to $\sim 4.5T_N$, providing further indications that this is not such a simple system as is often assumed.

However, dipole-field simulations on this material do go some way to providing a self-consistent picture. Zero-field μ^+SR experiments [51] find a single muon precession frequency of $\nu = 154\,MHz$, suggesting $B = 1.14\,T$. From the Knight shift in the paramagnetic phase [52], the hyperfine field is estimated to be $B_{hyperfine} = -0.48\,T$. Since other components of the local field would be expected to be zero, we estimate that the dipole field being sought is $B_{dipole} = 1.62\,T$, equivalent to a muon precession frequency of $\nu = 220\,MHz$.

The first result is that dipole-field distributions are relatively insensitive to the slight changes in the crystal structure. This is illustrated in Fig. 3.8, where the dipole fields arising from the face-centred cubic, simplified structure are compared with the more precise monoclinic structure found in Ref. 48. The reduction in symmetry smooths over some of the Van Hove singularities, and moves others: given their intimate relationship with positions of high symmetry [42], this is perhaps unsurprising. The high-field tail, corresponding to muons which stop near a Mn^{2+} ion, is shared by both. The shaded region on the graph corresponds to $\nu = 220\,MHz$: even without any constraints on muon position, this appears to be close to the most likely frequency to be observed.

The next stage of the analysis is to constrain the muon site to plausible positions. The results of this process are shown in Fig. 3.9. Adding the constraint that the muon should sit $0.09 \leq r_{\mu\text{–}O} \leq 0.11\,nm$ from an oxygen restricts possible positions to around 11 % of the MnO unit cell volume. The main effect of this restriction is to reduce the number of muon sites particularly near to a manganese spin site, which

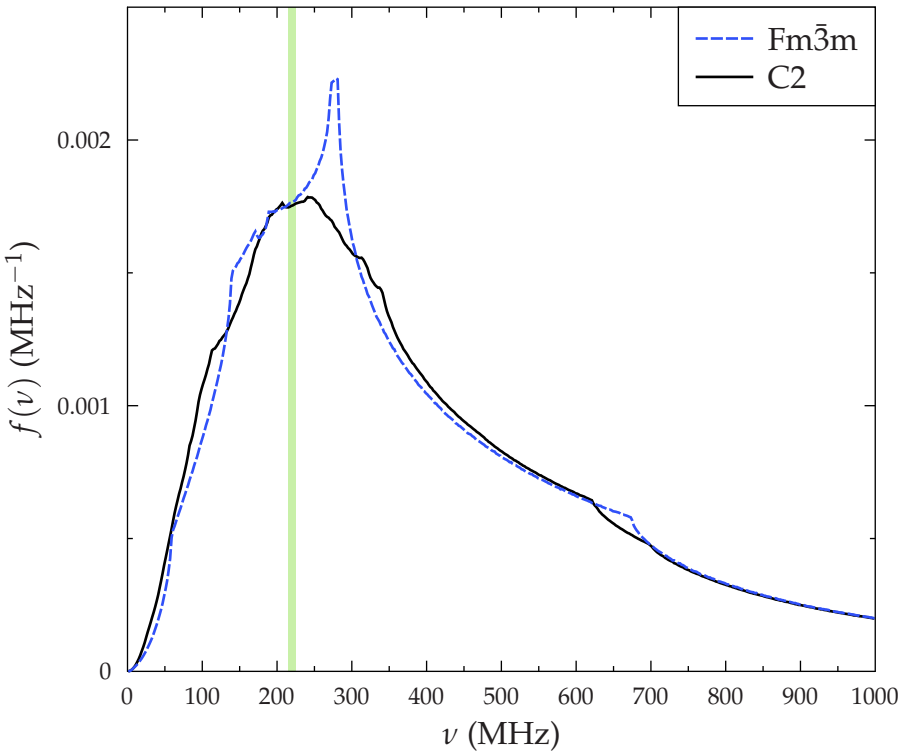

Figure 3.8: The dipole-field distributions inside the unit cell of MnO with two different crystallographic structures. The face-centred cubic structure, space group Fm$\bar{3}$m, is denoted by the dashed blue line, whilst the monoclinic structure, space group C2, is denoted by the solid black line. The green shaded region shows the dipole field actually observed, $\nu = 220\,\text{MHz}$.

significantly squashes the pdf's high-field tail. Adding the constraint that the muon must also sit far from a manganese site ($r_{\mu\text{–Mn}} > 0.17\,\text{nm}$) restricts it to 2.5 % of the unit cell. This eradicates the high-field tail entirely, and rather radically changes the shape of the distribution. Indeed, the most likely muon precession frequencies from this set of constraints lie in two peaks either side of that actually observed! A final simple method of identifying likely muon sites is to look for interstitial sites by constraining the muon to lie far from *all* atoms in the structure: setting $r_{\mu\text{–any}} > 0.17\,\text{nm}$ leaves 5 % of the structure available for occupation by muons, and creates a slightly different distribution, again peaked around the observed precession frequency.

Though this picture of the MnO magnetic and crystal structure therefore forms a consistent narrative when coupled with the muon measurements of total local field and hyperfine field, this story is not tightly constrained. The distribution of precession frequencies stretches from 50 to 350 MHz even when the possible muon positions are restricted to the interstitial 5 % of the unit cell. This means it is possible to neglect the hyperfine contribution entirely and still conclude that the muon stops at this plausible interstitial site, as appears to have been erroneously performed in Ref. 53. The large distribution of fields at the likely sites will almost

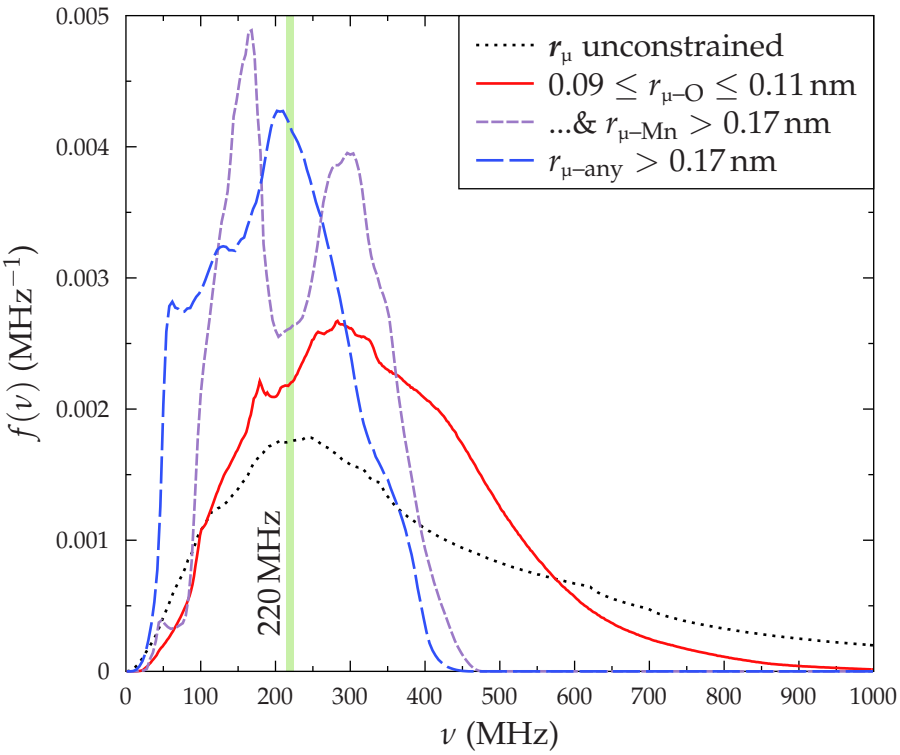

Figure 3.9: Dipole-field distributions in the unit cell of the full, low-symmetry crystal structure of MnO with a variety of different restrictions on muon position. The dotted black line, $\boldsymbol{r}_\mu$ unconstrained, assumes that the muon can stop anywhere, and is identical to the appropriate line in Fig. 3.8. The solid red line, $0.09 \leq r_{\mu\text{–O}} \leq 0.11$ nm, represents those points where the muon is approximately 0.1 nm from an oxygen ion. Adding the further constraint that the muon must stop far from a manganese, $r_{\mu\text{–Mn}} > 0.17$ nm, gives rise to the third, purple dashed line. Finally, interstitial sites are identified by choosing those positions where the muon is far from all atoms, $r_{\mu\text{–any}} > 0.17$ nm, giving the dashed blue line.

certainly persist for other potential moment orientations, which makes this a poor constraint on magnetic structure too. The consistency of the dipole-field simulation with neutron scattering data thus provides some corroboration for both, but this analysis also indicates some of the potential shortcomings of the technique: the large possible effect of hyperfine fields, and the potential for dipole fields to provide only a weak constraint on the system under study.

3.5.3 Bayes' theorem

Bayes' theorem [54, 55] is a mathematical relationship allowing inversion of conditional probabilities. A *conditional probability* is one such as $P(\mathsf{A}|\mathsf{B})$, the probability of an event A occurring given that event B has occurred. The *joint probability* $P(\mathsf{A} \cap \mathsf{B})$ is the probability of A and B both happening, and is given by the probability of B

occuring, multiplied by the probability of A occurring given that B did,

$$P(\mathsf{A} \cap \mathsf{B}) = P(\mathsf{B})P(\mathsf{A}|\mathsf{B}). \tag{3.12}$$

The reverse,

$$P(\mathsf{A} \cap \mathsf{B}) = P(\mathsf{A})P(\mathsf{B}|\mathsf{A}), \tag{3.13}$$

also holds. Now, in the case of some set of mutually-exclusive events $\{\mathsf{A}_i\}$ such that

$$\sum_i P(\mathsf{A}_i) = 1, \tag{3.14}$$

we can write the probability of some other event B as

$$P(\mathsf{B}) = \sum_i P(\mathsf{B}|\mathsf{A}_i)P(\mathsf{A}_i). \tag{3.15}$$

Thus, given a hypothesis H, it is usually possible to compute the likelihood of a given experimental observation O given the truth of that hypothesis, i.e. $P(\mathsf{O}|\mathsf{H})$. However, given that in science our hypotheses must bend to reality rather than the other way around, we actually wish to evaluate the probability of a hypothesis being true *given* the known empirical evidence, i.e. $P(\mathsf{H}|\mathsf{O})$. It is in this context that we wish to reverse conditional probabilities, and thus we turn to Bayes' theorem.

Bayes' theorem expresses the probability of an event A given the occurence of an event B as

$$P(\mathsf{A}|\mathsf{B}) = \frac{P(\mathsf{B}|\mathsf{A})P(\mathsf{A})}{P(\mathsf{B})}. \tag{3.16}$$

It is obtained simply by setting Eq. (3.12) equal to Eq. (3.13). Here, $P(\mathsf{A})$ is the *prior probability* or the *prior*, and represents the probability of A occurring without knowledge of the occurrence or otherwise of B. The derived quantity $P(\mathsf{A}|\mathsf{B})$ is then the *posterior probability*. $P(\mathsf{B})$ can be considered a normalising constant, taking into account the likelihood of B occurring at all.

The theorem's applications are diverse and its results often counter-intuitive: it has been turned to assessing the usefulness of medical screening; to provide a rigorous method of combining evidence in criminal trials [56]; as an alternative to potentially misleading significance tests [57]; and may even provide a quantitative formulation of the scientific method itself.

To take the example of medical screening, imagine we have a test for a medical condition with false positive and false negative rates which are both 1 %. The probability that is sought is then of A (having the disease) given B (a positive result on the test). Let us consider two scenarios: a common disease suffered by $P(\mathsf{A}) = 5\,\%$ of the population, and a rare condition afflicting only $P(\mathsf{A}) = 0.1\,\%$. The probability of receiving a positive result on the test is then the probability of being correctly identified as having the condition, or incorrectly identified as not having it,

$$P(\mathsf{B}) = P(\mathsf{B}|\mathsf{A})P(\mathsf{A}) + P(\mathsf{B}|\text{not A})P(\text{not A}). \tag{3.17}$$

Thus, for the common disease $P(\mathsf{B}) = 0.99 \times 0.05 + 0.01 \times 0.95 = 0.059$, whilst for the rare disease $P(\mathsf{B}) = 0.99 \times 0.001 + 0.01 \times 0.999 = 0.01098$. Finally, Bayes'

theorem gives $P(\mathrm{A}|\mathrm{B}) = 84\,\%$ for the common disease, but only $P(\mathrm{A}|\mathrm{B}) = 9\,\%$ for the rare one: given a positive test result for a given condition, a patient is significantly more likely to have a common condition than a rare one. This might seem counter-intuitive because in both cases the test is extremely and equally accurate. However, when the error rate becomes comparable with the prevalence of what is being tested for, probability dictates that mistaken test results will begin to outnumber actual sufferers. This does not totally invalidate medical testing for uncommon diseases, however, as a 9 % likelihood of actually having the disease is a significant increase in certainty over that possessed before the test was carried out.

When Bayes' theorem is employed in the task of testing scientific hypotheses, it implies that extraordinary claims require extraordinary evidence. The less likely your hypothesis is *a priori*, the stronger the corroboration required to prove it to a given level of certainty. The challenge is to provide a reasonable estimate of these *a priori* probabilities (i.e. the priors) in this case. For a sufficiently fundamental hypothesis, this could entail a complex metaphysical problem.

It is also possible to reformulate Bayes' theorem for continuous probability distributions. Suppose we wish to extract the probability density function f_X of a random variable X given an observed value of an experimental parameter Y, itself a continuous random variable with pdf f_Y,

$$f_X(x \mid Y = y) = \frac{f_X(x) \cdot f_Y(y \mid X = x)}{f_Y(y)}, \tag{3.18}$$

where dividing by $f_Y(y)$ ensures that the resulting pdf integrates to unity.

3.5.4 Application to dipole-field simulation

In a sample under study with μ^+SR, we can combine those facts already known about the system with the μ^+SR results using Bayes' theorem to infer further information. The crucial element in this kind of analysis is to be rigorous in assuming prior probabilities.

The most unambiguous information extracted by a muon experiment is the set of one or more precession frequencies extrapolated to zero temperature, $\{\nu_i(T = 0)\}$, which correspond to magnetic fields which are present at some position inside the sample. Positions are generated at random inside the unit cell to minimise any sampling artefacts, and those which do not satisfy muon site constraints are discarded. Dipole fields at these positions are evaluated and stored, and finally gathered into a histogram, representing a pdf of potential frequencies. If the magnetic structure is already known, this acts as a consistency check. However, if aspects of the magnetic structure are unknown, Bayes' theorem can be employed to narrow the possibilities. The pdf can be recalculated for variant structures and the likelihood of obtaining the observed frequencies can be calculated. The structure in which it is most likely that the observed frequencies be seen is then the most likely structure. The prior probabilities chosen should reflect bounds on quantities known from other experimental techniques, or the wider body of scientific knowledge. For example, the magnetisation direction may be known from other measurements, and

so only moments orientated along this axis need be investigated; or if measuring moment size in an $S = \frac{1}{2}$ system, it would be extremely surprising to find $\mu = 10\mu_B$, and a prior pdf $f(\mu)$ should reflect this.

Obtaining bounds on quantities of interest, or extracting an approximate shape of a pdf, may only require dipole fields to be evaluated at a few thousand points in the unit cell. Evaluating a smooth, well-resolved pdf complete with Van Hove singularities and so forth can require tens or hundreds of millions of points to be evaluated (and, given the inherent unknowns in the problem, such calculations may well be spuriously precise). Though this method has been adopted in this thesis, it is possible that smoothing lower-resolution pdfs, perhaps by convolution with a function representing other unknowns, would provide a truer representation of the uncertainties in these problems.

The technique is most easily illustrated with examples, and as such a sample Bayesian calculation of the known magnetic moment in manganese oxide follows. Other examples include moment size and orientation in Ba_2MOsO_6, which are estimated using this technique in Chapter 4, and moment size in the $[M(HF_2)(pyz)_2]X$ series of molecular magnets, which is derived in Chapter 6.

3.5.5 Bayesian analysis of MnO

We can apply the Bayesian dipole-field analysis technique to estimate the moment size in manganese oxide. The experimentally-observed quantity is the muon precession frequency $\nu = 220\,\text{MHz}$. We then make the plausible assumption that the muon is likely to stop in an interstitial position, as defined by $r_{\mu\text{–any}} > 0.17\,\text{nm}$. Given that we are now taking the moment size as unknown, the pdf of dipole fields is re-evaluated in units of MHz/μ_B, giving rise to a new pdf $f(\nu/\mu)$. (Since dipole fields scale with the size of the moment, this is simply the pdf of dipole fields shown in Fig. 3.9 appropriately scaled.)

Since ν is obtained from experiment, what we would like to know is $g(\mu|\nu)$, the pdf of manganese moment μ *given* the observed ν. This can be obtained from our calculated $f(\nu/\mu)$ using Bayes' theorem [55], which yields

$$g(\mu|\nu) = \frac{\frac{1}{\mu} f(\nu/\mu)}{\int_0^{\mu_{\max}} \frac{1}{\mu'} f(\nu/\mu')\,\mathrm{d}\mu'}\,, \tag{3.19}$$

where we have assumed a prior probability for the manganese moment that is uniform between zero and $\mu_{\max}$. We take $\mu_{\max} = 10\mu_B$, although the results are insensitive to the precise value of $\mu_{\max}$ as long as it is reasonably large. In fact, we evaluate

$$g(\mu|\nu) \propto \int_{\nu-\Delta\nu}^{\nu+\Delta\nu} f(\nu/\mu)\,\mathrm{d}\nu\,, \tag{3.20}$$

where, in the absence of any quantitative uncertainty estimation in Ref. 51, $\Delta\nu$ is a 5 % error on the extracted frequency. The relevant pdfs are shown in Fig. 3.10; first, the muon precession frequency per unit magnetic moment, and secondly

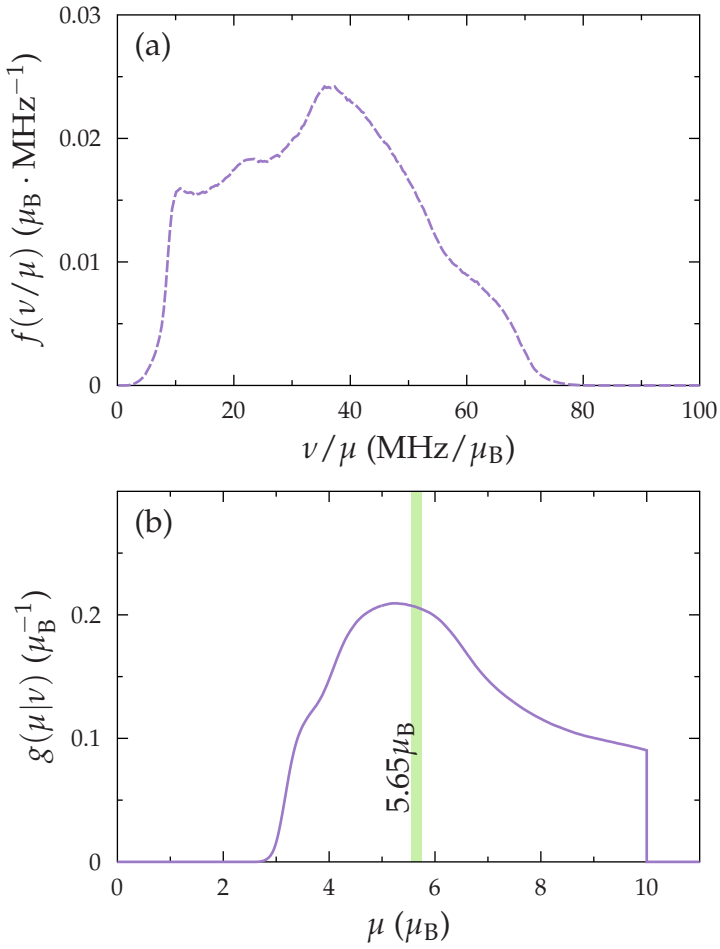

Figure 3.10: A Bayesian derivation of the magnetic moment μ on the manganese ions in MnO. (a) The pdf of observed muon precession frequency ν per unit moment μ. (b) The resulting probability distribution of μ, with the value of $\mu = 5.65\mu_B$ marked.

the magnetic moment calculated given the experimentally-derived frequency $\nu = 220$ MHz. The peak of this probability distribution clearly lies near the $\mu = 5.65\mu_B$ marked: given that the pdf of muon precession frequency shown in Fig. 3.9 peaks at the experimentally-derived frequency given an assumed $\mu = 5.65\mu_B$, this result is unsurprising.

3.6 MµCalc

I have developed MµCalc, a piece of software for dipole-field analysis. It is written using Python [58], a high-level, cross-platform scripting language, which allows it to be run without compilation on Linux/Unix, Windows and Mac systems. MµCalc combines a text-based user interface with a 3D display window, making visual verification of crystal and magnetic structures, as well as generated dipole

fields, simple for users. The program supports all space groups on the Bilbao crystallographic server [59], and can import crystal structures in the widely-used CIF (Crystallographic Information File) format [60]. Magnetic structures are input using the powerful magnetic propagation vector formalism described in Appendix B which allows any periodic magnetic structure, from a simple antiferromagnet to a complex, incommensurate spin-density wave, to be described compactly. MμCalc can then be used to perform convergence testing, as outlined in Sec. 3.2.2, before calculating dipole fields using the Lorentz spheres of dipoles at specified points, on a grid, or at randomly-generated points, with the ability to filter by muon site constraints relative to atoms in the crystal structure. Frequency histograms can then be exported, and Bayesian analysis performed. It is also possible to export crystal structure and dipole-field images in POV-Ray [61] format, for rendering publication-quality 3D graphics. Atom sizes, colours and transparencies can be varied, bonds added, and extraneous parts of the structure can be deleted for clarity.

MμCalc has been used for all dipole-field calculations performed in this thesis, and has also been used to produce all crystal structure diagrams included herein. Source code, installation notes and documentation are available online [62].

3.7 Future work

Bayesian dipole-field techniques post-dated much of the development of MμCalc, and certain applications could enjoy large computational speed increases if the program were redesigned with these Bayesian calculations in mind. For example, in Chapter 4, the Ba_2MOsO_6 system is explored in which a net ferromagnetic moment could arise from either true ferromagnetism or a canted antiferromagnetic structure. To investigate this, initially parallel moments were rotated whilst keeping the net ferromagnetic moment constant (for full details, see Sec. 4.3.2). This procedure was computationally expensive, because each incremental change in the structure required repeating the vector sum across a large Lorentz sphere of dipoles. However, a dipole-field program which initially calculated the dipolar tensor and stored its values could calculate the effects of changing the magnitude and/or direction of moments without repeating the computationally-expensive summation stage. This tensor would need to be calculated for each sublattice of moments intended to change in value independently. It may be useful to use the tensor evaluated in spherical polar coordinates, allowing the moments to be specified in terms of size and direction.

Another possibility would be investigating the consequences of different muon site constraints. All work in this thesis assumes simple spherical shells of potential muon sites at appropriate distances from negative ions, with solid spheres of exclusion around positive ones. Making the boundaries fuzzier, or somehow weighting the likelihood by electrostatic potential, might yield improved results. It would be important when pursuing this to calibrate against results in systems with known magnetic structures, in order that the resulting technique had empirical validity and not just alluring complexity.

(a)

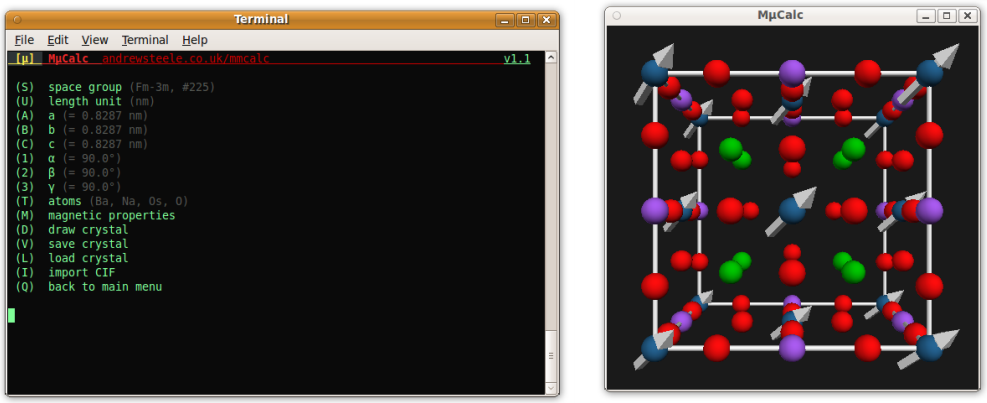

(b)

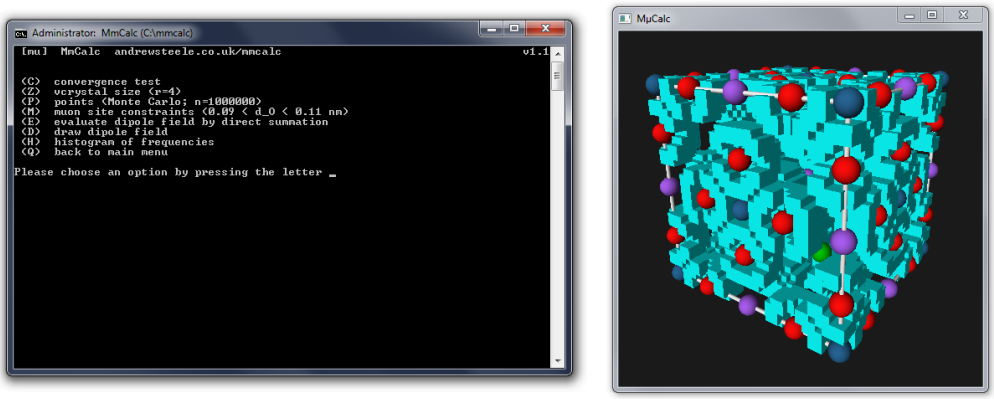

(c)

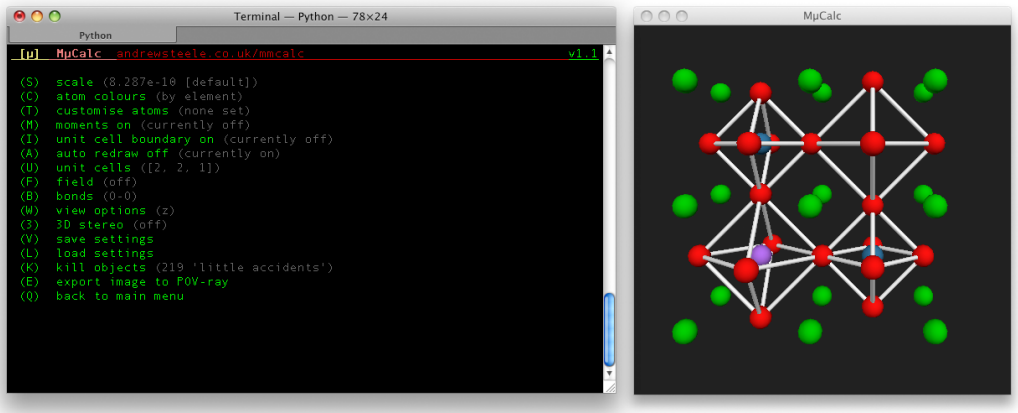

Figure 3.11: Screenshots showing MμCalc's three main menus. (a) The crystal and magnetic structure menu, shown along with the 3D Visual Python window, which displays the structure entered: in this case, ferromagnetic Ba_2NaOsO_6. (b) The dipole-field calculation menu. The 3D window here shows the volume where a muon may sit if constrained to lie approximately 0.1 nm from an oxygen ion in Ba_2NaOsO_6. (c) The visualisation menu allows detailed customisation of the appearance of crystal structures to create high-quality figures. The 3D window in this case shows the images of the Ba_2NaOsO_6 structure seen in Fig. 4.1. Images show the program running on Ubuntu Linux 10, Windows 7 and Mac OS X, respectively.

Chapter 4

Low-moment magnetism in Ba_2MOsO_6 (M = Li, Na)

Metal oxides containing 5d transition metal ions provide a wealth of novel magnetic behaviour in which orbital, charge and spin degrees of freedom play a rôle. The physics of the 5d transition metals differs from their more familiar 3d counterparts in a number of ways. Firstly, the 5d orbitals are significantly larger in spatial extent, allowing them to behave more like free electrons in many systems and reducing the effect of electron correlations. Moreover, spin–orbit coupling in 5d ions is larger because of their higher atomic number (with atomic number Z, spin–orbit interaction scales as Z^4 [34]). In 3d transition metal compounds, the spin–orbit coupling is typically rather smaller than the crystal-field splitting, but the larger spin–orbit interaction in 5d oxides contributes to a substantially different balance between energy scales.

In this context, osmium compounds provide a number of interesting examples. Osmium has oxidation states ranging from Os^{4+} ($5d^4$) to Os^{7+} ($5d^1$). The behaviour of compounds such as OsO_2, $SrOsO_3$ and $BaOsO_3$ (all containing Os^{4+}) is dominated by the large spatial extent of the orbitals; the electrons are delocalised, giving rise to Pauli paramagnetism [63]. On the other hand, the much smaller Os^{7+} ion gives rise to rather different behaviour: double perovskites of the form Ba_2(Na, Li)OsO_6 [containing Os^{7+} ions arranged on a face-centred cubic (fcc) lattice] exhibit Mott-insulating, $S = \frac{1}{2}$ local-moment behaviour [64, 65]. The insulator barium sodium osmate (Ba_2NaOsO_6) has drawn particular attention [66] due to its seemingly contradictory combination of negative Weiss temperature ($\approx -10\,\mathrm{K}$) and yet weak ferromagnetic (FM) moment ($\approx 0.2\mu_B$/formula unit) below $T_c \approx 7\,\mathrm{K}$. This contrasts with the isostructural Ba_2LiOsO_6, which has both a negative Weiss temperature and no ferromagnetic moment [64, 67]. The apparent contradiction in Ba_2NaOsO_6 raises the possibility that it is a canted antiferromagnet, although first-principles density functional theory electronic structure calculations indicate that a ferromagnetic state has lower energy [68]. The large hybridisation between the osmium 5d and oxygen 2p orbitals leads to a very large crystal-field splitting (several eV) between the e_g and t_{2g} bands. It has been suggested that the low moment arises

from a partial cancellation of orbital and spin angular momenta in the occupied spin-up t_{2g} band [68]. An alternative mechanism [69] involves the frustration of both the antiferromagnetic (AFM) interactions and the orbital ordering by the fcc lattice, resulting in a delicate balance of interactions which favours ferromagnetism for Ba_2NaOsO_6, but antiferromagnetism for Ba_2LiOsO_6. The high-temperature paramagnetic moment $\mu_{\text{eff}} \approx 0.6\mu_B$ in Ba_2NaOsO_6 is significantly lower than the $1\mu_B$ which would be expected for a free electron, and is thus indicative of substantial spin–orbit coupling [66]. The magnetic ground state of Ba_2MOsO_6 is thus a matter of significant speculation.

In view of these competing explanations, further experimental data which can distinguish between different magnetic configurations are desirable. An obvious solution to this would be to solve the magnetic structures by neutron diffraction, but these materials are not amenable to this for several reasons: firstly, osmium is a relatively strong absorber of neutrons; secondly, there is a significant probability that the M = Na compound is a ferromagnet, meaning that the magnetic peaks and structural Bragg peaks would coincide; and thirdly, the ordered moment is likely to be low, as we shall see, which would make detecting magnetic order difficult, especially if it is indeed a ferromagnet. Muon-spin relaxation provides a local probe of magnetism in Ba_2MOsO_6, and the novel Bayesian technique explained in Sec. 3.5 allows bounds to be extracted on moment size and configuration. The muon data, in combination with measured magnetisation, are consistent with the development of long-range FM order with a reduced moment in Ba_2NaOsO_6, and a reduced moment is also likely for Ba_2LiOsO_6.

The work comprising this chapter has been submitted for publication, and is available as a preprint as indicated in Ref. 70.

4.1 Structure and magnetisation

The double-perovskite structure of Ba_2NaOsO_6 is shown in Fig. 4.1; note that sodium and osmium ions inhabit alternate oxygen octahedra. The structure is described by the space group $Fm\bar{3}m$, with cubic lattice constant $a = 0.828\,70(3)$ nm. Ba_2LiOsO_6 is isostructural, slight differences arising from the fact that Li^+ is smaller than Na^+, and thus the size difference between the Li and Os octahedra is somewhat less pronounced. The lattice constant is reduced to $a = 0.810\,46(2)$ nm. Full details of both structures can be found in Ref. 64.

Magnetisation measurements using a SQUID magnetometer are shown in Fig. 4.2, and are consistent with earlier work [64, 66]. Ba_2NaOsO_6 exhibits a magnetisation curve typical of a ferromagnet with a small amount of hysteresis, approaching a saturation value of $\approx 0.2\mu_B$/formula unit, but still displaying a slight upward trend in magnetisation even at 7 T. This does not rule out canted antiferromagnetism, as the initial part of the curve could represent the alignment of net FM domains whilst the slow, near-linear increase in magnetisation represents a slow canting of spins in those domains as field is increased.

Ba_2LiOsO_6 initially displays the linear magnetisation typical of a slowly-canting antiferromagnet, but a spin-flop transition at around 5.5 T with obvious hysteresis is

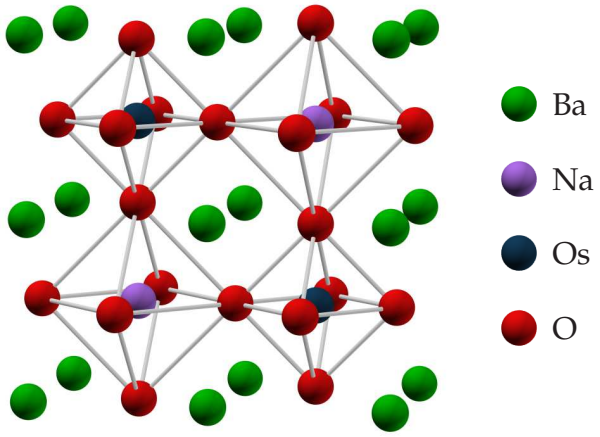

Figure 4.1: Double-perovskite crystal structure of Ba_2NaOsO_6, comprising alternating OsO_6 octahedra (top left and bottom right) and NaO_6 octahedra, with barium ions occupying the remaining space.

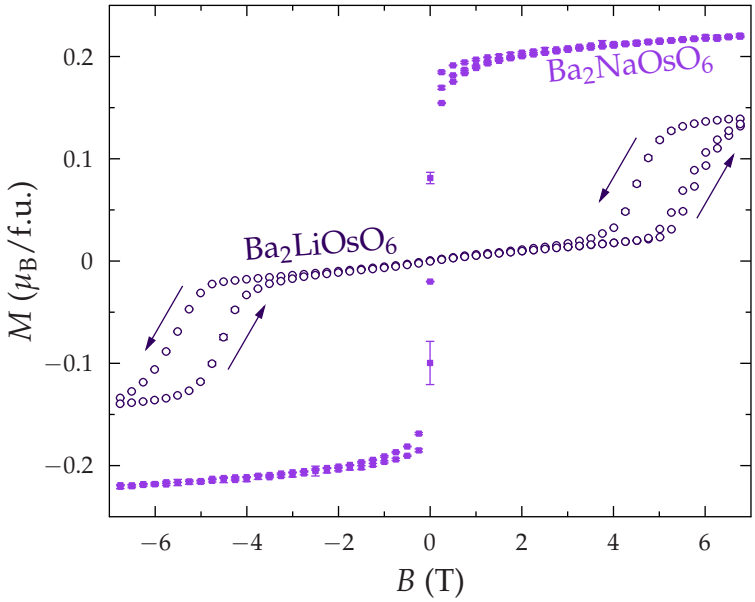

Figure 4.2: Magnetisation measured at 2 K in a SQUID magnetometer for Ba_2MOsO_6. Error bars are shown, but in most cases are smaller than the marker size.

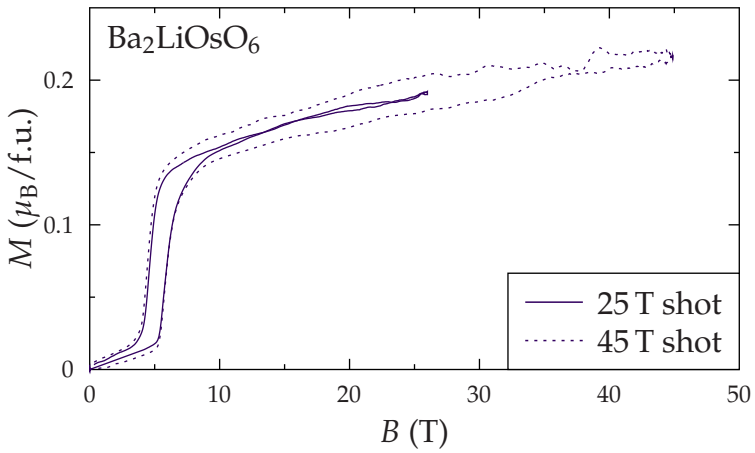

Figure 4.3: Magnetisation measured at 4 K in pulsed field for Ba_2LiOsO_6, calibrated against the SQUID magnetisation data shown in Fig. 4.2. Data from a 45 T shot (dashed line) are noisier than those from a 25 T shot (solid line) but show no evidence for additional magnetic transitions.

also evident. Pulsed field magnetometry on Ba_2LiOsO_6 suggests that this compound does not reach a saturated magnetisation value even at 45 T, and also reveals no additional transitions up to this high field (see Fig. 4.3).

4.2 Experimental methods

Crystallites of Ba_2NaOsO_6 and Ba_2LiOsO_6 were grown using a flux method [64]. Powders of Os (99.8%), $Ba(OH)_2{\cdot}8H_2O$ (98%) and high-purity $NaOH{\cdot}H_2O$ (99.996%) or LiOH (99.995%) and KOH (99.99%) were mixed in the ratio 1:2.1:300 or 1:2.1:140:75 respectively. These mixtures were each placed in an alumina crucible inside a thick quartz tube which was inserted into a 600 °C pre-heated tube furnace where it was held for 3 days. The furnace was then rapidly cooled to room temperature and small single crystals were harvested from each crucible.[1] The muon experiments used a very large number of these crystals without alignment. The measurements were performed using the GPS instrument at PSI. Samples were wrapped in 25 µm Ag foil and mounted on a flypast holder comprising two silver prongs.

4.3 μ^+SR results

4.3.1 Ba_2NaOsO_6

Typical zero-field μ^+SR spectra measured above and below the magnetic transition for Ba_2NaOsO_6 are shown in Fig. 4.4. Two damped oscillations are visible at low temperature, demonstrating the existence of a transition to a state of long-range

[1] Samples studied in this chapter were synthesised by D. Prabhakaran.

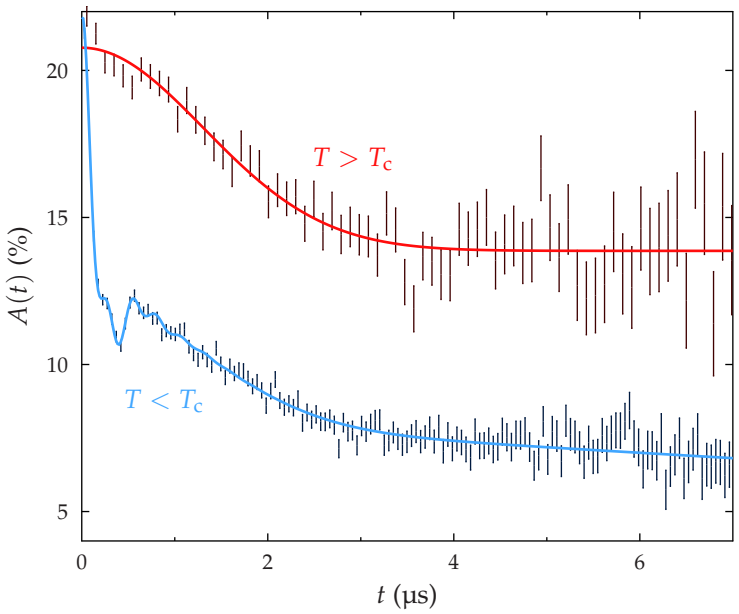

Figure 4.4: Muon data above ($T = 8\,\mathrm{K}$) and below ($T = 3\,\mathrm{K}$) the magnetic transition at $T_c = 6.8\,\mathrm{K}$ for Ba_2NaOsO_6, along with fits to Eq. (4.1) for the data below the transition, and a Gaussian relaxation for data above.

magnetic order. Data below the transition were fitted to

$$A(t) = \left[\sum_{i=1}^{2} A_i e^{-\lambda_i t} \cos\left(2\pi\nu_i t\right) + A_3 e^{-\lambda_3 t}\right] + A_{\mathrm{bg}} e^{-\lambda_{\mathrm{bg}} t}, \tag{4.1}$$

representing two oscillatory components, labelled 1 and 2; a fast-relaxing term, labelled 3, to account for the rapid initial depolarisation; and a slow-relaxing term, labelled bg, which accounts for the background arising from muons which stop in the silver sample holder or cryostat tails and the $\frac{1}{3}$ of muons which stop inside the sample with spins parallel to the local magnetic field. The frequencies of the two oscillatory components were initially left free but, after observing that they varied in proportion with one-another, they were held in fixed proportion $P_2 = \nu_2/\nu_1$ during fitting. The existence of two oscillatory components most likely indicates two crystallographically-similar muon sites, perhaps one nearer to the magnetic Os ion and the other nearer to the non-magnetic Na ion. The ratio of the probabilities of stopping in the two oscillating states $A_1/A_2 = 0.19 \pm 0.02$, and $A_3/A_2 = 0.92 \pm 0.01$. Further, $\nu_1(T \to 0) = 3.9(1)\,\mathrm{MHz}$ and $P_2 = 0.40 \pm 0.05$. The relaxation rates $\lambda_1 \approx 4\,\mathrm{MHz}$ and $\lambda_2 \approx 2\,\mathrm{MHz}$ do not vary significantly as a function of temperature, whilst λ_3 decreases from $1.6(1)\,\mathrm{MHz}$ at $1.5\,\mathrm{K}$ to zero at the transition temperature T_c. The background term varies somewhat between experimental runs, but its amplitude and relaxation rate remain approximately constant, with $A_{\mathrm{bg}}/A_2 \approx 0.75$ and $\lambda_{\mathrm{bg}} \approx 0.03\,\mathrm{MHz}$.

Since the muon-precession frequency is proportional to the local magnetic field, which is itself proportional to sample magnetisation, the precession frequency $\nu(T)$ acts as an effective order parameter for the system. The temperature evolution of

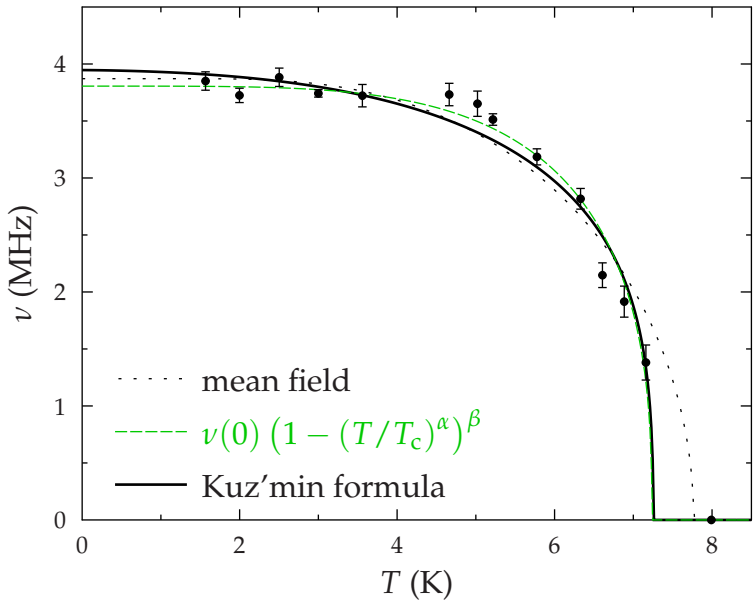

Figure 4.5: The frequency $\nu(T)$ extracted from fits to $A(t)$ spectra as a function of sample temperature T, along with fits to various models. Data are only shown for the larger frequency ν_1 because ν_2 was held in fixed proportion during fitting. The mean-field fit follows Ref. 71 and the Landau-type parameterisation of the FM equation of state is due to Kuz'min [72].

this order parameter thus allows some insight into the nature of the magnetically-ordered state. This evolution is shown in Fig. 4.5, along with fits to various different parametrisations. The temperature dependence of $\nu(T)$ fitted rather poorly to an analytic expression for a mean-field $S = \frac{1}{2}$ magnet [71],

$$\frac{M}{M_S} = \frac{e^{g_J \mu_B J \lambda M / k_B T} - \frac{1}{2}}{e^{g_J \mu_B J \lambda M / k_B T} + \frac{1}{2}} \tag{4.2}$$

where $\frac{M}{M_S}$ is the magnetisation as a fraction of the saturation magnetisation; J and g_J are the angular momentum and its associated g-factor, respectively; and λM is the mean field, proportional to the magnetisation. This might be expected since assuming that all moments are bathed in a uniform mean field is usually inappropriate in the case of magnetism driven by short-range exchange interactions. In particular, the estimated transition temperature $T_c = 7.8(2)\,\mathrm{K}$ is significantly higher than both the other fitting functions used (as is clear from Fig. 4.5) and than the previous estimate of the transition temperature, $T_c = 6.8(3)\,\mathrm{K}$, derived from heat capacity. Fitting extracted frequencies as a function of temperature to the phenomenological function

$$\nu(T) = \nu(0)\left[1 - \left(\frac{T}{T_N}\right)^{\alpha}\right]^{\beta} \tag{4.3}$$

allows an estimate of the critical temperature and the exponent β to be extracted. Leaving all parameters unconstrained does not result in a stable fit. However,

fixing $\beta = 0.367$, corresponding to the 3D Heisenberg model, yields $T_c = 7.2(2)$ K. A similarly good fit can be obtained using a Landau-type parametrisation of the equation of state of a ferromagnet (following Eq. (18) of Kuz'min [72]):

$$\frac{M^2}{M_S^2} = \frac{\left[\kappa^2 + 4\left(1-\kappa\right)\frac{1-(T/T_C)^3}{1+p(T/T_C)^{3/2}}\right]^{\frac{1}{2}} - \kappa}{2\left(1-\kappa\right)}^{\frac{1}{2}}, \tag{4.4}$$

where T is temperature and T_C is Curie temperature; and adjustable parameters $p = 0.25$ and $\kappa = 0.18$ were used, appropriate for Fe (a metallic ferromagnet). This yields the same estimate of the transition temperature as the phenomenological Eq. (4.3). The agreement with these latter two models shows that the behaviour is consistent with three-dimensional FM order.

4.3.2 Extracting magnetic moment with Bayesian analysis

Dipole-field simulations were performed for Ba_2NaOsO_6 using a variety of magnetic models, both FM and AFM (ignoring any canting) with moments orientated along [0 0 1], [0 1 1] and [1 1 1]. In the AFM cases, no propagation vector is used but instead different Os moments within the unit cell are orientated in opposite directions: those with a fractional coordinate $x = 0$ are antiparallel to those with $x = 0.5$, giving rise to [1 0 0] FM sheets. The exact magnetic structure is unknown, but varying the nature of the AFM order does not make a large difference to results, and hence an exhaustive search appears not to be necessary. Since the muon site is unknown, we adopt a probabalistic approach, and attempt to identify likely constraints on muon position. The metal ions in this system are all positively charged, meaning that the muon is unlikely to stop near them. As discussed in Chapter 3, muons have been shown to stop around 0.1 nm from an O^{2-} ion in other oxides [44, 45]. Thus, in these calculations, positions in the unit cell were generated at random and dipole fields calculated at sites which were both approximately this distance from an oxygen ion ($0.09 \leq r_{\mu\text{–O}} \leq 0.11$ nm) and not too close to a positive ion ($r_{\mu-+} \geq 0.1$ nm). The magnitudes of the resulting fields were then converted into muon precession frequencies, and the resulting histogram yields the probability density function (pdf) $f(\nu/\mu)$, evaluated as a function of precession frequency ν divided by osmium moment μ (since the precession frequency scales with the osmium moment). A subset of the results is shown in Fig. 4.6: the FM and AFM [1 1 1] configurations were identified as most likely using DFT calculations; whilst the AFM [0 0 1] shows a case with a pdf which differs markedly from those, and shows the extent of variation between these different spin configurations—and that this variation is quite small. The high-field tails, representing the muon sites approaching 0.1 nm from an osmium ion, extend to around 200 MHz/μ_B.

This analysis ignores contributions from the Lorentz field and demagnetising field, though these are likely to cancel each-other to some extent. Further, we can estimate an approximate upper bound on their magnitude by evaluating $\mu_0 M$, giving $\frac{\gamma_\mu}{2\pi}\left|\boldsymbol{B}_L + \boldsymbol{B}_{demag}\right| \lesssim 2$ MHz. The importance of the contact hyperfine field,

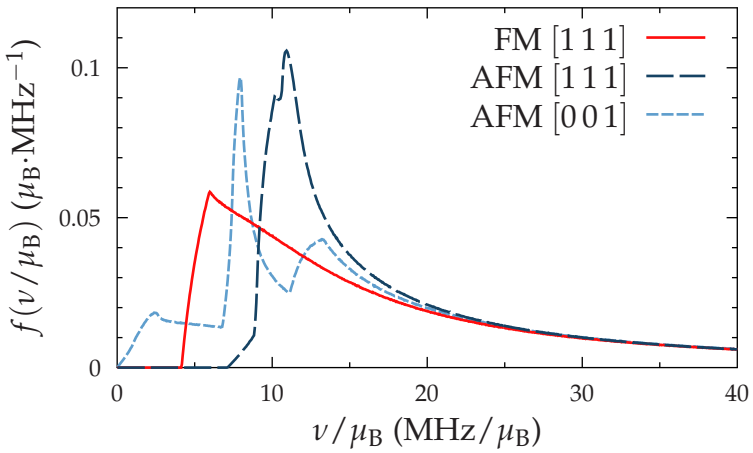

Figure 4.6: Probability density functions of muon precession frequency ν per unit magnetic moment μ under various assumed magnetic structures. Results are shown for three different magnetic structures: the direction associated with each line indicates the moment direction; AFM configurations possess FM planes along the [1 0 0] direction, as described in the text.

$\boldsymbol{B}_{\text{hyperfine}}$, is extremely difficult to evaluate (see Sec. 3.3.2) and it is neglected. However, the Os^{7+} ion is both small and positively charged, meaning that not only is the spatial extent of its spin-polarised electron cloud small, but the muon is likely to stop far from it. Thus, this contribution should not be significant, and would be even further reduced if its magnetic moment is low.

We then follow the Bayesian scheme outlined in Sec. 3.5, modified slightly due to the presence of multiple frequencies in the spectra. When multiple frequencies ν_i are observed, it is necessary to multiply their probabilities of observation in order to obtain the chance of their simultaneous observation, and so we evaluate the pdf of the magnetic moment μ given the set of observed frequencies $\{\nu_i\}$,

$$g(\mu|\{\nu_i\}) \propto \prod_i \int_{\nu_i-\Delta\nu_i}^{\nu_i+\Delta\nu_i} f(\nu_i/\mu)\,\mathrm{d}\nu_i\,, \tag{4.5}$$

where $\Delta\nu_i$ is the error on the fitted frequency, and $f(\nu/\mu)$ is the pdf of frequency per unit moment as described previously. The effect of this operation is somewhat like a convolution, and is shown in Fig. 4.7.

The results of this are shown in Fig. 4.8, and show that for all collinear magnetic structures considered a low moment is overwhelmingly likely. Furthermore, for the FM case the most probable $\mu \approx 0.2\mu_B$, consistent with the magnetisation measurements. The lowest possible moment is set by the largest value of ν/μ in the high-field tail, and is very close to zero.

Though this lends plausibility to the suggested low moment on the osmium site, it does not explicitly test for the alternative, i.e. a canted antiferromagnetic structure with a net moment. Thus, an alternative method of testing the hypothesis was attempted, considering possible canted structures which would give rise to the

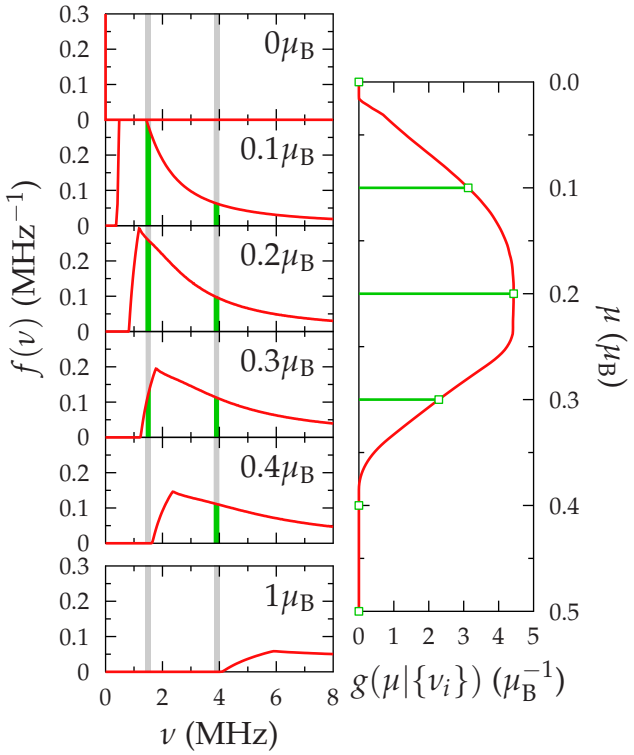

Figure 4.7: Schematic representation of the convolution-like procedure of Eq. (4.5). The column of graphs on the left shows the pdf of muon precession frequencies in Ba_2NaOsO_6 given FM $[1\,1\,1]$ structure assuming various different values of the osmium moment μ. Light grey shaded regions correspond to the observed frequencies together with their uncertainties, and the green shading then shows the integrated probability of this frequency being observed. The graph on the right, rotated by 90°, then shows the pdf of moment μ along the (vertical) x-axis. The green impulses then represent the two green areas on the corresponding left graph multiplied together. If the osmium has no moment, then muon precession would not be observed. The broad maximum at $\mu \approx 0.2\mu_B$ corresponds to the slow increase in probability of the lower frequency in tandem with the decrease in probability of the other. By $\mu = 0.4\mu_B$, it is no longer possible to observe the lower frequency and thus the probability of this moment is zero. At $\mu = \mu_B$, neither frequency is present at the muon sites examined.

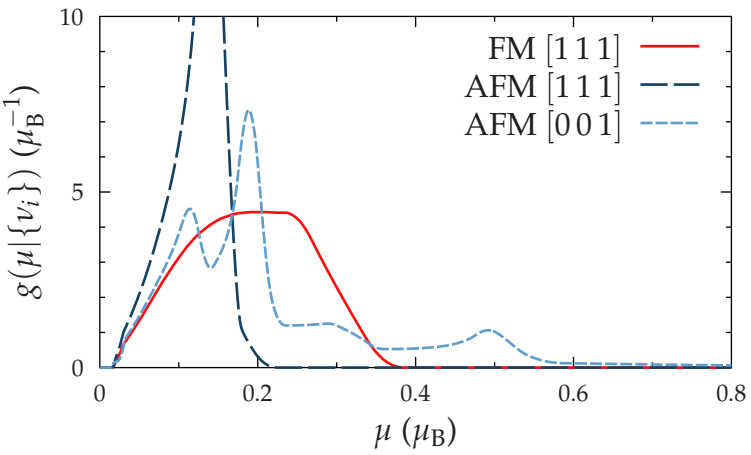

Figure 4.8: Probability density functions of osmium moment μ in Ba_2NaOsO_6 given the set of frequencies observed in muon experiments, $\{\nu_i\}$. Results are shown for three different magnetic structures: the direction associated with each line indicates the moment direction; AFM configurations possess FM planes along the [1 0 0] direction, as described in the text.

$\mu = 0.2\mu_B$ seen in bulk measurements. In these simulations, moments are counter-rotated by an angle α, subject to the constraint that $\mu \sin\alpha = 0.2\mu_B$, illustrated in Fig. 4.9 (a). The intermediate evaluation of pdfs of moment size for various different angles α is shown in Fig. 4.9 (b), and the results are shown in Fig. 4.10. They are again consistent with a reduced moment μ, certainly lower than the high-temperature paramagnetic moment of $0.6\mu_B$.

Thus, this probabilistic methodology suggests that the small magnetic moment of ordered Ba_2NaOsO_6 is likely to be true weak-moment ferromagnetism, rather than an artefact of a canted magnetic structure with larger moments. This is not an exhaustive study of possible magnetic configurations but, given the results found in the variety of trial structures examined, it is unlikely that a combination of a pathological magnetic structure and muon site could give rise to the observed precession frequencies and yet disguise a significantly larger magnetic moment on the osmium site.

4.3.3 Ba_2LiOsO_6

For Ba_2LiOsO_6, a single, heavily-damped oscillation is present at low temperature. Example data above and below the transition are shown in Fig. 4.11. The data fit to an exponentially-damped Kubo–Toyabe function,

$$A(t) = A_1 p_{KT} e^{-\lambda_1 t} + A_2 e^{-\lambda_2 t} + A_{bg}, \tag{4.6}$$

where the first component contains p_{KT}, the Kubo–Toyabe relaxation defined in Eq. (2.12); the second component represents a relaxation; and the third component is a non-relaxing background. The Kubo–Toyabe function has a fitted field width $\Delta/2\pi = 0.8(1)$ MHz at 1.5 K. As discussed in Sec. 2.4.1, this indicates a static but

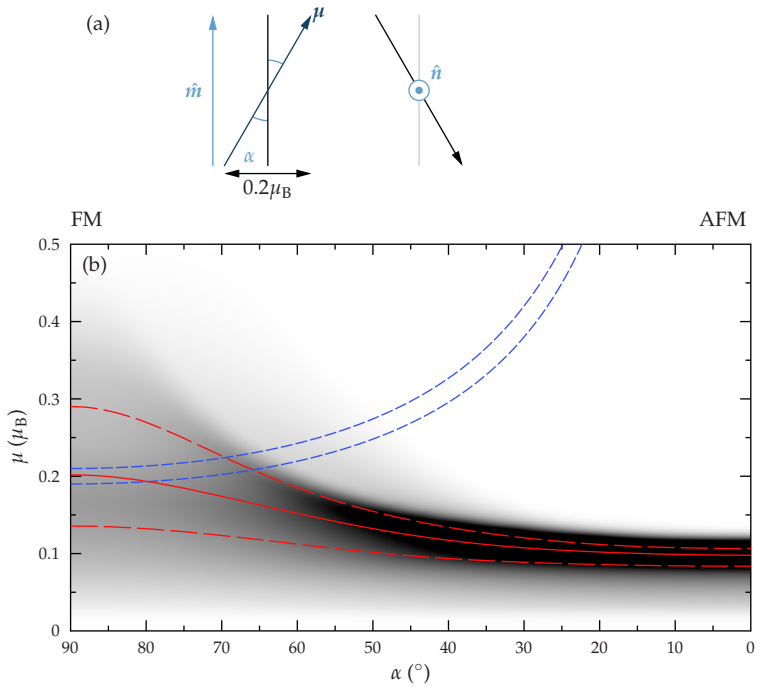

Figure 4.9: (a) Schematic representation of two initially-AFM osmium moments being counter-rotated by an angle α from an initial direction $\hat{\boldsymbol{m}}$ about a unit normal $\hat{\boldsymbol{n}}$, maintaining a projection $0.2\mu_B$ along the direction of magnetisation within the sample. (b) Probability density function of osmium moment μ as a function of canting angle α in Ba_2NaOsO_6 as moments are canted from FM order along the $[0\,0\,1]$ direction to AFM order along $[0\,1\,0]$, rotating about $[1\,0\,0]$. Density of black denotes the pdf of osmium moment size: vertical cross-sections are therefore pdfs displayed like those in Fig. 4.6. A vertical cross-section at $\alpha = 90°$ corresponds to the solid red line in Fig. 4.6. The similar vertical section at $\alpha = 0°$ does not correspond to the dashed, light blue line in Fig. 4.6 because the AFM moments are ordered in $[1\,0\,0]$ FM sheets, which breaks the symmetry between $\boldsymbol{b}$- and $\boldsymbol{c}$-orientated moments. The solid and long-dashed red lines indicate the median value of moment for a given angle, and the interquartile range, respectively. The short-dashed blue lines show the canted moment $\mu = (0.2 \pm 0.02)\mu_B / \sin\alpha$ required to obtain the desired magnetisation of $\approx 0.2\mu_B$, and thus the probability density between them gives rise to a pdf of canting angle as shown in Fig. 4.10.

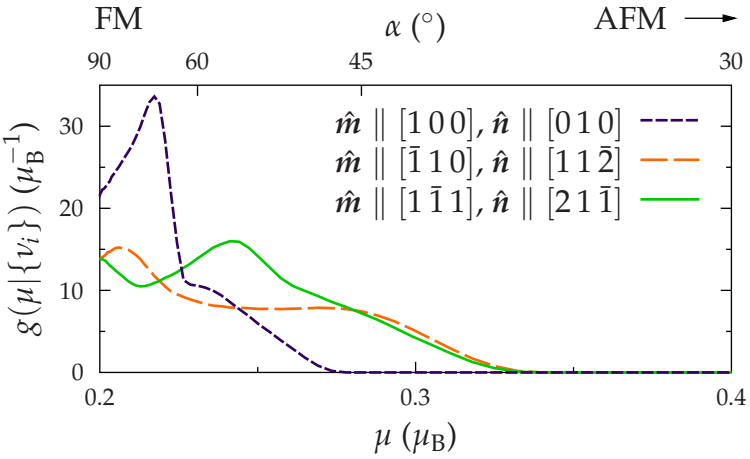

Figure 4.10: Probability density functions of osmium moment μ in Ba_2NaOsO_6 given the set of frequencies observed in muon experiments, $\{\nu_i\}$. Results are shown for three different sets of magnetic structures: AFM moments initially pointing antiparallel along the direction $\hat{\boldsymbol{m}}$ are counter-rotated as shown in Fig. 4.9 (a) around a unit vector $\hat{\boldsymbol{n}}$. AFM configurations possess FM planes along the $[1\,0\,0]$ direction, as described in the text. The moment size is scaled with their rotation to ensure that the net moment is $0.2\mu_B$.

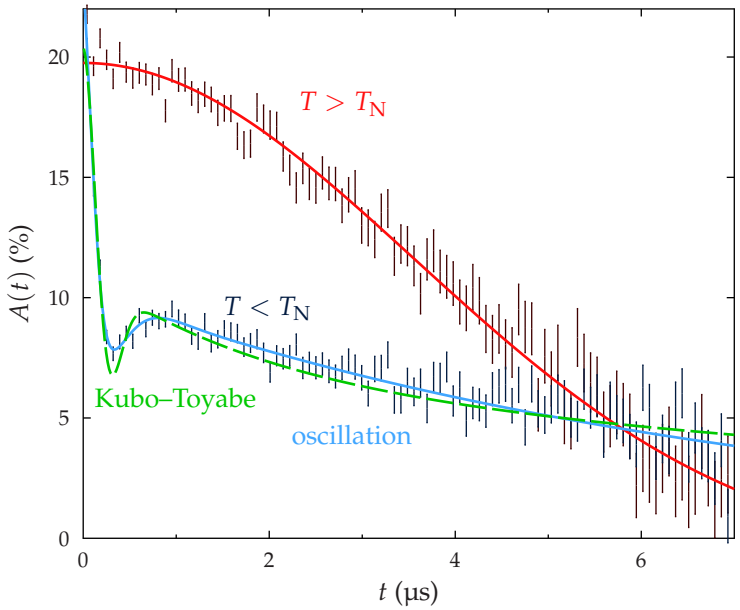

Figure 4.11: Example μ^+SR spectra above ($T = 8.4\,K$) and below ($T = 1.5\,K$) the transition temperature $T_N = 8\,K$ for Ba_2LiOsO_6. For the 1.5 K data, the dashed line is a Kubo–Toyabe fit, the solid line is a damped oscillation plus a fast-relaxing component.

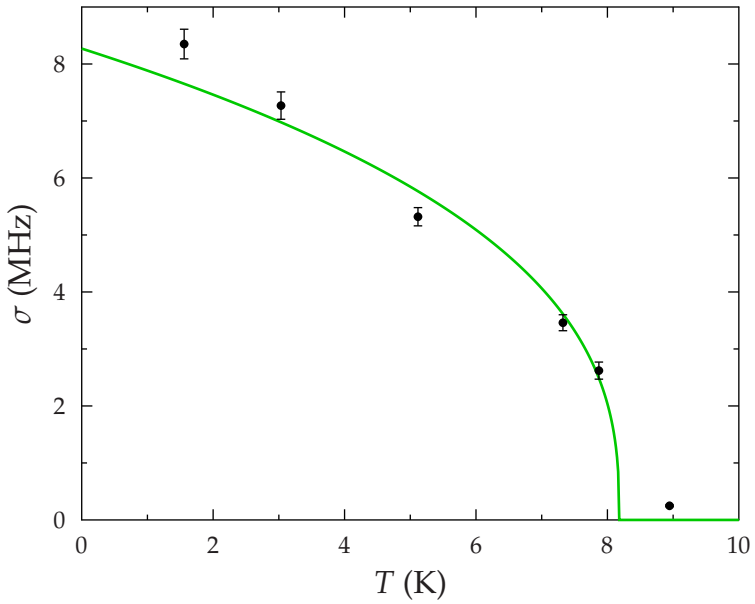

Figure 4.12: The width σ of an initial Gaussian relaxation fitted over the first 1 μs of data as a function of temperature T. Since this would be expected to scale with the internal field of the magnet, this can be used to approximately identify the transition to long-range order, which occurs at around 8 K. The line is a guide to the eye.

spatially-disordered spontaneous field. Similarly, it is possible to fit the data with a damped oscillation plus a fast-relaxing Gaussian component,

$$A(t) = A_1 \cos(2\pi\nu t)\, \mathrm{e}^{-\lambda_1 t} + A_2 \mathrm{e}^{-\sigma_2^2 t^2} + A_{\mathrm{bg}}, \tag{4.7}$$

where the first component represents a damped oscillation, the second a pure relaxation and the third component a non-relaxing background. The large relaxation on the oscillating component, $\lambda_1/2\pi = 0.84(5)\,\mathrm{MHz} \approx \nu = 1.2(1)\,\mathrm{MHz}$, indicates a wide field distribution, and thus also points to the presence of significant disorder. Following either argument, it seems that the long-range magnetic ordered state present in the sample is static, but significantly disordered. At higher temperature the relaxation function can be modelled with a Gaussian, signifying the paramagnetic state.

The fast initial relaxation is associated with the onset of long-range order, but how exactly is unclear. One possibility is that muons stop at a site with a very small average field, but a wide distribution of fields, and thus this relaxation would be expected to scale with the order parameter. Focussing only on the early-time relaxation and plotting the relaxation rate allows a crude parametrisation of the development of static fields as a function of temperature. This is shown in Fig. 4.12, and displays the magnetic transition at 8 K.

The moments in Ba_2LiOsO_6 therefore appear to be static but show a larger degree of disorder than those of the Ba_2NaOsO_6 for $T < T_N$. This makes applying the Bayesian technique more difficult, firstly because identifying a single internal

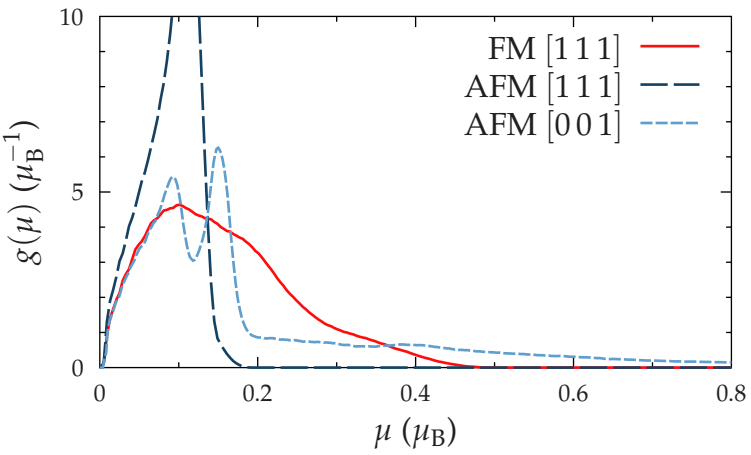

Figure 4.13: Probability density functions of osmium moment μ given the approximate local field extracted from experimental data in Ba_2LiOsO_6. Results are shown for three different magnetic structures: the direction associated with each line indicates the moment direction; AFM configurations possess FM planes along the [1 0 0] direction, as described in the text.

field is problematic, and secondly because simple magnetic structures do not give rise to such distributions of fields, and thus can only be an approximation to the true structure.

The local field at the muon site can be estimated from either the extracted Kubo–Toyabe field distribution width or the damped oscillation frequency and both are indeed similar in value. Performing a Bayesian analysis assuming that the fitted oscillation frequency at 1.5 K gives the field at the muon site allows the osmium moment size in this lithium analogue to be estimated. The distributions of muon precession frequency at muon sites near oxygen and far from positive ions are similar to those for Ba_2NaOsO_6 shown in Fig. 4.6, whilst inputting the inferred frequency gives rise to pdfs of osmium moment shown in Fig. 4.13. This analysis therefore yields a likely low moment $\lesssim 0.2\mu_B$, consistent with that measured in the spin-flop state seen in Figs. 4.2 and 4.3.

4.4 Discussion

Thus, both bulk probes in large applied field and a Bayesian analysis of zero-field μ^+SR suggest that a low moment is common to both Ba_2MOsO_6 compounds studied here. This agreement between techniques acts as both corroboration of the weak ferromagnetism proposed in the sodium osmate, and suggests that the lithium compound is not simply an unexciting AFM structural analogue since it too possesses a reduced moment. It is also a preliminary vindication of the Bayesian dipole-field technique, given the agreement between the muon-estimated moments and those inferred from SQUID and pulsed-field magnetisation measurements.

In contrast to $BaIrO_3$, which achieves a low ferromagnetic moment due to charge-

density wave formation [73], in these compounds the origin must be rather different. It has been postulated [68, 69] that the d^1 spin-moment of Os is compensated by the t_{2g} $L = 1$ orbital moment induced by the very strong spin–orbit coupling. Partial orbital quenching by the environment is thought to destroy the perfect compensation of the moment, leading to a small remaining magnetic moment. However, an important complication [69] is that the antiferromagnetic coupling between OsO_6 clusters takes place on an fcc lattice. It is therefore strongly frustrated and hence may be responsible for the sensitivity of the ground state to minor chemical changes, explaining the difference between the magnetic properties of isostructural Ba_2LiOsO_6 and Ba_2NaOsO_6.

Chapter 5

Introduction to two-dimensional molecular magnetism

In the following two chapters (Quasi–two-dimensional molecular magnets $[Cu(HF_2)(pyz)_2]X$ and Other quasi–two-dimensional molecular magnets), I will discuss a series of molecular materials which act as model systems for exploring fundamental magnetism. In particular, the structures of the compounds studied here give rise to magnetic exchange interactions which are significantly larger within planes in the materials than between those planes. These materials therefore behave approximately as collections of isolated two-dimensional magnetic layers, with a small inter-layer coupling which becomes significant at low enough temperatures. This chapter provides some introductory material relevant to both chapters, first giving a brief overview of the physics of the model being probed, the $S = \frac{1}{2}$ two-dimensional square-lattice quantum Heisenberg antiferromagnet, in Sec. 5.1; then describing molecular magnetism, concentrating on the structures examined in this thesis in Sec. 5.2; and finally, an overview is given of the methods by which we can parametrise the low dimensionality of materials in Sec. 5.3.

The work in these chapters has been published, as indicated in Ref. 74.

5.1 The $S = \frac{1}{2}$ 2D square-lattice quantum Heisenberg antiferromagnet

The $S = \frac{1}{2}$ two-dimensional square-lattice quantum Heisenberg antiferromagnet (2DSLQHA) continues to be one of the most important theoretical models in condensed matter physics [75]. Experimental realisations of the 2DSLQHA in crystals also contain an interaction between planes, so that the relevant model

describing the coupling of electronic spins $\boldsymbol{S}_i$ gives rise to the Hamiltonian[1]

$$\mathcal{H} = J \sum_{\langle i,j \rangle_{xy}} \boldsymbol{S}_i \cdot \boldsymbol{S}_j + J_\perp \sum_{\langle i,j \rangle_z} \boldsymbol{S}_i \cdot \boldsymbol{S}_j, \tag{5.1}$$

where J ($J_\perp$) is the strength of the in- (inter-) plane coupling and the first (second) summation is over neighbours parallel (perpendicular) to the 2D xy-plane. Any 2D model ($J_\perp = 0$) with continuous symmetry will not show long-range magnetic order (LRO) for $T > 0$ due to a divergence of infrared fluctuations [76, 77]. However, layered systems approximating 2D models ($J_\perp \neq 0$) will inevitably enjoy some degree of interlayer coupling and this will lead to magnetic order, albeit at a reduced temperature due to the influence of quantum fluctuations. Quantum fluctuations are also predicted to reduce the value of the magnetic moment in the ground state of the 2DSLQHA to around 60% of its classical value [75], and this reduction is often seen in the ordered moments of real materials. In layered materials that approximate the 2DSLQHA, the measurement of the antiferromagnetic ordering temperature T_N is often problematic due not only to this reduction of the magnetic moment, but also to short-range correlations that build up in the quasi-2D layers above T_N. These correlations lead to a reduction in the size of the entropy change that accompanies the phase transition, reducing the size of the anomaly in the measured specific heat [78]. It has been shown in a number of previous cases that μ^+SR measurements do not suffer from these effects and therefore represent an effective method for detecting magnetic order in complex anisotropic systems [79, 80, 81, 82].

5.2 Molecular magnetism

The rich chemistry of molecular materials allows for the design and synthesis of a wide variety of highly-tunable magnetic model systems [83]. Magnetic centres, exchange paths and the surrounding molecular groups can all be systematically modified, allowing investigation of their effects on magnetic behaviour. In particular, the existence of different exchange paths along different spatial directions can result in quasi–low-dimensional magnetic behaviour (i.e. systems with magnetic interactions constrained to act in a two-dimensional plane or along a one-dimensional chain). Such systems have the potential to better approximate low-dimensional models than many traditional inorganic materials. In addition, these molecular materials can have exchange energy scales of order $J/k_\mathrm{B} \sim 10\,\mathrm{K}$ which are accessible with typical laboratory magnetic fields [80] of $B \sim 10\,\mathrm{T}$ allowing an additional avenue for their experimental study. This contrasts with typical inorganic low-dimensional systems where the exchange is found to be $J/k_\mathrm{B} \sim 1000\,\mathrm{K}$ and fields of $B \sim 1000\,\mathrm{T}$ would be needed to significantly perturb the spin system.

It has also been shown [84, 85] that a small XY-like anisotropy exists in some molecular materials. Although $J_\perp$ is the decisive energy scale for the magnetic

[1] This Hamiltonian employs the single-J convention such that, in the case of just two $S = \frac{1}{2}$ interacting spins, the separation between the singlet and triplet energies is equal to the interaction strength J.

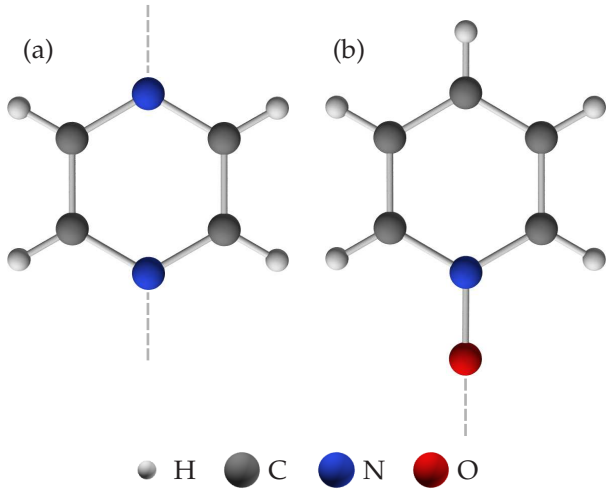

Figure 5.1: Bridging ligands used in the compounds described in this thesis: (a) pyrazine ($N_2C_4H_4$, abbreviated pyz); and (b) (ii) pyridine-*N*-oxide (C_5H_5NO, abbreviated pyo). Dashed lines indicate where the ligands bond to other parts of molecular structures.

ordering, this anisotropy has been shown to have an influence on the ordering temperature [84] and determines the shape of the low-field B–T phase diagram of these systems [85].

Several classes of molecular magnetic material closely approximate the 2DSLQHA model, and the following two chapters report the results of μ^+SR measurements performed on several such materials. These systems are self-assembled coordination polymers, based around paramagnetic ions such as Cu^{2+}, linked by neutral bridging ligands and coordinating anion molecules. The materials are based on combinations of three different ligands: (i) pyrazine ($N_2C_4H_4$, abbreviated pyz) and (ii) pyridine-*N*-oxide (C_5H_5NO, abbreviated pyo), both of which are planar rings; and (iii) the linear bifluoride ion [$(HF_2)^-$], which is bound by strong hydrogen bonds F···H···F. The pyz and pyo ligands are shown in Fig. 5.1.

Specifically, Chapter 6 discusses the molecular system $[M(HF_2)(pyz)_2]X$, where M^{2+} = Cu^{2+} is the transition metal cation and X^- is one of various anions (e.g. BF_4^-, ClO_4^-, PF_6^- *etc.*). Chapter 7 then reports the results of measurements on other quasi-2D systems. First, $[Cu(pyz)_2(pyo)_2]Y_2$, with Y^- = BF_4^- or PF_6^-, in which pyo ligands bridge $Cu(pyz)_2$ planes. Then, the quasi-2D non-polymeric compounds $[Cu(pyo)_6]Z_2$, where Z^-=BF_4^-, ClO_3^- or PF_6^- are examined. Materials in which either Ni^{2+} ($S = 1$) or Ag^{2+} ($S = \frac{1}{2}$) form the magnetic species in the quasi-2D planes rather than Cu^{2+} are also investigated.

5.3 Parametrising exchange anisotropy

In order to assess the extent to which these systems approximate the 2DSLQHA, we can quantify their dimensionality by comparing the transition temperature T_N to

the exchange parameter J. The temperature T_N can be extracted using μ^+SR, whilst J can be obtained reliably from pulsed-field magnetisation measurements [80], heat capacity or magnetic susceptibility. Further, quantum Monte Carlo simulations allow this to be related to the interlayer exchange $J_\perp$, and the correlation length of quantum fluctuations, ξ.

Mean-field theory predicts a simple relationship for the ratio of the transition temperature T_N and the exchange J given by [34]

$$\frac{k_B T_N}{J} = \frac{2}{3} z S(S+1), \tag{5.2}$$

where k_B is Boltzmann's constant, z is the number of nearest neighbours and S is the spin of the magnetic ions. In the pseudocubic $[Cu(HF_2)(pyz)_2]X$ systems, $S = \frac{1}{2}$ and $z = 6$, and Eq. (5.2) yields $k_B T_N/J = 3$. However, the reduced dimensionality increases the prevalence of quantum fluctuations, depressing the transition temperature, and in $[Cu(HF_2)(pyz)_2]BF_4$ we find $k_B T_N/J \approx 0.25$, which is indicative of large exchange anisotropy.

Combining the experimental measures of T_N and J with the results of quantum Monte Carlo (QMC) simulations allows us to deduce the exchange anisotropy $J_\perp/J$ in the system [80]. Specifically, QMC simulations [86] for 2DSLQHA where $10^{-3} \leq J_\perp/J \leq 1$ are well described by the expression

$$\frac{J_\perp}{J} = e^{b - 4\pi\rho_s/T_N}, \tag{5.3}$$

where ρ_s is the spin stiffness and b is a numerical constant. For $S = \frac{1}{2}$, the appropriate parameters are $\rho_s/J = 0.183$ and $b = 2.43$. This expression allows a better estimate of $k_B T_N/J$ in a 3D magnet: evaluating for $J_\perp/J = 1$ yields $k_B T_N/J = 0.95$. This is lower than the crude mean-field estimate because mean-field theory takes no account of fluctuations. Estimates of J for our materials, from pulsed magnetic field studies except where noted, along with calculated $J_\perp/J$ ratios, are shown in the summary tables throughout these chapters.

Another method of parametrising the exchange anisotropy is to consider the predicted correlation length of two-dimensional correlations in the layers at the temperature at which we observe the onset of LRO. The larger this length, the better isolated the layers can be supposed to be. This can be estimated by combining an analytic expression for the correlation length in a pure 2DSLQHA [87], ξ_{2D}, with quantum Monte Carlo simulations to obtain an expression [88, 89] appropriate for $1 \leq \xi_{2D}/a \leq 350,000$,

$$\frac{\xi_{2D}}{a} = 0.498 e^{1.131 J/k_B T} \left[1 - 0.44 \left(\frac{k_B T}{J} \right) + \mathcal{O}\left(\frac{k_B T}{J} \right)^2 \right], \tag{5.4}$$

where a is the square lattice constant, and T is the temperature. This formula yields $\xi_{2D}(T_N) \approx 0.5a$ for the mean-field model ($k_B T_N/J = 3$), and $\xi_{2D}(T_N) \approx a$ for $k_B T_N/J = 0.95$ from quantum Monte Carlo simulations [i.e. Eq. (5.3) with $J_\perp/J = 1$]. By comparison, in $[Cu(HF_2)(pyz)_2]BF_4$ Eq. (5.4) gives $\xi_{2D}(T_N) \approx 50a$, showing a dramatic increase in the size of correlated regions which build up in the quasi-2D layers before the onset of LRO.

Chapter 6

Quasi–two-dimensional molecular magnets $[Cu(HF_2)(pyz)_2]X$

The synthesis of the $[M(HF_2)(pyz)_2]X$ system [90, 80, 91] represented the first example of the use of a bifluoride building block to make a three-dimensional coordination polymer. This class of materials possesses a highly stable structure due to the exceptional strength of the bifluoride hydrogen bonds. The structure of the $[M(HF_2)(pyz)_2]X$ system [90, 91] comprises infinite 2D $[M(pyz)_2]^{2+}$ sheets which lie in the ***ab***-plane, with bifluoride ions $(HF_2)^-$ above and below the metal ions acting as bridges between the planes, to form a pseudocubic network. The X^- anions occupy the body-centre positions within each cubic pore. An example structure, for $[Cu(HF_2)(pyz)_2]PF_6$, is shown in Fig. 6.1. Samples are produced in polycrystalline form via aqueous chemical reactions between MX_2 salts and stoichiometric amounts of ligands. Preparation details for the compounds are reported in Refs. 90, 91, 92.[1]

In this section we consider those materials where the M cations are Cu^{2+} $3d^9$ $S = \frac{1}{2}$ centres. It is thought that the magnetic behaviour of these materials results from the $3d_{x^2-y^2}$ orbital of the Cu at the centre of each CuN_4F_2 octahedron lying in the CuN_4 plane, so that the spin exchange interactions between neighbouring Cu^{2+} ions occur through the s-bonded pyz ligands [90]. The interplane exchange through the HF_2 bridges connecting two Cu^{2+} ions should be very weak as these bridges lie on the 4-fold rotational axis of the Cu $3d_{x^2-y^2}$ magnetic orbital, resulting in limited overlap with the fluorine p_z orbitals. Therefore to a first approximation, the magnetic properties of $[M(HF_2)(pyz)_2]X$ can be described in terms of a 2D square lattice.

Measurements for X^- = BF_4^-, ClO_4^- and SbF_6^- were made using the MuSR spectrometer at ISIS, whilst PF_6^-, AsF_6^-, NbF_6^- and TaF_6^- were measured using GPS at PSI.

[1] Samples studied in this chapter were synthesised by J. L. Manson and J. A. Schleuter.

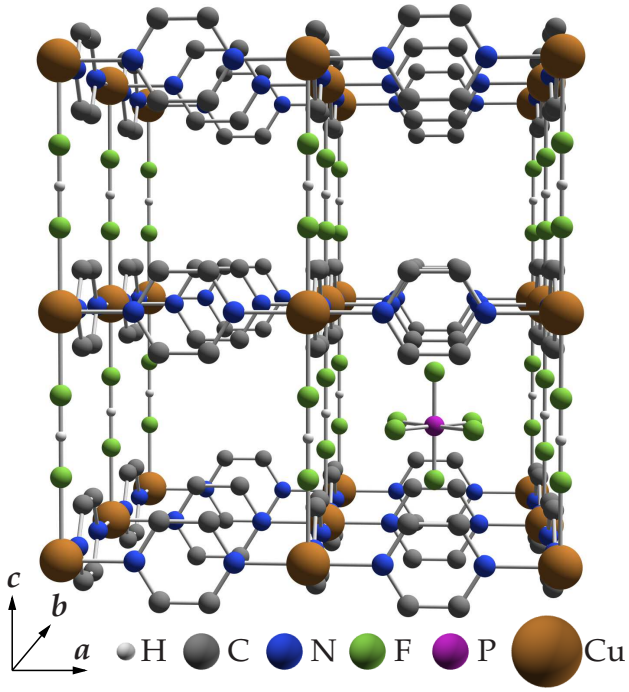

Figure 6.1: The structure of $[Cu(HF_2)(pyz)_2]PF_6$, as an example of the $[M(HF_2)(pyz)_2]X$ series. Copper ions are joined in a 2D square lattice by pyrazine ligands to form $Cu(pyz)_2^{2+}$ sheets; the 2D layers are joined in the third dimension by HF_2^- groups, making a pseudocubic 3D structure; and this structure is stabilised by a PF_6^- anion at the centre of each cubic pore. For clarity, hydrogen atoms attached to pyrazine rings have been omitted, and only one PF_6^- anion is shown.

6.1 Long-range magnetic order

The main result of our measurements on these systems is that, below a critical temperature T_N, oscillations in the asymmetry spectra $A(t)$ are observed at two distinct frequencies, for all materials in the series. This shows unambiguously that each of these materials undergoes a transition to a state of LRO. Example asymmetry spectra are shown in the left-hand column of Figs. 6.2 and 6.3. They were found to be best fitted with a relaxation function

$$\begin{aligned} A(t) = \; A_0 \; & \Big[p_1 e^{-\lambda_1 t} \cos(2\pi\nu_1 t + \phi_1) \\ & + p_2 e^{-\lambda_2 t} \cos(2\pi P_2 \nu_1 t + \phi_2) + p_3 e^{-\lambda_3 t} \Big] \\ & + A_{bg} e^{-\lambda_{bg} t}, \end{aligned} \tag{6.1}$$

where A_0 represents the contribution from those muons which stop inside the sample and A_{bg} accounts for a relaxing background signal due to those muons that stop in the silver sample holder or cryostat tails, or with their spin parallel to the local field. Of those muons which stop in the sample, p_1 indicates the weighting of the component in an oscillating state with frequency ν_1; p_2 is the weighting of a lower-frequency oscillating state with frequency ν_2; and p_3 represents the weighting

X	ν_1 (MHz)	ν_2 (MHz)	λ_3 (MHz)	p_1	p_2	p_3	ϕ_1 (°)	ϕ_2 (°)	T_N	β	α	J/k_B (K)	$\lvert J_\perp/J\rvert$
BF_4	3.30(6)	0.95(3)	8	15	15	70	−57(1)	26(2)	1.54(2)	0.18(4)	1.6(7)	6.3	9×10^{-4}
ClO_4	3.2(1)	0.64(1)	8	2	2	96	−94(1)	104(4)	1.91(1)	0.25(2)	2.6(3)	7.3	2×10^{-3}
PF_6	3.89(6)	2.23(5)	25	30	30	40	−53(3)	37(6)	4.37(2)	0.26(2)	1.5(3)	12.4	1×10^{-2}
AsF_6	3.49(9)	2.15(2)	40	25	25	50	−14(2)	14(3)	4.32(3)	0.23(3)	1.6(5)	12.8	1×10^{-2}
SbF_6	3.51(2)	2.14(2)	-	50	50	-	−46(3)	−20(2)	4.29(1)	0.34(2)	2.8(3)	13.3	9×10^{-3}
NbF_6	3.33(7)	2.36(5)	1	40	20	40	0	−30(5)	4.28(1)	0.33(3)	2.0(4)	-	-
TaF_6	3.33(9)	2.21(5)	-	50	50	-	0	0	4.22(1)	0.25(1)	1.5(3)	-	-

Table 6.1: Fitted parameters for molecular magnets in the $[Cu(HF_2)(pyz)_2]X$ family. The first parameters shown relate to fits to Eq. (6.1), which allow us to derive frequencies at $T = 0$, ν_i; probabilities of stopping in the various classes of stopping site, p_i, in percent; and phases associated with fitting the oscillating components ϕ_i. Then, the temperature dependence of ν_i is fitted with Eq. (6.2), extracting values for the Néel temperature, T_N, critical exponent β and parameter α. Finally, the quoted J/k_B is obtained from pulsed-field experiments [80], and the ratio of inter- to in-plane coupling, $J_\perp/J$, is obtained by combining T_N and J with formulae extracted from quantum Monte Carlo simulations (see Sec. 5.3, and Ref. 80). Dashes in the λ_3 column for the SbF_6 and TaF_6 compounds indicate that no fast-relaxing component was used to fit those data. Dashes in the J/k_B and $J_\perp/J$ columns for NbF_6 and TaF_6 indicate a lack of pulsed-field data for these materials.

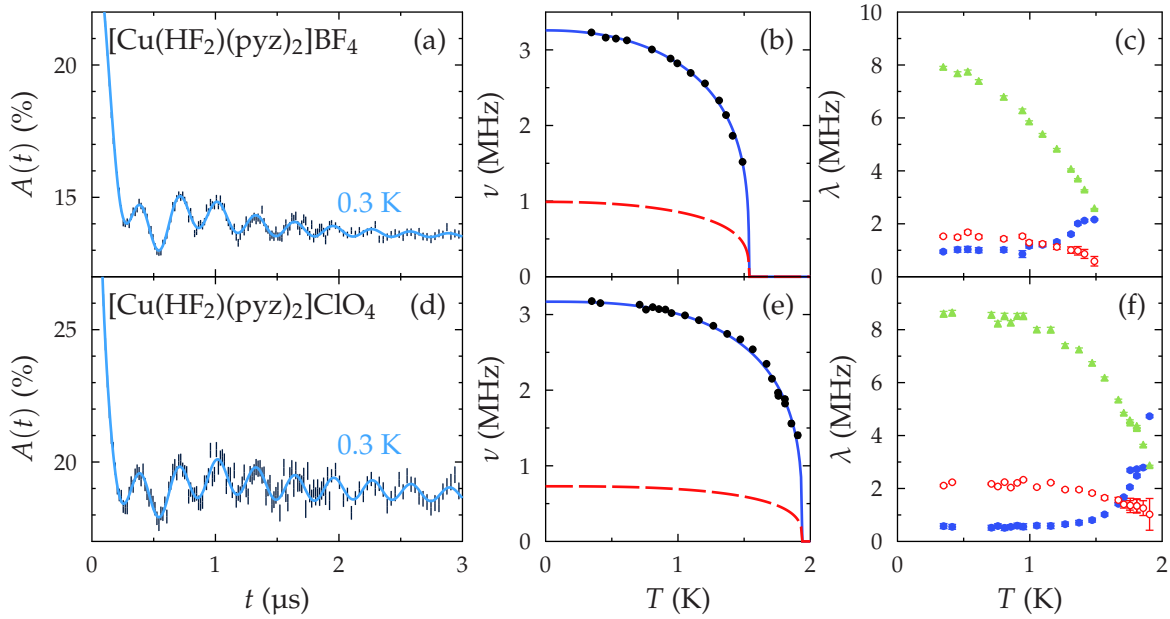

Figure 6.2: Data and the results of fits to Eq. (6.1) for $[Cu(HF_2)(pyz)_2]X$ magnets with tetrahedral anions X^-. From left to right: (a) and (d) show sample asymmetry spectra $A(t)$ for $T < T_N$ along with a fit to Eq. (6.1); (b) and (e) show frequencies as a function of temperature [no data points are shown for the second line because this frequency ν_2 was held in fixed proportion to the first, ν_1 (see text)]; and (c) and (f) show relaxation rates λ_i as a function of temperature. In the $\nu(T)$ plot, error bars are included on the points but in most cases they are smaller than the marker being used. The blue solid line representing ν_1 in (b) and (e) corresponds to the blue filled circles in the third column of graphs [(c) and (f)] for that component's relaxation, λ_1, whilst the red dashed line and red unfilled circles correspond to ν_2 and λ_2, respectively. The green filled triangles correspond to the fast relaxation λ_3.

of a component with a large relaxation rate λ_3. All parameters were initially left free to vary. The second frequency was found to vary with temperature in fixed proportion to ν_1 via $\nu_2 = P_2\nu_1$ for each material. The parameter P_2 was identified by fitting the lowest-temperature $A(t)$ spectra where Eq. (6.1) would be expected to most accurately describe the data, and subsequently held fixed during the fitting procedure. Phase factors ϕ_i were also found to be necessary in some cases to obtain a reliable fit. The parameters resulting from these fits are listed in Table 6.1, and data with fits are shown in Figs. 6.2 and 6.3. We also note here that the discontinuous nature of the change in all fitted parameters and the form of the spectra at T_N strongly suggest that these materials are magnetically ordered throughout their bulk.

The frequencies and relaxation rates as a function of temperature extracted from these fits are shown in the central column of Figs. 6.2 and 6.3. The muon precession frequency, which is proportional to the internal field in the material, can be considered an effective order parameter for the system. Consequently, fitting

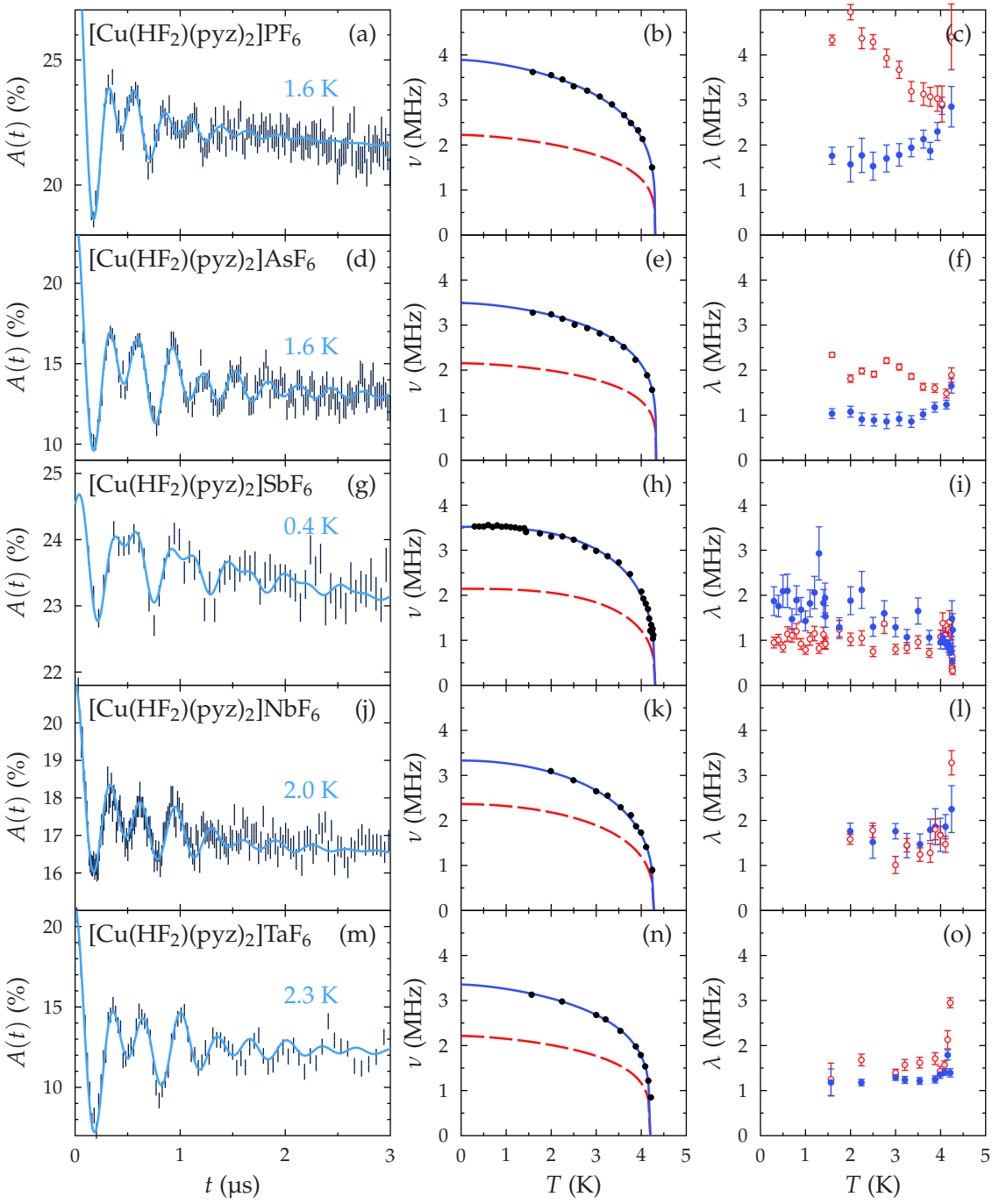

Figure 6.3: Example data and fits for $[Cu(HF_2)(pyz)_2]X$ magnets with octahedral anions X^-. From left to right: (a), (d), (g), (j) and (m) show sample asymmetry spectra $A(t)$ for $T < T_N$ along with a fit to Eq. (6.1); (b), (e), (h), (k) and (n) show frequencies as a function of temperature [no data points are shown for the second line because this frequency ν_2 was held in fixed proportion to the first, ν_1 (see text)]; and (c), (f), (i), (l) and (o) show relaxation rates λ_i as a function of temperature. In the $\nu(T)$ plot, error bars are included on the points but in most cases they are smaller than the marker being used. The blue solid line representing ν_1 in (b), (e), (h), (k) and (n) corresponds to the blue filled circles in the third column of graphs [(c), (f), (i), (l) and (o)] for that component's relaxation, λ_1, whilst the red dashed line and red unfilled circles correspond to ν_2 and λ_2, respectively.

extracted frequencies as a function of temperature to the phenomenological function

$$\nu(T) = \nu(0)\left[1 - \left(\frac{T}{T_N}\right)^{\alpha}\right]^{\beta}, \tag{6.2}$$

allows an estimate of the critical temperature and the exponent β to be extracted. Our results fit well with a previous observation [80] that the compounds divide naturally into two classes: those with tetrahedral anions $X^- = BF_4^-$, ClO_4^- and those with octahedral anions $X^- = AF_6^-$. The tetrahedral compounds have lower transition temperatures $T_N \lesssim 2$ K, as compared to the octahedral compounds' $T_N \gtrsim 4$ K; and the tetrahedral compounds also display slightly lower oscillation frequencies than their octahedral counterparts [80].

This difference has been explained in terms of differences in the crystal structure between the two sets of compounds. Firstly, the octahedral anions are larger than their tetrahedral counterparts. Secondly, the pyrazine rings are tilted by differing amounts with respect to the normal to the 2D layers: those in the octahedral compounds are significantly more upright. Since the Cu $3d_{x^2-y^2}$ orbitals point along the pyrazine directions, these tilting angles might be expected, to first order, to make little difference to nearest-neighbour exchange because such rotation is about a symmetry axis as viewed from the copper site. However, it may be that the different direction of the delocalised orbitals above and below the rings through which exchange probably occurs, possibly in conjunction with hybridisation with the anion orbitals, results in an altered next-nearest neighbour or higher-order interactions, changing the transition temperature.

Within the tetrahedral compounds, the difference in the weighting of the oscillatory component $(p_1 + p_2)$ in $X^- = BF_4^-$ and ClO_4^- probably results from the difficulty in fitting the fast-relaxing component. Even with little change in the size of the oscillations, any error in assigning the magnitude of this component will affect the proportion of the $A(t)$ signal attributed to them. This difficulty is partly due to the resolution-limited nature of ISIS arising from the pulsed beam structure. In the octahedral compounds, $X^- = SbF_6^-$ and TaF_6^- do not appear to have a resolvable fast-relaxing component, and consequently p_3 was set to zero during the fitting procedure. This is reflected by dashes in the p_3 and λ_3 columns in Table 6.1.

The fact that two oscillatory frequencies are observed points to the existence of at least two magnetically distinct classes of muon site. In general it is found that $p_1 \approx p_2$ for these materials, making the probability of occupying the sites giving rise to magnetic precession approximately equal. The weightings $p_{1,2}$ were found to be significantly less than the weighting p_3 relating to the fast-relaxing site. This, in combination with the magnitude of the fast relaxation $\lambda_3(T = 0) \gtrsim 10$ MHz, suggests that this term should not be identified with the $\frac{1}{3}$-tail which results from muons with spins parallel to their local field. (If that were the case then we would expect $(p_1 + p_2)/p_3 = 2$, which is not observed.) It is likely that each of the components, p_1, p_2 and p_3, therefore reflect the occurrence of a separate class of muon site in this system. The possible positions of these three classes of site are investigated in Sec. 6.4.

The temperature evolution of the relaxation rates λ_i is shown in the right-hand columns of Figs. 6.2 and 6.3. In the fast-fluctuation limit, the relaxation rates are expected [28] to vary as $\lambda \propto \Delta^2\tau$, where $\Delta = \sqrt{\gamma_\mu^2\langle(B - \langle B\rangle)^2\rangle}$ is the second moment of the local magnetic field distribution (whose mean is $\langle B\rangle$) in frequency units, and τ is the correlation time. In all measured materials, the relaxation rate λ_1, corresponding to the higher oscillation frequency, starts at a small value at low temperature and increases as T_N is approached from below. This is the expected temperature-dependent behaviour and most likely reflects a contribution from critical slowing down of fluctuations near T_N (described e.g. in Ref. 93). In contrast, the relaxation rate λ_2 (associated with the lower frequency) starts with a higher magnitude at low temperature and decreases smoothly as the temperature is increased. This is also the case for the relaxation rate λ_3 of the fast-relaxing component. This smooth decrease of these relaxation rates with temperature has been observed previously in magnetic materials [36, 94] and seems to roughly track the magnitude of the local field. It is possible that muon sites responsible for λ_1 and λ_3 lie further from the 2D planes than those sites giving rise to λ_2, and are thus less sensitive to 2D fluctuations, reducing the influence of any variation in τ. The temperature evolution of λ_1 and λ_3 might then be expected to be dominated by the magnitude of Δ, which scales with the size of the local field and would therefore decrease as the magnetic transition is approached from below.

The need for nonzero phases ϕ_i has been identified in previous studies of molecular magnets [81, 95, 96, 82], but never satisfactorily explained. One possible explanation for these might be that the muon experiences delayed state formation. However, the simplest model of this can be ruled out as the phases appear not to correlate with ν_i. Such a correlation would be expected since a delay of t_0 before entering the precessing state would give rise to a component of the relaxation function $a_i(t) = \cos[2\pi\nu_i(t + t_0)] = \cos(2\pi\nu_i t + \phi_i)$, with $\phi_i \propto \nu_i$, which is not observed. This does not completely rule out delayed state formation, as t_0 could be a function of temperature (although this seems unlikely at these temperatures). Nonzero phases are also sometimes observed when attempting to fit data with cosinusoidal relaxation functions from systems having incommensurate magnetic structures. The phase then emerges as an artefact of fitting, as a cosine with a $\frac{\pi}{4}$ phase shift approximates the zeroth-order Bessel function of the first kind, $J_0(\omega t)$, which is obtained from μ^+SR of an incommensurately-ordered system [26, 97]. The Bessel function arises because the distribution of fields seen by muons at sites is asymmetric. However, attempts to fit the data with a pair of damped Bessel functions produced consistently worse fits than fits to Eq. (6.1), suggesting that a simple incommensurate structure is not a satisfactory explanation. It is also possible that several further magnetically-inequivalent muon sites exist, resulting in multiple, closely-spaced frequencies which give the spectra a more complex character which is not reflected in the fitting function. The simpler relaxation function would then obtain a better fit if the phase were allowed to vary. This has been observed, for example, in $LiCrO_2$ [41]. A final possibility is that the distribution of fields at muon sites is asymmetric for another reason, perhaps arising from a complex magnetic structure. This may give rise to a Fourier transform which is only able to be fitted

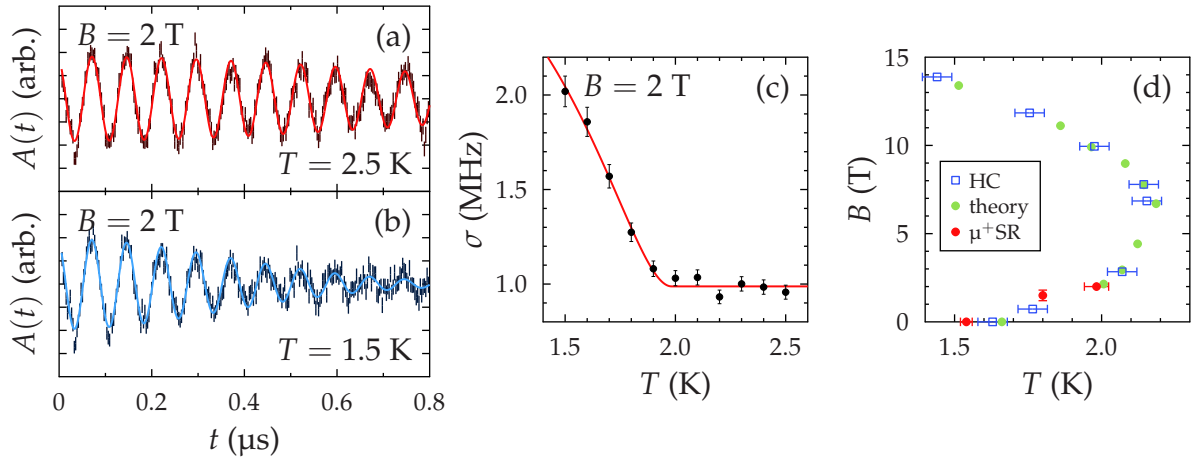

Figure 6.4: Sample TF μ⁺SR data measured for $[Cu(HF_2)(pyz)_2]BF_4$ in an applied field of 2 T are shown in (a) and (b). Data are shown in the 'rotating reference frame', rotating at $\gamma_\mu \times 1.9\ \text{T} = 257$ MHz, nearly cancelling out spin precession induced by the 2 T applied transverse field. (c) The evolution of the magnetic broadening σ with T, showing a magnetic transition at 1.98 K in 2 T. (d) The B–T phase diagram from Ref. 85 showing the nonmonotonic behaviour at low applied magnetic field. In the key, HC is heat capacity, theory represents the results of computational modelling, and μ⁺SR shows our results from TF measurements (see main text).

with phase-shifted cosines. However, the mechanism by which this would occur is unclear.

6.2 Nonmonotonic field dependence of T_N

Although the interplane exchange coupling $J_\perp$ is expected to have a large amount of control of the thermodynamic properties of these materials, it may be the case that single-ion anisotropies are also responsible for deviations in the behaviour of our materials from the predictions of the 2DSLQHAF model. In particular, these anisotropies have been demonstrated to show a crossover to magnetic behaviour consistent with the 2D XY model [84]. It was recently reported [85] that $[Cu(HF_2)(pyz)_2]BF_4$ exhibits an unusual nonmonotonic dependence of T_N as a function of applied magnetic field B [see Fig. 6.4 (d)]. This behaviour was explained as resulting from the small XY-like anisotropy of the spin system in these systems. The physics of the unusual field-dependence then arises due to the dual effect of B on the spins, both suppressing the amplitude of the order parameter by polarising the spins along a given direction, and also reducing the phase fluctuations by changing the order parameter phase space from a sphere to a circle. A more detailed explanation for the behaviour [85] reveals that the energy scales of the physics are controlled by a Kosterlitz–Thouless-like mechanism, along with the interlayer exchange interaction $J_\perp$.

The measurement of the B–T phase diagram in $[Cu(HF_2)(pyz)_2]BF_4$ reported in Ref. 85 was made by observing a small anomaly in specific heat. In order to test whether the phase boundary could be determined using muons, transverse-field (TF) μ^+SR measurements were carried out using the LTF instrument at SμS. In these measurements, the field is applied perpendicular to the initial muon spin direction, causing a precession of the muon-spins in the sum of the applied and internal field directed perpendicular to the muon-spin orientation (see Sec. 2.4.2). Example TF spectra measured in a field of 2 T are shown in Fig. 6.4 (a) and (b). The spectra are well described by a function

$$A(t) = A(0)\mathrm{e}^{-\sigma^2 t^2/2}\cos(2\pi\nu t + \phi), \tag{6.3}$$

where the phase factor depends on the details of the detector geometry, and σ is proportional to the second moment of the internal field distribution via $\sigma^2 = \gamma_\mu^2\langle B^2\rangle$. Upon cooling through T_N a large increase in σ is observed, as shown in Fig. 6.4 (c). This approximately resembles an order parameter, and the discontinuity at the onset of the increase is identified with T_N by fitting σ with the above-T_N relaxation adding in quadrature to the additional relaxation present below the transition. The resulting point at $T_N(B = 2\,\mathrm{T}) = 1.98(4)$ K is shown to be consistent with the predicted low-field phase boundary in Fig. 6.4 (d). A further point, identifiable by its vertical rather than horizontal error bar, was found by performing a field scan at a fixed temperature of $T = 1.8$ K. The field-dependence of the relaxation rate shows a sharp increase at the transition, at $B = 1.5 \pm 0.3$ T.

Points derived from μ^+SR measurements possibly lie slightly lower in T than both that predicted by theory, and the line predicted on the basis of the specific heat measurements. The theoretical calculations use $J/k_B = 5.9$ K and $J_\perp/J = 2.5 \times 10^{-3}$, whilst our estimates suggest $J/k_B = 6.3$ K and $J_\perp/J = 0.9 \times 10^{-3}$. Performing these calculations for a purely 2D system results in the entire curve shifting to the left [85], and consequently the leftward shift of our data points is consistent with our finding of increased exchange anisotropy. It is clear that the TF μ^+SR technique may be used in future to measure the B–T phase diagram and enjoys some of the same advantages it has in zero field over specific heat and magnetic susceptibility in anisotropic systems.

6.3 Muon response in the paramagnetic phase

Above T_N, the character of the measured spectra changes considerably and lower-frequency oscillations characteristic of the dipole–dipole interaction between muons and fluorine nuclei [98] are observed. The Cu^{2+} electronic moments, which dominate the spectra for $T < T_N$, are disordered in the paramagnetic regime and fluctuate very rapidly on the muon time scale. They are therefore motionally narrowed from the spectra, leaving the muon sensitive to the quasi-static nuclear magnetic moments.

M	X	$r_{\mu\text{–F}}$ (nm)	p_1 (%)	σ (MHz)	T (K)
Cu	BF_4	0.1038(1)	77(1)	0.29(1)	5.1
Cu	ClO_4	0.1081(2)	70(1)	0.37(1)	5.1
Cu	PF_6	0.1044(2)	74(2)	0.29(2)	5.2
Cu	AsF_6	0.1043(3)	78(2)	0.31(3)	4.9
Cu	SbF_6	0.1047(2)	64(1)	0.30(1)	5.0
Cu	BF_4	0.1042(1)	76(1)	0.26(1)	26
Cu	ClO_4	0.1087(1)	71(1)	0.37(1)	25
Cu	SbF_6	0.1080(3)	59(1)	0.26(1)	30
Cu	NbF_6	0.1039(4)	69(3)	0.32(3)	32
Cu	TaF_6	0.1039(2)	78(2)	0.26(3)	32
Ni	SbF_6	0.1068(4)	60(1)	0.38(1)	19
Ni	PF_6	0.1063(5)	66(2)	0.40(1)	8.4

Table 6.2: Muon–fluorine dipole–dipole interaction fitted parameters in the family $[M(HF_2)(pyz)_2]X$, extracted from fitting data to Eq. (6.7). In addition to separation by metal ion, Cu compounds are grouped by the temperature at which the measurement was made: those compounds measured over a range of temperatures appear in both sections of the table.

A muon and nucleus interact via the two-spin Hamiltonian

$$\hat{H} = \sum_{i>j} \frac{\mu_0 \gamma_i \gamma_j \hbar}{4\pi r^3} \left[\boldsymbol{S}_i \cdot \boldsymbol{S}_j - 3 \left(\boldsymbol{S}_i \cdot \hat{\boldsymbol{r}} \right) \left(\boldsymbol{S}_j \cdot \hat{\boldsymbol{r}} \right) \right], \tag{6.4}$$

where the spins $\boldsymbol{S}_{i,j}$ with gyromagnetic ratios $\gamma_{i,j}$ are separated by the vector $\boldsymbol{r}$. This gives rise to a precession of the muon spin, and the muon-spin polarisation along a quantisation axis z varies with time as

$$D_z(t) = \frac{1}{N} \left\langle \sum_{m,n} \left| \langle m \left| \sigma_q \right| n \rangle \right|^2 \mathrm{e}^{\mathrm{i}\omega_{m,n} t} \right\rangle_q, \tag{6.5}$$

where N is the number of spin states, $|m\rangle$ and $|n\rangle$ are eigenstates of the total Hamiltonian $\hat{H}$, σ_q is the Pauli spin matrix corresponding to the direction q, and $\langle\rangle_q$ represents an appropriately-weighted powder average. The vibrational frequency of the muon–fluorine bond exceeds by orders of magnitude both the frequencies observable in a μ^+SR experiment, and the frequency appropriate to the dipolar coupling in Eq. (6.4); the bond length probed via these entangled states is thus time-averaged over thermal fluctuations. Fluorine is an especially strong candidate for this type of interaction firstly because it is highly electronegative causing the positive muon to stop close to fluorine ions, and secondly because its nuclei are 100% ^{19}F, which has $I = \frac{1}{2}$.

Data were fitted to a relaxation function

$$A(t) = A_0 (p_1 \mathrm{e}^{-\lambda_{\text{F-}\mu} t} D_z(t) + p_2 \mathrm{e}^{-\sigma^2 t^2}) + A_{\text{bg}} \mathrm{e}^{-\lambda_{\text{bg}} t}, \tag{6.6}$$

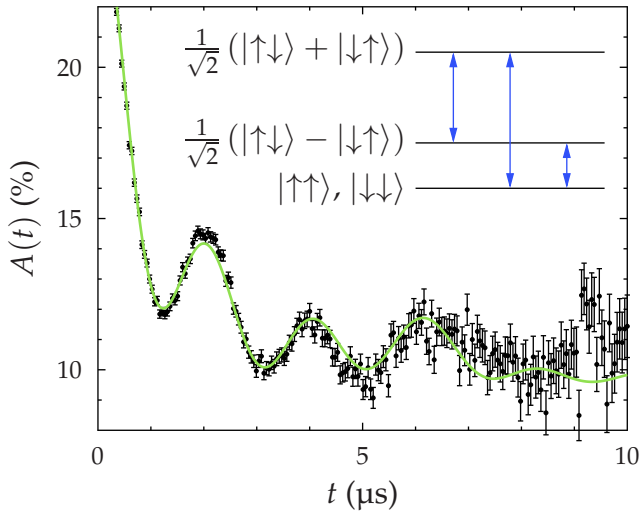

Figure 6.5: Data taken at $T = 15\,\mathrm{K} \gg T_\mathrm{N} = 1.4\,\mathrm{K}$ for $[Cu(HF_2)(pyz)_2]BF_4$, showing Fμ oscillations along with a fit to Eq. (6.6). The inset shows the energy levels present in a simple system of two $S = \frac{1}{2}$ spins, along with the allowed transitions.

where the amplitude fraction $p_1 \approx 70\%$ reflects the muons stopping in a site or set of sites near to a fluorine nucleus, which result in the observed oscillations $D_z(t)$; the weak relaxation of the muon spins is crudely modelled by a decaying exponential. The fraction $p_2 \approx 30\%$ describes those muons stopping in a class of sites primarily influenced by the randomly-orientated fields from other nuclear moments, giving rise to a Gaussian relaxation with $\sigma \approx 0.3\,\mathrm{MHz}$. Example data and a fit are shown in Fig. 6.5, whilst parameters extracted by fitting this function to data from each compound are shown in Table 6.2.

Fits to a variety of different $D_z(t)$ functions were attempted, including that resulting from a simple Fμ bond (previously observed in some polymers [99]) and the better-known FμF complex comprising a muon and two fluorine nuclei in linear symmetric configuration, which is seen in many alkali fluorides [100]. This latter model was also modified to include the possibilities of asymmetric and nonlinear bonds. Previous measurements [98] made in the paramagnetic regime of $[Cu(HF_2)(pyz)_2]ClO_4$ suggested that the muon stopped close to a single fluorine in the HF_2 group and also interacted with the more distant proton. This interaction is dominated by the F–μ coupling and, for our fitting, the observed muon–fluorine dipole–dipole oscillations were found to be well described by a single Fμ interaction damped by a phenomenological relaxation factor. For such Fμ entanglement, the time evolution of the polarisation is described by

$$D_z(t) = \frac{1}{6}\left[1 + \sum_{j=1}^{3} u_j \cos\left(\omega_j t\right)\right], \tag{6.7}$$

where $u_1 = 2$, $u_2 = 1$ and $u_3 = 2$. The frequencies $\omega_j = j\omega_\mathrm{d}/2$, where $\omega_\mathrm{d} = \mu_0\gamma_\mu\gamma_\mathrm{F}\hbar/4\pi r^3$, in which $\gamma_\mathrm{F} = 2\pi \times 2.518 \times 10^8\,\mathrm{MHz\,T^{-1}}$ is the gyromagnetic ratio

material	r_0 (nm)	a (10^{-7} nm K^{-2})
$[Cu(HF_2)(pyz)_2]BF_4$	0.10376(3)	3.96(6)
$[Cu(HF_2)(pyz)_2]ClO_4$	0.10842	2.7212
PVDF [99]	0.10914	1.9488

Table 6.3: Fitted values obtained by fitting muon–fluorine bond lengths with a T^2 scaling law, as Eq. (6.9).

of a ^{19}F nucleus [101], and r is the muon–fluorine separation. These three frequencies arise from the three transitions between the three energy levels present in a system of two entangled $S = \frac{1}{2}$ particles (see inset to Fig. 6.5). The fact that the relaxation function is similar in all materials in the series, including $[Cu(HF_2)(pyz)_2]ClO_4$ which is the only compound studied without fluorine in its anion, (the only difference being a slight lengthening of the μ–F bond, and with no significant change in oscillating fraction) suggests that the muon site giving rise to the Fμ oscillations in all systems is near the HF_2 bridging ligand.

The temperature evolution of the Fμ signal was studied for $T \leq 300$ K in $[Cu(HF_2)(pyz)_2]BF_4$ and $[Cu(HF_2)(pyz)_2]ClO_4$. In both cases, the dipole–dipole oscillations disappear gradually in a temperature range $150 \lesssim T \lesssim 250$ K, with oscillations totally absent in the centre of this range, followed by reappearing as temperature is increased further. Plots of $A(t)$ spectra at a variety of temperatures are shown in Fig. 6.6 (a) and (d). The data were initially fitted to Eq. (6.6), with all parameters left free to vary. The temperature-evolution of the muon–fluorine bond length, $r_{F-\mu}$, can be seen in Fig. 6.6 (b) and (e). The spectra were also fitted with

$$A(t) = A_0 \left(p_1 e^{-\lambda_0 t} + p_2 e^{-\sigma^2 t^2} \right) + A_{bg} e^{-\lambda_{bg} t}, \tag{6.8}$$

a sum of an exponential and a Gaussian relaxation, which might be expected to describe the data in the region where the oscillations vanish. Both this relaxation and that extracted from Eq. (6.6) are plotted in Fig. 6.6 (c) and (f), labelled λ_0 and $\lambda_{F-\mu}$ respectively.

This bond length appears to grow and then shrink by nearly 20% over the 100 K range where the oscillations fade from the spectra and reappear. This variation is significantly larger than any variation in crystal lattice parameters which would be expected. Since the oscillations visibly disappear from the measured spectra, results from fitting with an oscillatory relaxation function are artefacts of the fitting procedure: since the frequencies scale with $1/r^3$, increasing bond length together with the associated relaxation rate fits the data with a suppressed oscillatory signal. This can be approximately quantified by examining the ratio $Q = 2\pi\lambda_{F-\mu}/\omega_d$, where a large value indicates that the function relaxes significantly before a single Fμ oscillation is completed. The shaded regions in Fig. 6.6 show where $Q > 2$, which acts as an approximate bound on where the parametrisation in Eq. (6.6) would be expected to fail. In the low-T region where $Q < 2$, the bond lengths appear to scale roughly as T^2, which has previously been observed in fluoropolymers [99].

Parameters extracted from fitting to

$$r_{\text{F}-\mu} = aT^2 + r_0 \tag{6.9}$$

are shown in Table 6.3.

The observation in these two samples of Fμ oscillations which disappear and then reappear is puzzling. While a definitive mechanism has not been identified, it is probably possible to rule out an electronically mediated effect since, for $T \gg T_N$, the Cu moment fluctuations will be outside the muon time-window. An explanation could involve nearby nuclear moments, possibly influenced by a thermally-driven structural distortion or instability.

A similar study of $[Cu(HF_2)(pyz)_2]SbF_6$ is shown in Fig. 6.6 (g), (h) and (i). In this material, the oscillations appear not to vanish over the temperature range studied, though a brief disappearance at $T \approx 200\,\text{K}$ cannot be ruled out. Instead, the oscillations show an apparently monotonic increase in damping with temperature, and the fitted bond length does not follow Eq. (6.9). The shaded region in Fig. 6.6 (h) and (i) has no upper bound, though we cannot rule out a constraint at $T > 250\,\text{K}$. The pure relaxation λ_0 is omitted because there is no region where the Fμ oscillations are sufficiently damped for Eq. (6.8) to be a good parametrisation.

6.4 Muon site determination

Combining the data measured above and below the transition in these materials allows us to attempt to construct a self-consistent picture of possible muon sites. The observed dipole–dipole observations above T_N suggest that at least one muon stopping site is near a fluorine ion. We consider three classes of probable muon site: Class I sites near the fluorine ions in the HF_2 groups, Class II sites near the pyrazine rings, and Class III sites near the anions at the centre of the pseudocubic pores. Comparison of Tables 6.1 and 6.2 show that the dominant amplitude component for $T > T_N$ arises from dipole–dipole oscillatory component $p_1 e^{-\lambda t} D_z(t)$ and from the fast-relaxing component $p_3 e^{-\lambda_3 t}$ for $T < T_N$, and that these are comparable in amplitude. It is therefore plausible to suggest that these two signals correspond to contributions from the same Class I muon sites near the HF_2 groups. Moreover, the analysis of the $T > T_N$ spectra in the previous section implies that this site lies $r_{\mu-F} \approx 0.11\,\text{nm}$ from an F in the HF_2 groups. The remainder of the signal (the oscillating fraction below T_N and the Gaussian relaxation above) can also be identified, suggesting that the sites uncoupled from fluorine nuclei (Classes II and/or III) result in the magnetic oscillations observed for $T < T_N$.

Further, the evidence from Fμ oscillations makes the occurence of Class III muon sites unlikely. The fact that spectra observed for $T > T_N$ in the $X^- = ClO_4^-$ material are nearly identical to those in all other compounds, in which X contains fluorine, suggest that the muons do not stop near the anions. Moreover, as discussed in Secs. 7.1 and 7.2 below, no Fμ oscillations are observed in $[Cu(pyz)_2(pyo)_2]X_2$ ($Y^- = BF_4^-$, PF_6^-) or $[Cu(pyo)_6](BF_4)_2$, suggesting that muons do not stop preferentially near these fluorine-rich anions either. We can therefore rule out the existence of

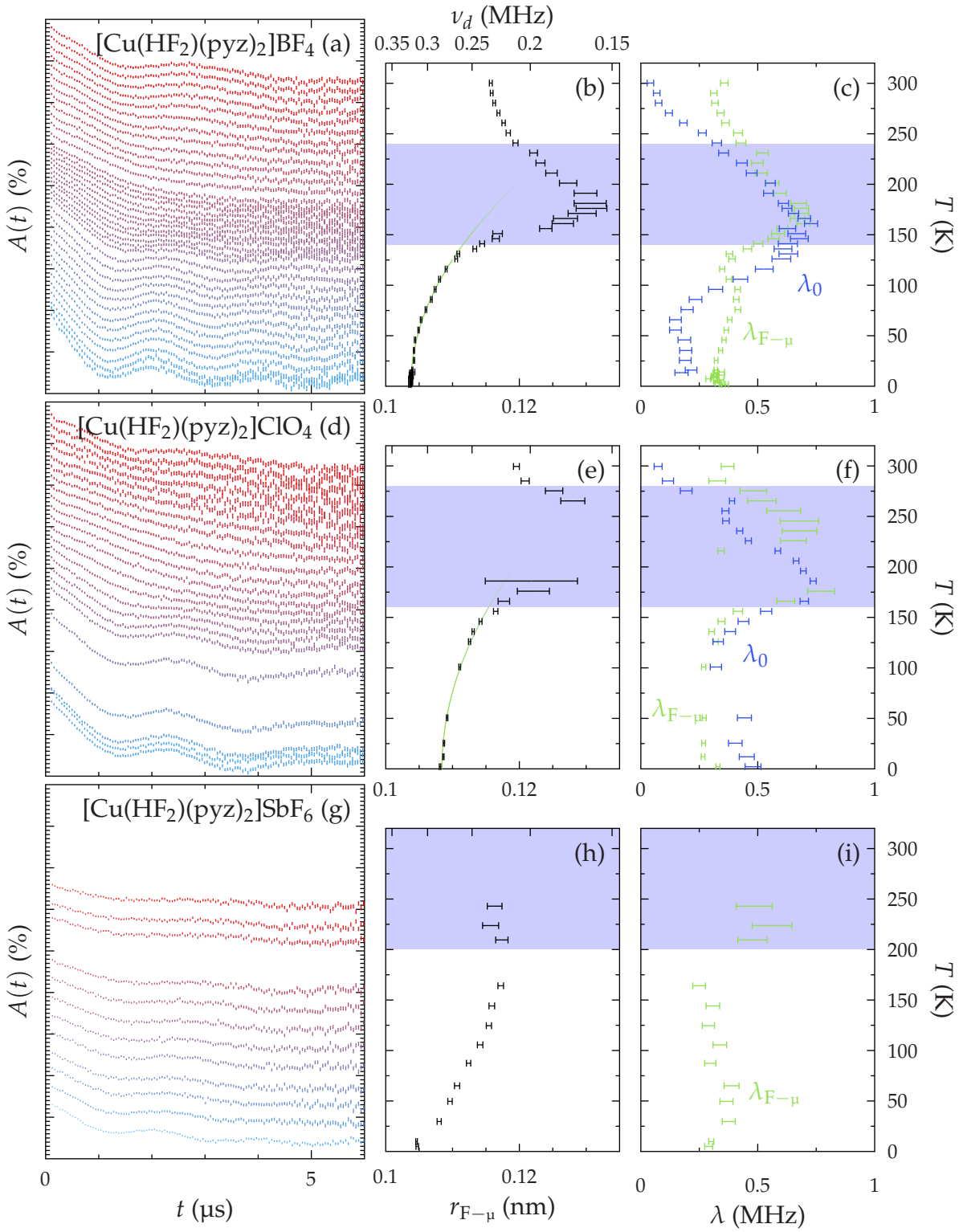

Figure 6.6: (caption on next page)

Figure 6.6: (figure on previous page) (a) Muon–fluorine dipole–dipole oscillations in $[Cu(HF_2)(pyz)_2]BF_4$ over a temperature range $2 \leq T \leq 300$ K. Asymmetry spectra are displaced vertically so as to approximately align with the temperature scale on plots (b) and (c). Ticks on the y-axis of (a) denote 1% asymmetry. Plot (b) shows the fitted value for $r_{F-\mu}$ as a function of temperature. The line shown is a fit to the low-T points with a T^2 scaling law, Eq. (6.9). The upper x-axis shows values of the dipole frequency, ν_d, which correspond to the lower x-axis values of $r_{F-\mu}$. Plot (c) shows fitted relaxation rates $\lambda_{F-\mu}$ and λ_0, referring to the relaxation of the Fμ function $D_z(t)$ in Eq. (6.6), and the pure relaxation in Eq. (6.8). Shaded regions indicate temperatures where $Q = 2\pi\lambda_{F-\mu}/\omega_d > 2$, roughly parametrising the disappearance of the oscillations. (d), (e) and (f) follow (a), (b) and (c), but show data for $[Cu(HF_2)(pyz)_2]ClO_4$. (g), (h) and (i) similarly, but for $[Cu(HF_2)(pyz)_2]SbF_6$ over the range $5 \leq T \leq 250$ K. The 5 K $A(t)$ plot is omitted because the background is raised substantially by approach to the transition to LRO.

Class III muon sites and propose that the magnetic oscillations measured for $T < T_N$ most probably arise due to Class II sites found near the pyrazine ligands.

Below T_N, the measured muon precession frequencies allow us to determine the magnetic field at these Class II muon sites via $\nu = \gamma_\mu B/2\pi$. Simulating the magnetic field inside the crystal therefore allows us to compare these B-fields with those predicted for likely magnetic structures and may permit us to constrain the ordered moment. For the case of our ZF measurements in the antiferromagnetic state, the local magnetic field at the muon site $\boldsymbol{B}_{local}$ is given by

$$\boldsymbol{B}_{local} = \boldsymbol{B}_{dipole} + \boldsymbol{B}_{hyperfine}. \tag{6.10}$$

The spin density giving rise to the contact hyperfine field $\boldsymbol{B}_{hyperfine}$ is particularly difficult to estimate accurately in complex molecular systems, but it is probable for insulating materials such as these that the spin density on the copper ion is well localised and so the hyperfine contribution is ignored in this analysis. The dipole field $\boldsymbol{B}_{dipole}$ can then be considered the sole contribution to local magnetic field, and evaluated as described in Chapter 3.

Although these materials are known to be antiferromagnetic from their negative Curie–Weiss temperatures and zero spontaneous magnetisation at low temperatures [91, 90], their magnetic structures are unknown. Dipole-field simulations were therefore performed for a variety of trial magnetic structures with $\mu = \mu_B$. Results are analysed using the Bayesian scheme outlined in Chapter 3. We begin by allowing the possibility that the magnetic precession signal could arise from any of the possible classes of muon site identified above. Random positions in the unit cell were generated and dipole fields calculated at these. To prevent candidate sites lying too close to atoms we constrain all sites such that $r_{\mu-A} > 0.1$ nm where A is any atom. Possible Class I muon sites were identified with $r_{\mu-F} = r_0 \pm 0.01$ nm (where r_0 is the muon–fluorine distance established from Fμ oscillations) and possible Class II sites were selected with the constraint that $0.10 \leq r_{\mu-C,N} \leq 0.12$ nm. The predicted probability density function (pdf) of muon precession frequencies

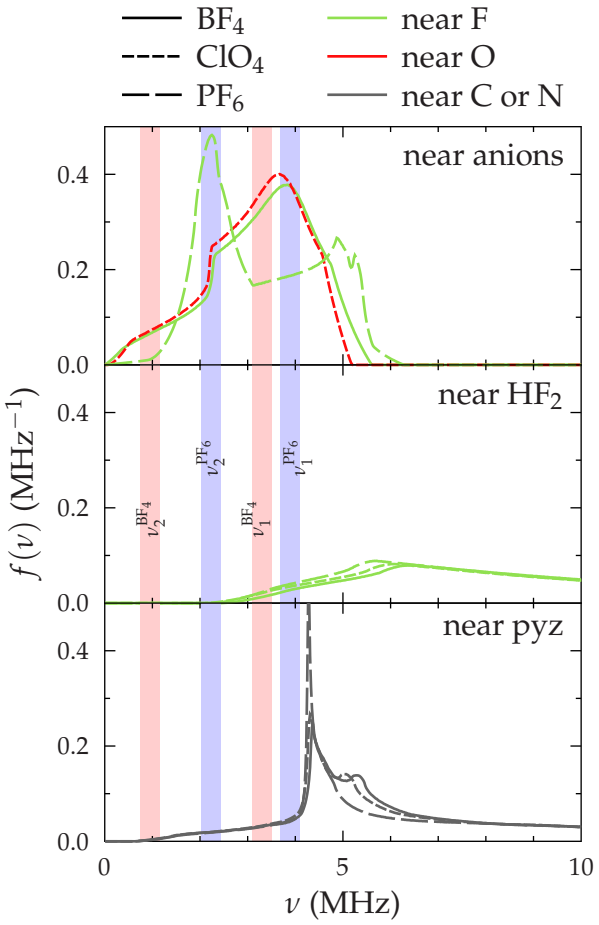

Figure 6.7: Probability density functions of muon precession frequencies at positions close to likely muon stopping sites in $[Cu(HF_2)(pyz)_2]X$ with Cu^{2+} moments $\mu = \mu_B$. The graphs show dipole fields near the fluorine or oxygen atoms in the negative anions; near the fluorine atoms in the bifluoride ligands; and near the carbon and nitrogen atoms, as a proxy for proximity to the pyrazine ring. The type of line indicates the compound for which the calculation was performed. The muon site is constrained to be close to particular atoms, indicated by line color. The shaded areas indicate ranges of fitted frequencies as $T \to 0$; two frequencies $\nu_{1,2}^{BF_4}$ represent those observed where $X^- = BF_4^-$, and $\nu_{1,2}^{PF_6}$ those observed in the $X^- = PF_6^-$ analogue.

(resulting from the magnitudes of the calculated fields) are plotted in Fig. 6.7, with the observed frequencies superimposed. Results are shown for a trial magnetic structure comprising copper spins lying in the plane of the pyrazine layers and at 45° to the directions of the pyrazine chains, and with spins arranged antiferromagnetically both along those chains and along the HF_2 groups. This candidate structure is motivated by analogy with $[Cu(pyz)_2](ClO_4)_2$, which also comprises Cu^{2+} ions in layers of 2D pyrazine lattices [102], and with the parent phases of the cuprate superconductors [89], which are also two-dimensional Heisenberg systems of $S = \frac{1}{2}$ Cu^{2+} ions. Other magnetic structures investigated give qualitatively similar results. From Fig. 6.7 it is clear that the only sites with significant probability density near to the observed frequencies are those lying near the anions (i.e. Class III sites) which do not appear to be compatible with our data. The more plausible muon sites correspond to higher frequencies than those observed. Our conclusion is that it is likely that the Cu^{2+} moments are rather smaller than the μ_B assumed in this initial calculation.

If we accept that the muon sites giving rise to magnetic precession are near the pyrazine groups then we may use this calculation to constrain the size of the copper moment. Since ν is obtained from experiment, what we would like to know is $g(\mu|\nu)$, the pdf of copper moment μ given the observed ν. This can be obtained from our calculated $f(\nu/\mu)$ using Bayes' theorem, which yields

$$g(\mu|\nu) = \frac{\frac{1}{\mu} f(\nu/\mu)}{\int_0^{\mu_{\max}} \frac{1}{\mu'} f(\nu/\mu')\,\mathrm{d}\mu'}\,, \tag{6.11}$$

where a prior probability is assumed for the copper moment that is uniform between zero and $\mu_{\max}$. We take $\mu_{\max} = 2\mu_B$, although the results are insensitive to the precise value of $\mu_{\max}$ as long as it is reasonably large. When multiple frequencies $\{\nu_i\}$ are present in the spectra, it is necessary to multiply their probabilities of observation in order to obtain the chance of their simultaneous observation, so we evaluate

$$g(\mu|\{\nu_i\}) \propto \prod_i \int_{\nu_i-\Delta\nu_i}^{\nu_i+\Delta\nu_i} f(\nu_i/\mu)\,\mathrm{d}\nu_i\,, \tag{6.12}$$

where $\Delta\nu_i$ is the error on the fitted frequency. Results are shown in Fig. 6.8, along with the dipole-field pdfs which gave rise to them. By inspection of the pdfs, the copper moment is likely to be $\mu \lesssim 0.5\mu_B$. The dipole-field simulations results also lend weight to our contention that the oscillatory signal cannot arise from the sites that also lead to the Fμ component above T_N. If this were the case then the most likely moment on the copper would be $\mu_{Cu} \lesssim 0.2\mu_B$, which seems unreasonably small. Moment sizes of $\mu \lesssim 0.5\mu_B$ were also observed for the 2DSLQHA system La_2CuO_4 (a recent estimate [103] from neutron diffraction gave $[0.42 \pm 0.01]\mu_B$), despite the predictions of $0.6\mu_B$ from spin wave theory and Quantum Monte Carlo [104]. It was suggested in that case [104] that disorder might play a role in reducing the moment sizes; an additional possible mechanism for this suppression is ring exchange [105, 106].

One limitation of this analysis is that the mechanism for magnetic coupling of copper ions through the pyrazine rings is postulated to be via spin exchange, in

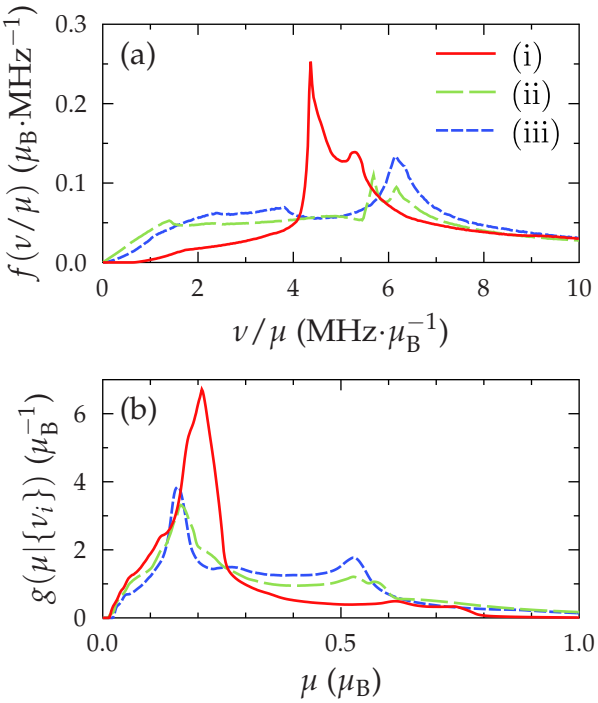

Figure 6.8: Probability density functions for muons in the putative oscillating sites near the pyrazine rings in $[Cu(HF_2)(pyz)_2]BF_4$ (a) for muon precession frequency ν assuming that the moment on the copper site $\mu = \mu_B$, created fom a histogram of dipole fields evaluated at points satisfying the constraints detailed in the text; and (b) for the moment on the copper sites given the frequencies actually observed, evaluated using the pdfs in (a) and Eq. (6.12). Lines represent trial magnetic structures. All exhibit antiferromagnetic coupling through both the bifluoride and pyrazine exchange paths, whilst (i) has copper moments pointing at 45° to the pyrazine grid, (ii) has moments along one of the pyrazine grid directions (***a*** or ***b***), and (iii) has copper moments pointing along the bifluoride axis (***c***).

which small magnetic polarisations are induced on intervening atoms [107]. Density functional theory calculations estimate that these are small, with the nitrogen and carbon moments estimated at $\mu_C \approx 0.01\mu_B$ and $\mu_N \approx 0.07\mu_B$, respectively [108]. However, their effect may be non-negligible: they may be significantly closer to the muon site than a copper moment, and dipole fields fall off rapidly, as $1/r^3$. Further, since much of the electron density in a pyrazine ring is delocalised in π-orbitals, the moments may not be point-like, as assumed in our dipole-field calculations. This may also lead to overlap of spin density at the muon site and result in a nonzero hyperfine field.

Chapter 7

Other quasi–two-dimensional molecular magnets

In addition to the $[Cu(HF_2)(pyz)_2]X$ systems examined in the previous chapter, a wide range of related molecular materials can be fabricated which display quasi–two-dimensional magnetic interactions. This type of investigation of a variety of related materials allows a systematic evaluation not only of the molecular magnetism itself, but also the use of muon techniques to study it. In particular, the range of differing dimensionalities present in molecular systems and how this relates to the critical exponent β, often derived from μ^+SR data, is examined.

This chapter reports the results of μ^+SR measurements on other quasi-2D systems. First, $[Cu(pyz)_2(pyo)_2]Y_2$, with Y^- = BF_4^- or PF_6^-, in which pyo ligands bridge $Cu(pyz)_2$ planes. Then, the quasi-2D non-polymeric compounds $[Cu(pyo)_6]Z_2$, where Z^-=BF_4^-, ClO_3^- or PF_6^- are examined. I also investigate materials in which either Ni^{2+} ($S = 1$) or Ag^{2+} ($S = \frac{1}{2}$) form the magnetic species in the quasi-2D planes rather than Cu^{2+}.

7.1 $[Cu(pyz)_2(pyo)_2]Y_2$

In this section, I report the magnetic behaviour of another family of molecular systems which shows quasi-2D magnetism, but for which the interlayer groups are very different and arranged in a completely different structure, resulting in a 2D coordination polymer. This system is $[Cu(pyz)_2(pyo)_2]Y_2$, where Y^- = BF_4^-, PF_6^-. As with the previous case, $S = \frac{1}{2}$ Cu^{2+} ions are bound in a 2D square lattice of $[Cu(pyz)_2]^{2+}$ sheets lying in the ***ab***-plane. Pyridine-*N*-oxide (pyo) ligands [shown in Fig. 5.1 (b)] protrude from the copper ions along the *c*-direction, perpendicular to the ***ab***-plane in the Y^- = PF_6^- material, but making an angle $\beta - 90 \approx 29^\circ$ with the normal in Y^- = BF_4^-. The anions then fill the pores remaining in the structure. The structure of $[Cu(pyz)_2(pyo)_2](BF_4)_2$ is shown in Fig. 7.1.

In a typical synthesis[1], an aqueous solution of CuY_2 hydrate (Y^- = BF_4^- or PF_6^-)

[1]Samples studied in this chapter were synthesised by J. L. Manson.

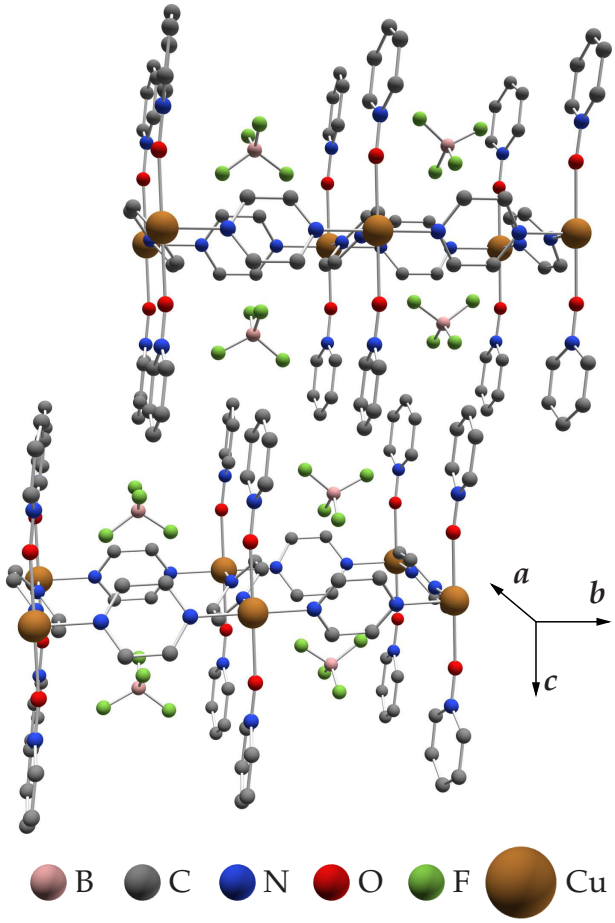

Figure 7.1: Structure of $[Cu(pyz)_2(pyo)_2](BF_4)_2$. Copper ions lie in 2D square layers, bound by pyrazine rings. Pyridine-*N*-oxide ligands protrude from the coppers in a direction approximately perpendicular to these layers. Tetrafluoroboride ions fill the pores remaining in the structure. Ion sizes are schematic; copper ions are shown twice as large for emphasis, and hydrogens have been omitted for clarity.

was combined with an ethanol solution that contained a mixture of pyrazine and pyridine-*N*-oxide or 4-phenylpyridine-*N*-oxide. Deep blue-green solutions were obtained in each case, and when allowed to slowly evaporate at room temperature for a few weeks, dark green plates were recovered in high yield. Crystal quality could be improved by sequential dilution and collection of multiple batches of crystals from the original mother liquor. The relative amounts of pyz and pyo were optimised in order to prevent formation of compounds such as $CuY_2(pyz)_2$ or $[Cu(pyo)_6]Y_2$.

Samples were measured in the LTF apparatus at SμS. Example data measured on $[Cu(pyz)_2(pyo)_2]Y_2$ are shown in Fig. 7.2, where oscillations are observed in $A(t)$ at a single frequency below T_N. Data were fitted to a relaxation function

$$A(t) = A_0 \left(p_1 \cos(2\pi\nu_1 t) e^{-\lambda_1 t} + p_2 e^{-\lambda_2 t} + p_3 e^{-\lambda_3 t} \right) + A_{bg}. \tag{7.1}$$

The small amplitude fraction $p_1 < 10\%$ for both samples refers to muons stopping

material	ν_1 (MHz)	p_1	p_2	p_3	T_N (K)	β	α	J/k_B (K)	$\lvert J_\perp/J\rvert$
$[Cu(pyz)_2(pyo)_2](BF_4)_2$	1.4(1)	< 10	50	50	1.5(1)	0.25(10)	1.6(3)	-	-
$[Cu(pyz)_2(pyo)_2](PF_6)_2$	0.64(1)	< 10	50	50	1.91(1)	0.22(2)	1.1(3)	4.5(5) *	0.05(3)
$[Cu(pyo)_6](BF_4)_2$	0.599(5)	15	30	55	0.649(5)	0.29(1)	1.7(1)	1.09(2) †	0.23(2)
$Ag(pyz)_2(S_2O_8)$	2.45(4)	30	70	-	7.8(3)	0.19(2)	3(2)	52.7(3)	$\sim 10^{-6}$

Table 7.1: Fitted parameters for molecular magnets in the family $[Cu(pyz)_2(pyo)_2]Y_2$, $[Cu(pyo)_6](BF_4)_2$ and $Ag(pyz)_2(S_2O_8)$. The first parameters shown relate to fits to Eq. (7.1) (for the first three rows) or Eq. (7.4) [for $Ag(pyz)_2(S_2O_8)$]. This allows us to derive frequencies at $T = 0$, ν_i; and probabilities of stopping in the various classes of stopping site, p_i, in percent. Then, the temperature dependence of ν_i is fitted with Eq. (4.3), extracting values for the Néel temperature, T_N, critical exponent β and parameter α. Finally, the quoted J/k_B is obtained from pulsed-field experiments [80] (* The value of g in this compound varies strongly with angle, between $g_{ab} = 2.028$ and $g_c = 2.255$. The value of g was thus approximated as $(\frac{2}{3}g_{ab} + \frac{1}{3}g_c) \pm (g_c - g_{ab})$. † The value of J is extracted from heat capacity and susceptibility from Ref. 109.). The ratio of inter- to in-plane coupling, $J_\perp/J$, is obtained by combining T_N and J with formulae extracted from quantum Monte Carlo simulations (see Sec. 5.3, and Ref. 80). The dash in the p_3 column for $Ag(pyz)_2(S_2O_8)$ reflects the fact that there is no third component in Eq. (7.4). Dashes in the J/k_B and $J_\perp/J$ columns for $[Cu(pyz)_2(pyo)_2](BF_4)_2$ indicate a lack of pulsed-field data for this material.

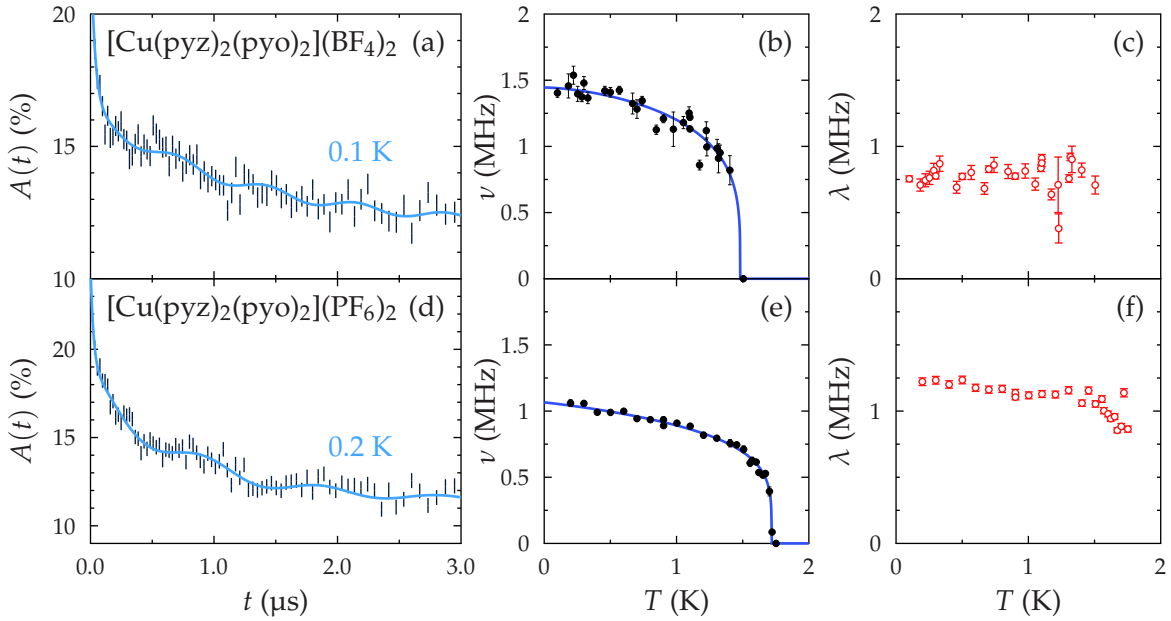

Figure 7.2: Example data and fits for $[Cu(pyz)_2(pyo)_2]Y_2$. From left to right: (a) and (d) show sample asymmetry spectra $A(t)$ for $T < T_N$ along with a fit to Eq. (7.1); (b) and (e) show the frequency ν as a function of temperature; and (c) and (f) show relaxation rates λ_i as a function of temperature. The relaxation rates λ_1, associated with the oscillation, and λ_3, the fast-relaxing initial component, do not vary significantly with T and are not shown. Only a slight trend in λ_2 in the $Y^- = PF_6^-$ material [graph (f)] is observed.

in a site or set of sites with a narrow distribution of quasi-static local magnetic fields, giving rise to the oscillations; $p_2 \approx 50\%$ is the fraction of muons stopping in a class of sites giving rise to a large relaxation rate $30 \lesssim \lambda \lesssim 60$ MHz and $p_3 \approx 50\%$ represents the fraction of muons stopping in sites with a small relaxation rate $\lambda_3 \approx 1$ MHz. The data from these compounds fit best with $\phi = 0$, and it is thus omitted from this expression. Frequencies obtained from fitting the data to Eq. (7.1) were then modelled with Eq. (4.3). The results of these fits are shown in Fig. 7.2, and Table 7.1.

Our results show that $[Cu(pyz)_2(pyo)_2](BF_4)_2$ has a transition temperature $T_N = 1.5 \pm 0.1$ K and a quasi-static magnetic field at the muon site $\nu_1(T = 0) = 1.4 \pm 0.1$ MHz. No quantities other than ν_1 show a significant trend in the temperature region $0.1 \leq T \leq 1.6$ K. Above the transition, purely relaxing spectra are observed, displaying no Fμ oscillations. As suggested above, this makes the existence of muon sites near the anions unlikely. A critical exponent of $\beta = 0.25 \pm 0.10$ is found, where the large uncertainty results in part from the difficulty in fitting the $A(t)$ data in the critical region.

Our results for $[Cu(pyz)_2(pyo)_2](PF_6)_2$ show that the transition temperature is slightly higher at $T_N = 1.72 \pm 0.02$ K and the oscillations occur at a lower frequency of $\nu_1(T = 0) = 1.07 \pm 0.03$ MHz. The relaxation rates λ_2 and λ_3 also decrease in magnitude as temperature is increased, settling on roughly constant

values $\lambda_2 \approx 0.6$ MHz and $\lambda_3 \approx 15$ MHz for $T > T_N$. No other quantities show a significant trend in the temperature region $0.2 \leq T \leq 1.7$ K. Above the transition, relaxing spectra devoid of Fμ oscillations are again observed. The critical exponent $\beta = 0.22 \pm 0.02$.

The small amplitude of the oscillations, common to both samples, might be explained in a number of ways. The materials may undergo long-range ordering but there may be an increased likelihood of stopping in sites where the magnetic field nearly precisely cancels. Alternatively, a range of similar muon sites may be present with a large distribution of frequencies, or alternatively the presence of dynamics, washing out any clear oscillations in large fractions of the spectra and instead resulting in a relaxation. Finally, it is not possible to exclude the possibility that only a small volume of the sample undergoes a magnetic transition; this may indicate the presence of a small impurity phase, possibly located at either grain boundaries or, given that this is a powder sample, near the crystallites' surfaces. The behaviour of fitted parameters in these materials is qualitatively similar to that reported in $CuCl_2(pyz)$, where there is also a relatively small precessing fraction of muons and little variation in relaxation rates as T_N is approached from below [95].

7.2 $[Cu(pyo)_6]Z_2$

The next example is not a coordination polymer, but instead forms a three-dimensional structure of packed molecular groups. The molecular magnet $[Cu(pyo)_6]Z_2$, where Z^- = BF_4^-, ClO_3^-, PF_6^-, comprises Cu^{2+} ions on a slightly distorted cubic lattice, located in $[Cu(pyo)_6]^{2+}$ complexes, and surrounded by octahedra of oxygen atoms [109]. The structure is shown in Fig. 7.3. This approximately cubic structure, which arises from the molecules' packing, might suggest that a three-dimensional model of magnetism would be appropriate. In fact, although the observed bulk properties of $[M(pyo)_6]X_2$ where M^{2+} = Co^{2+}, Ni^{2+} or Fe^{2+} are largely isotropic, the copper analogues display quasi–low-dimensional, $S = \frac{1}{2}$ Heisenberg antiferromagnetism [109]. Weakening of superexchange in certain directions, and thus the lowering of the systems' effective dimensionality, is attributed to lengthening of the superexchange pathways resulting from Jahn–Teller distortion of the Cu–O octahedra, which is observed in structural and EPR measurements [111, 110]. At high temperatures, ($T \gtrsim 100$ K), these distortions are expected to be dynamic but, as T is reduced (to ≈ 50 K), they freeze out. The anion Z^- determines the nature of the static Jahn–Teller elongation. The Z^- = BF_4^- material displays ferrodistortive ordering which, in combination with the antiferromagnetic exchange, gives rise to 2D Heisenberg antiferromagnetic behaviour [109, 112]. By contrast, Z^- = ClO_4^-, NO_3^- (neither of which is investigated here) display antiferrodistortive ordering [111], which gives rise to quasi-1D Heisenberg antiferromagnetism [109]. All of the samples investigated were measured in the LTF spectrometer at SμS.

In the Z^- = BF_4^- compound, below a temperature T_N, a single oscillating frequency is observed, indicating a transition to a state of long-range magnetic order. Example data above and below the transition, along with fits, are shown in Fig. 7.4 (a). Data were fitted to Eq. (7.1), and the frequencies extracted from the

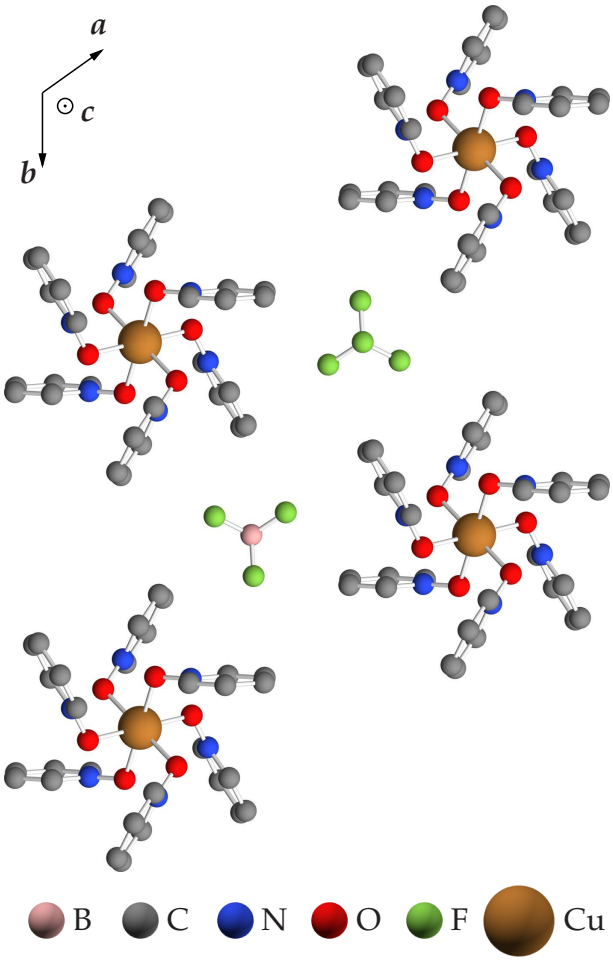

Figure 7.3: Structure of $[Cu(pyo)_6](BF_4)_2$, viewed along the three-fold (***c***-) axis, after Ref. 110. Copper ions are surrounded by octahedra of six oxygens, each part of a pyridine-*N*-oxide ligand; $[Cu(pyo)_6]^{2+}$ complexes space-pack with BF_4^- stabilising the structure. Ion sizes are schematic; copper ions are shown twice as large for emphasis, and hydrogens have been omitted for clarity. As indicated in the top left, the ***a*** and ***b*** directions lie in the plane of the paper, separated by $\gamma = 120°$, whilst the ***c*** direction is out of the page.

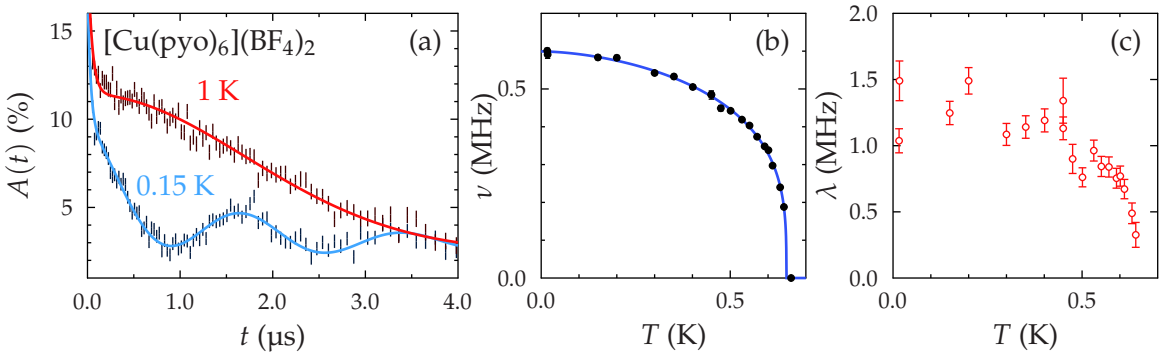

Figure 7.4: Example data and fits for $[Cu(pyo)_6](BF_4)_2$. From left to right: (a) shows sample asymmetry spectra $A(t)$ for $T < T_N$ and $T > T_N$, along with fits to Eq. (7.1) and Eq. (7.2), respectively; (b) shows frequency as a function of temperature; and (c) shows relaxation rate λ_2 as a function of temperature; λ_1 was held fixed during the fitting procedure, and λ_3 persists for $T > T_N$. In the $\nu(T)$ plot, error bars are included on the points but in most cases they are smaller than the marker being used.

procedure fitted as a function of temperature to Eq. (4.3), as shown in Fig. 7.4 (b). This procedure identifies a transition temperature $T_N = 0.649 \pm 0.005$ K. The only other parameter found to vary significantly in the range $20\,\text{mK} \leq T \leq T_N$ was λ_2, shown in Fig. 7.4 (c). The fitted parameters are shown in Table 7.1. We may compare this with the result of an earlier low-temperature specific heat study [109] which found a very small λ-point anomaly at $T_N = 0.62(1)$ K, slightly lower than our result. Fitting the magnetic component of the heat capacity with the predictions from a two-dimensional Heisenberg antiferromagnet gives $J/k_B = -1.10(2)$ K, and similar analysis of the magnetic susceptibility [109] yields $J/k_B = 1.08(3)$ K. Using these values, together with the muon estimate of T_N and Eq. (5.3), allows us to estimate the inter-plane coupling, $J_\perp/J = 0.26(1)$. (Using the value of T_N from heat capacity results in an estimate $J_\perp/J = 0.21(2)$.)

For temperatures $T_N < T \leq 1$ K, the spectra are well described by a relaxation function

$$A(t) = A_0(p_1 e^{-\lambda t} + p_2 e^{-\sigma^2 t^2}) + A_{bg}, \tag{7.2}$$

comprising an initial fast-relaxing component with $\lambda \approx 20$ MHz, and a Gaussian relaxation with $\sigma \approx 0.4$ MHz corresponding to the slow depolarisation of muon spins due to randomly-orientated nuclear moments.

The $Z^- = ClO_3^-$ material also shows evidence for a magnetic transition, although in this case oscillations in the muon asymmetry are not observed. Instead a discontinuous change in the relaxation which seems to point towards an ordering transition is seen. Example asymmetry spectra are shown in Fig. 7.5 (a) and data at all measured temperatures are well described with the relaxation function

$$A(t) = A_0 e^{-\lambda t} + A_{bg}\,. \tag{7.3}$$

Evidence for a magnetic transition comes from the temperature evolution of λ [Fig. 7.5(b)], where the relaxation decreases with increasing temperature until it

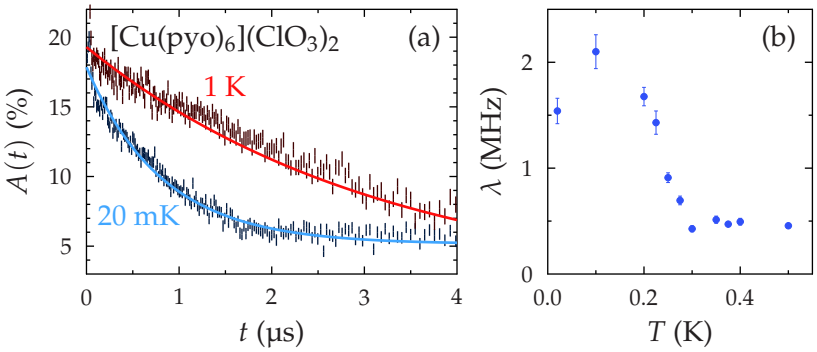

Figure 7.5: Example data and fits for $[Cu(pyo)_6](ClO_3)_2$. Representative $A(t)$ spectra for $T < T_N$ and $T > T_N$, along with fits to Eq. (7.3), are shown in (a), whilst the value of the relaxation rate, λ, as a function of temperature is shown in (b).

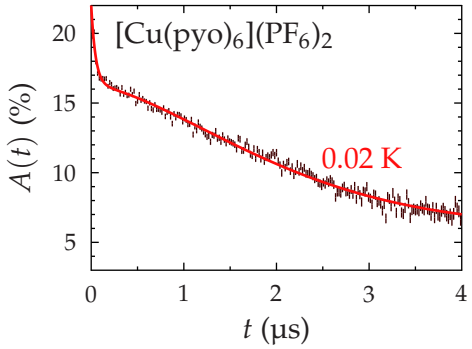

Figure 7.6: Sample asymmetry spectrum for $[Cu(pyo)_6](PF_6)_2$ measured at $T = 0.02$ K. The spectra remain indistinguishable from this across the range of temperatures examined, $0.02\,\text{K} \leq T \leq 1\,\text{K}$.

settles at $T \approx 0.3$ K, on a value $\lambda \approx 0.5$ MHz. It is likely that this tracks the internal magnetic field inside the material, and is suggestive of $T_N = 0.30(1)$ K.

The final member of this family studied, $Z^- = PF_6^-$, shows no evidence for a magnetic transition over the range of temperatures studied, $0.02\,\text{K} \leq T \leq 1\,\text{K}$. An example spectrum is shown in Fig. 7.6. The data resemble the above-transition data measured in the BF_4 and ClO_3 compounds and it therefore seems likely that the paramagnetic state persists to the lowest temperature measured.

7.3 $Ag(pyz)_2(S_2O_8)$

The examples so far have used Cu^{2+} ($3d^9$) as the magnetic species. An alternative strategy is to employ Ag^{2+} ($4d^9$) which also carries an $S = \frac{1}{2}$ moment. This idea has led to the synthesis of $Ag(pyz)_2(S_2O_8)$, which comprises square sheets of $[Ag(pyz)_2]^{2+}$ units spaced with $S_2O_8^{2-}$ anions [113]. Each silver ion lies at the centre of an elongated (AgN_4O_2) octahedron, where the Ag–N bonds are significantly shorter than the Ag–O. Preparation details can be found in Ref. 114.

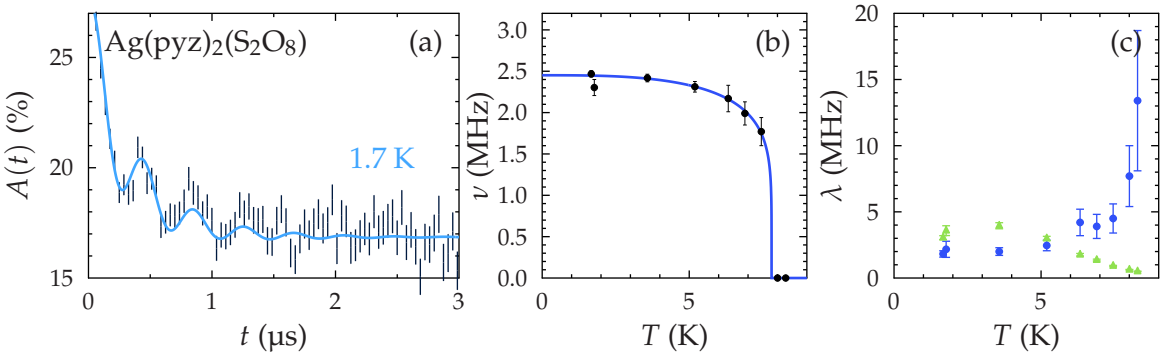

Figure 7.7: Example data and fits for $Ag(pyz)_2(S_2O_8)$. From left to right: (a) shows sample asymmetry spectra $A(t)$ for $T < T_N$ along with a fit to Eq. (7.4); (b) shows the frequency as a function of temperature; and (c) shows relaxation rates λ_i as a function of temperature. Filled circles show the relaxation rate λ_1, which relaxes the oscillation. The filled triangles correspond to the relaxation λ_2.

Measurements were made using the GPS instrument at SμS. Example muon data, along with fits to various parameters, are shown in Fig. 7.7. Asymmetry oscillations are visible in spectra taken below a transition temperature T_N. The data were fitted with a relaxation function

$$A(t) = A_0 \left(p_1 \cos(2\pi\nu_1 t + \phi_1) e^{-\lambda_1 t} + p_2 e^{-\lambda_2 t} \right) + A_{bg}, \tag{7.4}$$

comprising a single damped oscillatory component, a slow-relaxing component, and a static background signal. The onset of increased relaxation λ_1 as the transition is approached from below leads to large statistical errors on fitted values, as is evident in Fig. 7.7 (c). The relaxation λ_2 decreases with increasing temperature. Fitting to Eq. (4.3) allows the critical parameters $\beta = 0.19 \pm 0.02$ and $T_N = 7.8(3)$ K to be determined. Fitted values are shown in Table 7.1.

The in-plane exchange J is too large to be determined with pulsed fields [113]: $M(B)$ does not saturate in fields up to 64 T. However, fitting $\chi(T)$ data allows an estimate of the exchange $J/k_B \approx 53$ K (and thus, in conjunction with g measured by EPR, the saturation field B_c is estimated to be 160 T). Thus, $k_B T_N / J = 0.148 \pm 0.006$. Estimation of the exhange anisotropy with Eq. (5.3) yields $|J_\perp / J| \sim 10^{-6}$, but this very small ratio of ordering temperature to exchange strength is outside the range in which the equation is known to yield accurate results. The alternative method of parametrising the low dimensionality in terms of correlation length at the Néel temperature (see Sec. 5.3) yields $\xi(T_N)/a = 1000 \pm 300$.

7.4 $[Ni(HF_2)(pyz)_2]X$

In order to investigate the influence of a different spin state on the magnetic cation in the $[M(HF_2)(pyz)_2]X$ architecture the $[Ni(HF_2)(pyz)_2]X$ ($X^- = PF_6^-$, SbF_6^-) system has been synthesised [92]. These materials are isostructural with the copper family discussed in Chapter 6, but contain $S = 1$ Ni^{2+} cations.

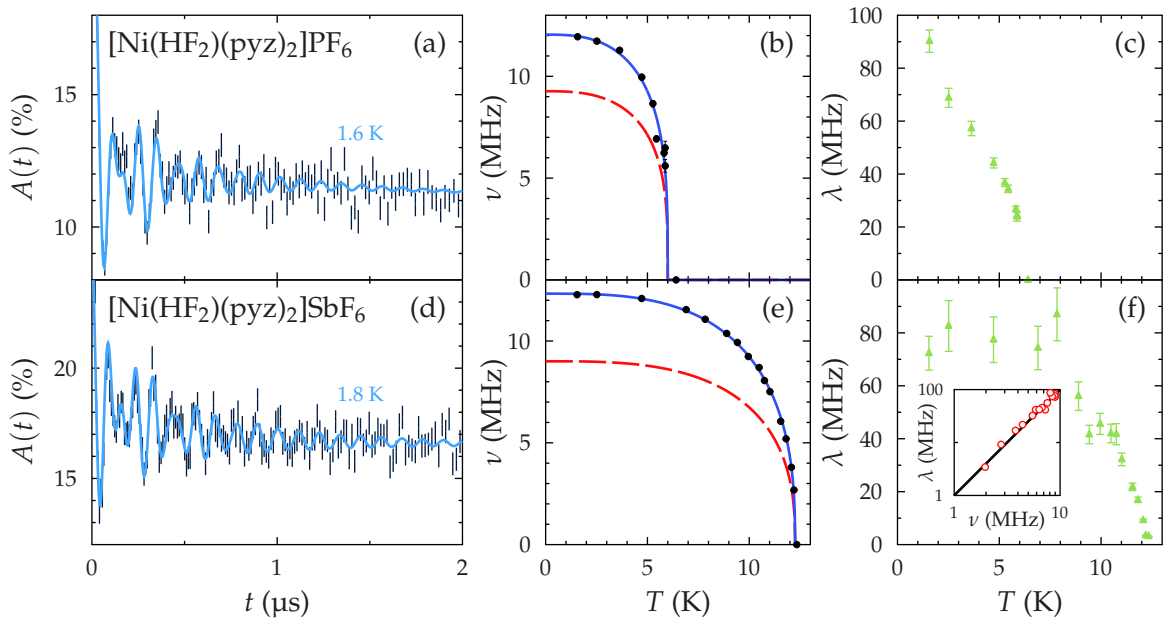

Figure 7.8: Example data and fits for M = Ni magnets. From left to right: (a) and (d) show sample asymmetry spectra $A(t)$ for $T < T_N$ along with a fit to Eq. (6.1); (b) and (e) show frequencies as a function of temperature [no data points are shown for the second line because this frequency ν_2 was held in fixed proportion to the first, ν_1 (see text)]; and (c) and (f) show relaxation rate λ_3 as a function of temperature. In the $\nu(T)$ plot, error bars are included on the points but in most cases they are smaller than the marker being used. The inset to (f) shows $\nu_2 \equiv \nu$ plotted against $\lambda_3 \equiv \lambda$ on a log–log scale. The black line shows $\lambda = \nu^2$.

X	T_N (K)	ν_1	ν_2	λ_3	p_1	p_2	p_3	β	α
PF_6	6.0(4)	12.0	9.3	90	15	10	75	0.25(10)	2.8(2)
SbF_6	12.26(1)	12.3(1)	8.98(1)	80	25	10	65	0.34(4)	3.1(1)

Table 7.2: Fitted parameters for M = Ni magnets. Values of ν_1, ν_2 and λ_3 are given in MHz. Errors shown are statistical uncertainties on fitting and thus represent lower bounds. Errors on Ni...PF_6 could not be estimated due to the fitting procedure (see text).

Data were taken using the GPS spectrometer at PSI. Example data are shown in Fig. 7.8. Oscillations are observed at two frequencies below the materials' respective ordering temperatures. Data were fitted with a relaxation function

$$\begin{aligned} A(t) &= A_0 \left[p_1 e^{-\lambda_1 t} \cos(2\pi\nu_1 t) + p_2 e^{-\lambda_2 t} \cos(2\pi P_2 \nu_1 t) \right. \\ &\quad \left. + p_3 e^{-\lambda_3 t} \right] + A_{bg} e^{-\lambda_{bg} t}. \end{aligned} \tag{7.5}$$

Of those muons which stop in the sample, $p_1 \approx 25\%$ indicates the fraction of the signal corresponding to the high-frequency oscillating state with $\nu_1(T = 0) \approx 12.3\,\text{MHz}$; $p_2 \approx 10\%$ corresponds to muons stopping in the low-frequency oscillating state with $\nu_2(T = 0) \approx 9.0\,\text{MHz}$; and $p_3 \approx 65\%$ represents muons stopping in a site with a large relaxation rate $\lambda_3(T = 0) \approx 70\,\text{MHz}$. The frequencies were observed to scale with one-another, and consequently the second frequency was held in fixed proportion $\nu_2 = P_2\nu_1$ during the fitting procedure. The only other parameter which changes significantly in value below T_N is λ_3, which decreases with a trend qualitatively similar to that of the frequencies. Fitting the extracted frequencies to Eq. (4.3) allows the transition temperature $T_N = 12.25 \pm 0.03\,\text{K}$ and critical exponent $\beta = 0.34 \pm 0.04$ to be extracted. In contrast to the copper family studied in Chapter 6, the relation $\lambda \propto \nu^2$ holds true, suggesting that a field distribution whose width diminishes with increasing temperature is responsible for the variation in λ, and that dynamics are relatively unimportant in determining the muon response. This is shown graphically in the inset to Fig. 7.8 (f), where a plot of frequency against relaxation rate lies on top of a line representing a $\lambda = \nu^2$ relationship. The phase ϕ required in previous fits (e.g. Eq. (6.1)) is not necessesary in fitting these spectra, and is set to zero. Fitted parameters are shown in Table 7.2.

Data for the $X^- = PF_6^-$ compound was subject to similar analysis, fitting spectra below T_N to Eq. (7.5), this time with $p_1 \approx 15\%$, $\nu_1(T = 0) \approx 12.0\,\text{MHz}$; $p_2 \approx 10\%$, $\nu_2(T = 0) \approx 9.3\,\text{MHz}$; and $p_3 \approx 75\%$, $\lambda_3(T = 0) \approx 100\,\text{MHz}$. The phase ϕ again proved unnecessary. These spectra do not show as sharp a transition as the $X^- = SbF_6^-$ compound, with the oscillating fraction of the signal decaying before the appearance of spectra whose different character indicates clearly that the sample is above T_N. The available data do not allow reliable extraction of critical parameters, but it is possible to estimate $5.5\,\text{K} \leq T_N \leq 6.2\,\text{K}$ and $0.15 \leq \beta \leq 0.4$. Fitted values are shown in Table 7.2.

Another method to locate the transition is to observe the amplitude of the muon spectra at late times as a function of temperature. The transition is then from zero in the unordered state to the '$\frac{1}{3}$-tail' characteristic of LRO, described in Sec. 2.4.1. Spectra were fitted with the simple relaxation function $A(t > 5\,\mu\text{s}) = A_{bg} e^{-\lambda_{bg} t}$, and then the amplitudes obtained were fitted with a Fermi-like step function

$$A(t > 5\,\mu\text{s},\ T) = A_2 + \frac{A_1 - A_2}{e^{(T - T_{mid})/w} + 1}, \tag{7.6}$$

which provides a method of modelling a smooth transition between $A_1 = A(T < T_N)$ and $A_2 = A(T > T_N)$. The fitted amplitudes and Fermi function are shown in Fig. 7.9. The fitted mid-point $T_{mid} = 6.4 \pm 0.1\,\text{K}$, and width $w = 0.3 \pm 0.1\,\text{K}$.

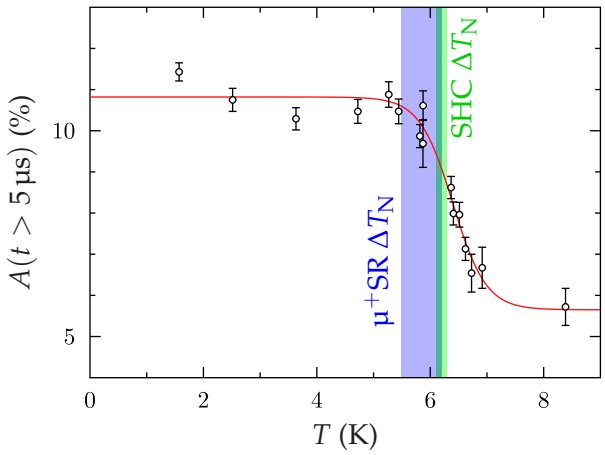

Figure 7.9: The asymmetry at late times $A(t > 5\ \mu s)$ measured in $Ni(HF_2)(pyz)_2PF_6$ along with a fit to Eq. (7.6). Overlaid are regions corresponding to the range of values found by fitting the frequency of oscillations as a function of temperature with Eq. (4.3) ($5.5\ K \leq T_N \leq 6.2\ K$), and the value of the λ-like anomaly in specific heat capacity (SHC) measurements with a representative error of 0.1 K ($6.1\ K \leq T_N \leq 6.3\ K$). The darker area represents the overlap between these regions.

Spin relaxation peaks just above T_N, and so one would expect that T_N lies at the lower end of this transition. Thus, the μ^+SR analysis suggests $T_N = 6.1 \pm 0.3$ K (i.e. $T_{mid} - w \pm w$). This is consistent with the estimate from $\nu_i(T)$ and the value $T_N = 6.2$ K obtained from heat capacity [92].

Members of the M = Ni family exhibit Fμ oscillations rather like their copper counterparts, with a similar fraction of the muons in sites giving rise to dipole–dipole interactions. The results of these fits are shown along with those from Cu compounds in Table 6.2. Because the nickel data were measured at temperatures different from those of the copper compounds and, as described in Sec. 6.3, the muon–fluorine bond length in the compound is sensitive to changes in temperature, care must be taken when comparing these values to those of the Cu family. Linearly interpolating the bond lengths for $[Cu(HF_2)(pyz)_2]SbF_6$ at 9 K and 29 K to find an approximate value of the bond length at 19 K yields $r_{\mu\text{–}F}(T = 19\ K) = 0.1062 \pm 0.0002$ nm (where the error represents a combination of the statistical errors on the fits and variation recorded in thermometry, and is thus a lower bound), very similar to that measured for $[Ni(HF_2)(pyz)_2]SbF_6$, $r_{\mu\text{–}F}(T = 19\ K) = 0.1068 \pm 0.0004$ nm.

In spite of being isostructural to the $[Cu(HF_2)(pyz)_2]X$ systems, the dimensionality of these Ni variants is ambiguous. Susceptibility data fit acceptably to a number of models, and *ab initio* theoretical calculations are suggestive of one-dimensional behaviour, dominated by the exchange along the bifluoride bridges. This is discussed more fully in Ref. 92.

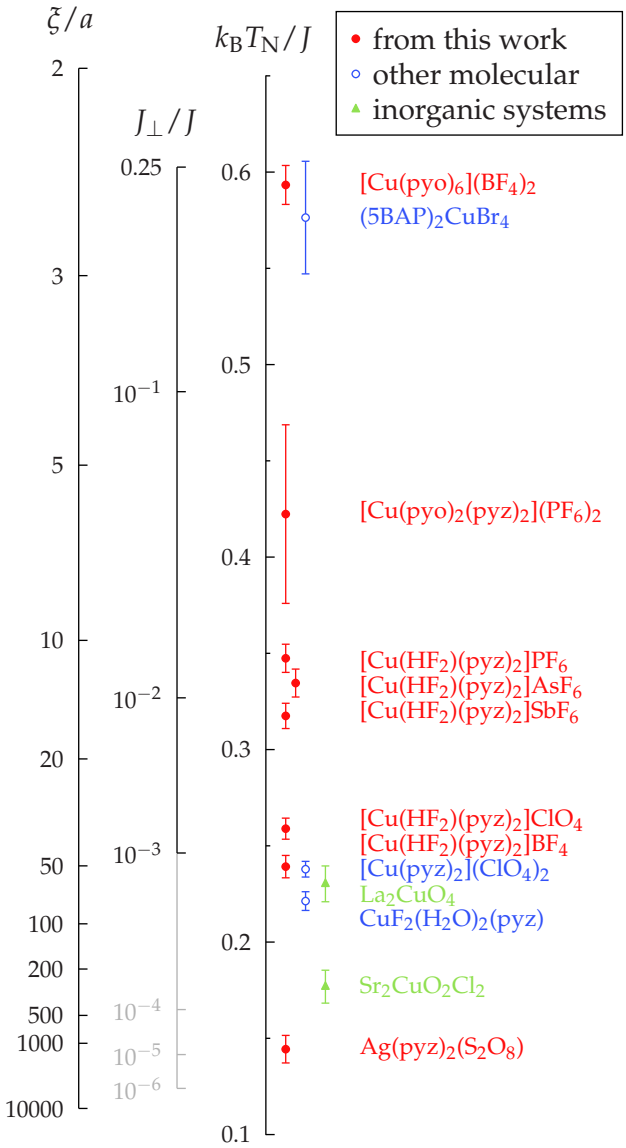

Figure 7.10: Quantification of the two-dimensionality of the materials in this thesis and comparison with other notable 2DSLQHA systems. Filled circles show materials investigated in this thesis; open circles show other molecular materials; and filled triangles show inorganic systems. The low dimensionality is parametrised firstly with the directly experimental ratio T_N/J, and then with predictions derived from quantum Monte Carlo simulations for both the exchange anisotropy, $J_\perp/J$ [Eq. (5.3)], and the correlation length of an ideal 2D Heisenberg antiferromagnet with the measured J at a temperature T_N [Eq. (5.4)]. The greying-out of the axis for $J_\perp/J$ indicates where Eq. (5.3) is extrapolated beyond the range for which it was originally derived [86]. Values of $k_B T_N/J$ for the other materials were evaluated from Refs. 115, 116, 117.

7.5 Discussion

Fig. 7.10 collects the results from this and the preceding chapter and shows how isolation between two-dimensional layers varies over a variety of systems; those presented in this thesis, molecular materials studied elsewhere, and inorganic materials. The primary axis is the experimental ratio $k_B T_N/J$. Also shown are the the ratios of the in-plane and inter-plane exchange interactions, $J_\perp/J$, and the correlation length at the transition, $\xi(T_N)/a$, extracted from fits to quantum Monte Carlo simulations. Of the materials in this thesis, the least anisotropic is $[Cu(pyo)_6](BF_4)_2$, whose low transition temperature is caused by a small exchange constant rather than particularly high exchange anisotropy. Below this, $[Cu(pyo)_2(pyz)_2](PF_6)_2$ exhibits a ratio $k_B T_N/J \approx 0.4$. The members of the $[Cu(HF_2)(pyz)_2]X$ family with octahedral anions have $k_B T_N/J \approx 0.33$, rather more than the $k_B T_N/J \approx 0.25$ shown by their counterparts with tetrahedral anions (as has been noted previously [80]). This makes the latter comparable to highly 2D molecular systems $[Cu(pyz)_2](ClO_4)_2$ and $CuF_2(H_2O)_2(pyz)$, and the cuprate parent compound La_2CuO_4. The prototypical inorganic 2D system $Sr_2CuO_2Cl_2$ exhibits $k_B T_N/J = 0.177 \pm 0.009$, and thus $\xi(T_N)/a = 280 \pm 90$. The most 2D material investigated in these chapters, $Ag(pyz)_2(S_2O_8)$, has $k_B T_N/J = 0.148 \pm 0.006$, implying $\xi(T_N)/a = 1000 \pm 300$, with the added benefit that the magnetic field required to probe its interactions is far closer to the range of fields achievable in the laboratory. By these measures, molecular magnets provide some excellent realisations of the 2DSLQHA, with $Ag(pyz)_2(S_2O_8)$ being the best realisation found to date.

Another method of examining the dimensionality of these systems is to consider their behaviour in the critical region. The critical exponent β is a quantity frequently extracted in studies of magnetic materials, and it is often used to make inferences about the dimensionality of the system under study. In the critical region near a magnetic transition, an order parameter Φ, identical to the (staggered) magnetisation, would be expected to vary as

$$\Phi(T) = \Phi_0 \left(1 - \frac{T}{T_N}\right)^{\beta}. \tag{7.7}$$

In simple, isotropic cases, the value of β depends on the dimensionality of the system, d, and that of the order parameter, D. For example, in the 3D Heisenberg model ($d = 3$, $D = 3$), $\beta = 0.367$, whilst in the 2D Ising model ($d = 2$, $D = 1$), $\beta = \frac{1}{8}$. Since the muon precession frequency is proportional to the local field, it is also proportional to the moment on the magnetic ions in a crystal, and can be used as an effective order parameter. However, Eq. (7.7) would only be expected to hold true in the critical region. The extent of the critical region (defined as that region where simple mean-field theory does not apply) can be parametrised by the Ginzburg temperature T_G, which is related to the transition temperature T_c by [118]

$$\frac{|T_G - T_c|}{T_c} = \left[\left(\frac{\xi}{a}\right)^d \left(\frac{\Delta C}{k_B}\right)\right]^{\frac{2}{d-4}}, \tag{7.8}$$

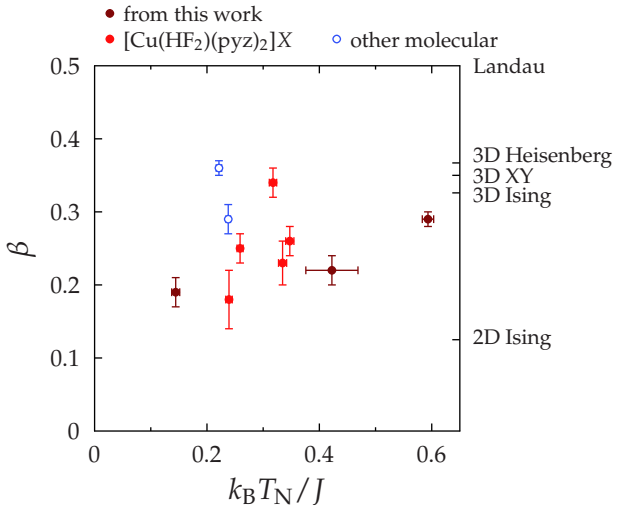

Figure 7.11: Critical exponent β, as commonly extracted from Eq. (4.3), plotted against the experimental ratio $k_B T_N/J$, indicative of exchange anisotropy. Bright filled circles indicate $[Cu(HF_2)(pyz)_2]X$ materials examined in Chapter 6, whilst darker circles indicate other materials studied in this work: $[Cu(pyz)_2(pyo)_2]BF_4$ (Sec. 7.1); $[Cu(pyo)_6](BF_4)_2$ (Sec. 7.2); $Ag(pyz)_2(S_2O_8)$ (Sec. 7.3). Open circles indicate other molecular materials: $CuF_2(H_2O)_2(pyz)$ (Ref. 119); $[Cu(pyz)_2](ClO_4)_2$ (Ref. 82).

where d is the dimensionality, ξ is the correlation length and ΔC is the discontinuity in the heat capacity. Quantum Monte Carlo simulations suggest [78] that $\Delta C/k_B \approx J_\perp/J$. It follows that for $d = 3$, where $\Delta C/k_B \approx 1$ we have $|T_G - T_c|/T_c \approx (\xi/a)^{-6}$, giving rise to a narrow critical region. In two dimensions, we have $|T_G - T_c|/T_c \approx (\xi/a)^{-2}(\Delta C/k_B)^{-1}$. Anisotropic materials with small $J_\perp/J$ only show a small heat capacity discontinuity, while ξ/a grows according to Eq. (5.4). This leads to a $|T_G - T_c|/T_c$ of order 1 for our materials, that is, a larger critical region for 2D (as compared to 3D) systems.

The large critical region in these materials allows meaningful critical parameters to be extracted from muon data. The simplest method of doing so is to fit the data to Eq. (4.3), as has been performed throughout this thesis; alternatively, critical scaling plots can be used (e.g. Ref. 93), which have been performed; the results of these were found to be unchanged within error. Since β might be expected to give an indication of the dimensionality of the hydrodynamical fluctuations in these materials, a comparison between extracted β and exchange anisotropy parametrised by $k_B T_N/J$ is shown in Fig. 7.11. Members of the $[Cu(HF_2)(pyz)_2]X$ family show some correlation between the critical exponent and the effective dimensionality but overall, the relationship is weak. This is probably because β, which is not a Hamiltonian parameter, is not simply a function of the dimensionality of the interactions, but probes the nature of the critical dynamics (including propagating and diffusive modes) which could differ substantially between systems.

7.6 Conclusions

A systematic study has been presented of muon-spin relaxation measurements on several families of quasi two-dimensional molecular antiferromagnet, comprising ligands of pyrazine, bifluoride and pyridine-*N*-oxide; and the magnetic metal cations Cu^{2+}, Ag^{2+} and Ni^{2+}. In each case μ^+SR has been shown to be sensitive to the transition temperature T_N, which is often difficult to unambiguously identify with specific heat and magnetic susceptibility measurements. These measurements have been combined with predictions of quantum Monte Carlo calculations to identify the extent to which each is a good realisation of the 2DSLQHA model. The critical parameters derived from following the temperature evolution of the μ^+SR precession frequencies do not show a strong correlation with the degree of isolation of the 2D magnetic layers.

The analysis of magnetic ordering in zero applied field in terms of inter-layer coupling $J_\perp$ presented here does not take into account the effect of single-ion–type anisotropy on the magnetic order. This has been suggested to be important close to T_N in several examples of 2D molecular magnet [84] where it causes a crossover to *XY*-like behaviour. In fact, its influence is confirmed in the nonmonotonic *B*–*T* phase diagram seen in $[Cu(HF_2)(pyz)_2]BF_4$. It is likely that this is one factor that determines the ordering temperature of a system, although, as shown in Ref. 84, it is a smaller effect than the interlayer coupling parametrised by $J_\perp$. The future synthesis of single crystal samples of these materials will allow the measurement of the single-ion anisotropies for the materials studied here.

The presence of muon–fluorine dipole–dipole oscillations allows the determination of some muon sites in these materials, although it appears from our results that these are not the sites that give rise to magnetic oscillations. However, the Fμ signal has been shown to be useful in identifying transitions at temperatures well above the magnetic ordering transition, which appear to have a structural origin. The fluorine oscillations hamper the study of dynamic fluctuations above T_N, which often appear as a residual relaxation on top of the dominant nuclear relaxation. It may be possible in future to use RF radiation to decouple the influence of the fluorine from the muon ensemble to allow muons to probe the dynamics.

The muon-spin precession signal, upon which much of the analysis presented here is based, is seen most strongly in the materials containing Cu^{2+} and is more heavily relaxed in the Ni^{2+} materials. This is likely due to the larger spin value in the Ni-containing materials. This is borne out by measurements on pyz-based materials containing Mn and Fe ions [120], where no oscillations are observed, despite the presence of magnetic order shown unambiguously by other techniques. In the case of Mn-containing materials, magnetic order is found with μ^+SR through a change in relative amplitudes of relaxing signals due to a differerence in the nature of the relaxation on either side of the transition. It is likely, therefore, that muon studies of molecular magnetic materials containing ions with small spin quantum numbers will be most fruitful in the future.

Finally, the temperature dependence of the relaxation rates in these materials has been shown to be quite complex, reflecting the variety of muon sites in these systems. In favourable cases these data could be used to probe critical behaviour,

such as critical slowing down, although the unambiguous identification of such behaviour may be problematic.

Despite these limitations on the use of μ^+SR in examining molecular magnetic systems of the type studied here, it is worth stressing that the technique still appears uniquely powerful in providing insights into the magnetic behaviour of these materials and will certainly be useful in the future as a wealth of new systems are synthesised and the goal of microscopically engineering such materials is approached.

Appendix A

Ewald summation

Ewald summation [32] is a method of rapidly evaluating fields at positions in an infinite lattice. It involves performing two sums, the first in real space over a lattice which has had an artificial screening added to reduce the importance of long-range interactions, and the second in reciprocal space. The screening in real space reduces the number of poles which need to be summed over and, even after the additional computational effort required to perform the reciprocal space sum is taken into account, this significantly improves the efficiency of the calculation.

First, Madelung constants are described which, though they are not directly relevant to the ultimate goal of magnetic dipole field simulation, provide a more comprehensible system in which to explain the process of Ewald summation. Then, the Madelung constant of sodium chloride is investigated and used to illustrate the problem of conditional convergence. Ewald summation is presented as a solution to this issue, and its generalisation to other quantities, specifically dipole fields, is then briefly explored.

A.1 Madelung constants

The *Madelung energy* [121] of a crystal is the electrostatic potential energy of an ion within it. This is dependent on the charges on and configuration of the ions which surround it. Evaluating it for an ion i requires performing the sum

$$E_i = \sum_{j \neq i} \frac{q_i q_j}{4\pi\epsilon_0 r_j}, \tag{A.1}$$

where $q_{i,j}$ are the charges on the i^{th} and j^{th} ions, ϵ_0 is the permittivity of free space, and the index j implies summation over the infinite array of ions in the crystal. In many simple systems where the charges on ions have the same magnitude but may take either sign, the sum can be simplified to

$$E = \frac{q^2}{4\pi\epsilon_0} \sum_{j \neq i} \frac{(\pm)_j}{r_j}, \tag{A.2}$$

	M
sodium chloride (NaCl)	1.747 564 595
cesium chloride (CsCl)	1.762 674 773
zincblende (ZnS)	1.638 055 062

Table A.1: Selected Madelung constants, referred to the nearest-neighbour distance [122].

where $(\pm)_j$ is $+1$ for a positively-charged ion j and -1 if the ion carries negative charge. The *Madelung constant* is then defined as

$$M = \sum_{j \neq i} (\pm)_j \frac{r_0}{r_j}, \tag{A.3}$$

where r_0 is the nearest-neighbour distance in the lattice. It is thus independent of both the crystal dimensions and the units of charge, meaning that one Madelung constant applies to many systems but for a prefactor. Thus defined, the constant must be positive in order for a lattice configuration to be energetically stable.

To take a very simple example, the Madelung constant of a 1D chain of alternating charges can be expressed analytically:

$$\begin{aligned} M &= \sum_{j \neq i} (\pm)_j \frac{r_0}{r_j} \\ &= 2\left(1 - \frac{1}{2} + \frac{1}{3} - \frac{1}{4} + \ldots\right) \\ &= 2 \ln 2 \\ &= 1.386\,294\ldots, \end{aligned} \tag{A.4}$$

where the factor of 2 arises from the fact that the chain of ions extends to infinity in both directions from the central ion, and using the identity $\ln(1+x) = x - \frac{x^2}{2} + \frac{x^3}{3} - \frac{x^4}{4} \ldots$.

A.2 NaCl and conditional convergence

Evaluating Madelung constants for 3D crystals is somewhat more complex. Let us take as an example sodium chloride, and consider evaluating its Madelung constant [122]. (Madelung constants for several common crystal structures are shown in Table A.1.) The NaCl structure comprises two interpenetrating face-centred cubic lattices, one of Na^+ and the other of Cl^- ions. This can be imagined as a simple cubic lattice, with alternating ions on each lattice site, like a three-dimensional chessboard of charge (see Fig. A.1). The Madelung constant must be extracted numerically. However, the algorithm chosen has a curious effect on whether or not it is possible to obtain the answer. An intuitive method for evaluating

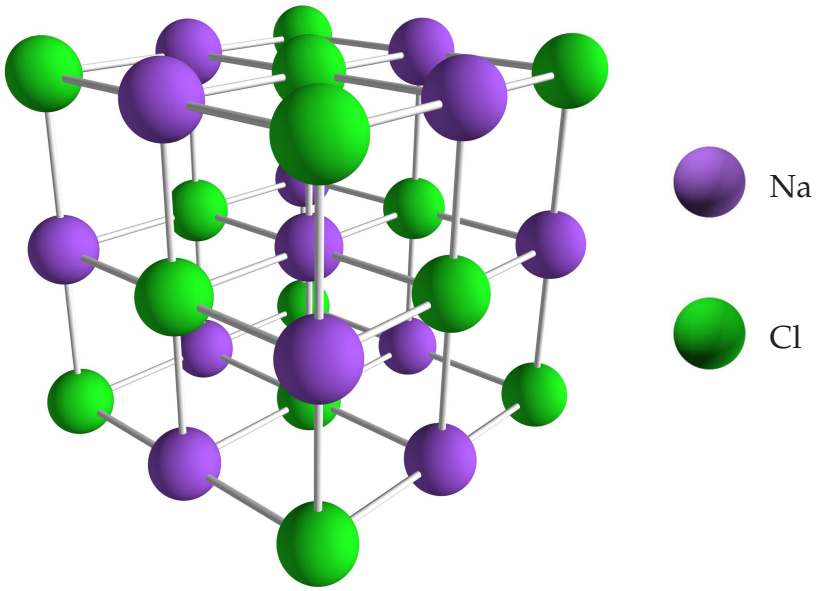

Figure A.1: The structure of sodium chloride.

this sum would be to take spheres of increasing radius about the origin and add up the electrostatic contribution from each new shell of ions. Since ions at larger radii contribute less to the potential energy, it seems logical that the contribution from each successive shell should fall off and, with sufficiently large radius, an accurate answer might be obtained. However, this procedure does not result in a converging series—it has, in fact, been shown mathematically that this series *never* converges [123]. If you instead add up successive cubic shells centred on the origin, the series does converge on the correct answer [123] (as shown in Fig. A.2). This phenomenon, where convergence is contingent on the order in which you add the terms in a given series, is known as *conditional convergence* [124].

In the case of the sodium chloride lattice sum, the additional condition which needs to be satisfied in order to extract the correct lattice constant is charge neutrality, and charges in concentric spherical shells very rarely cancel out precisely. However, in cases where this is approached, so too is the correct value of the Madelung constant: the $342\,648^{\text{th}}$ term in the infinite sum over spherical shells has a net charge of 2, and the calculated Madelung constant is 1.748 042 464, relatively close to the correct value [122].

As well as being a mathematical curiosity, conditional convergence is a potential hazard in performing any lattice sum: experimentation with a variety of summation methodologies would be required to have any assurance that, if convergence were achieved at all, the answer arrived at was correct. Worse, those sums which do converge often do so very slowly; with long-range interactions which fall off as $1/r$, many terms in the sum must be evaluated for every additional decimal place of accuracy. These issues can be overcome by introducing Ewald summation.

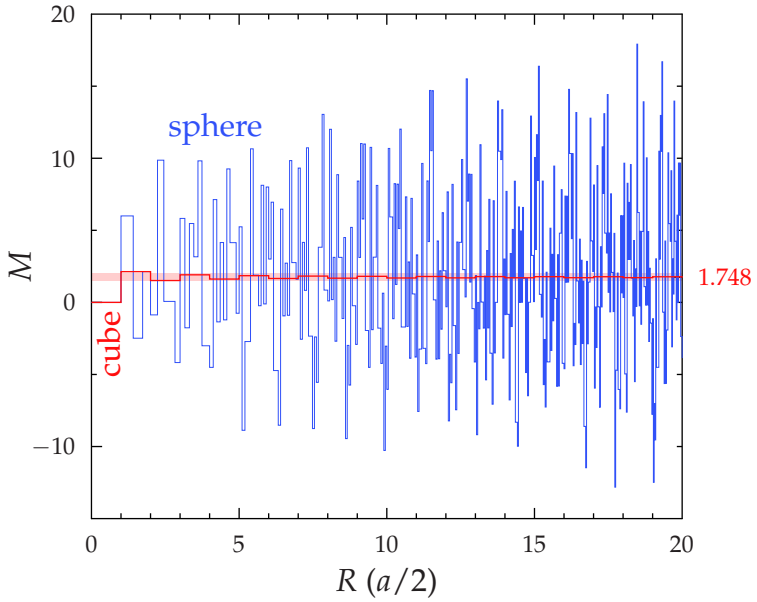

Figure A.2: Conditional convergence in the Madelung constant for sodium chloride. Summing over successive spherical shells fails to cause the series to converge, but the true value is arrived at relatively quickly if cubic sections are considered instead. The calculated value for the Madelung constant, M, is shown against the radius of the sphere, or half-edge of the cube, R in terms of nearest-neighbour distances, equal to half the cubic lattice constant, a. The right y-axis label indicates the true value, $M = 1.748$.

A.3 Ewald summation

Ewald summation [32] splits a sum into two parts—a real space sum, which deals with the short-range part of an interaction, and a reciprocal space sum, which accounts for long-range component. By sharing the load wisely between these two different sums, rapid convergence can be achieved and time spent computing lattice sums much reduced. Another advantage is that, by judicious choice of the *convergence factor* which makes the real-space interactions short-range, the sum can be made *absolutely* and *uniformly* convergent for lattice sums involving spherical shells [124], meaning that choice of summation algorithm is no longer an issue: naïvely using spheres alway works.

Fig. A.3 illustrates the problem for the case of a 1D lattice comprising alternating positive and negative charges. We wish to know the electrostatic potential energy of the central ion in an infinite line of charges. Though this scenario involves a 1D lattice extending to infinity in the $\pm x$ directions, the mathematics which follows is presented in terms of the 3D vector $\boldsymbol{r}$ for generality. We start by defining a charge distribution ρ_i at every lattice site i; simply a δ-function of the appropriate charge q_i located at the site's position $\boldsymbol{r}_i$,

$$\rho_i(\boldsymbol{r}) = q_i \delta(\boldsymbol{r} - \boldsymbol{r}_i). \tag{A.5}$$

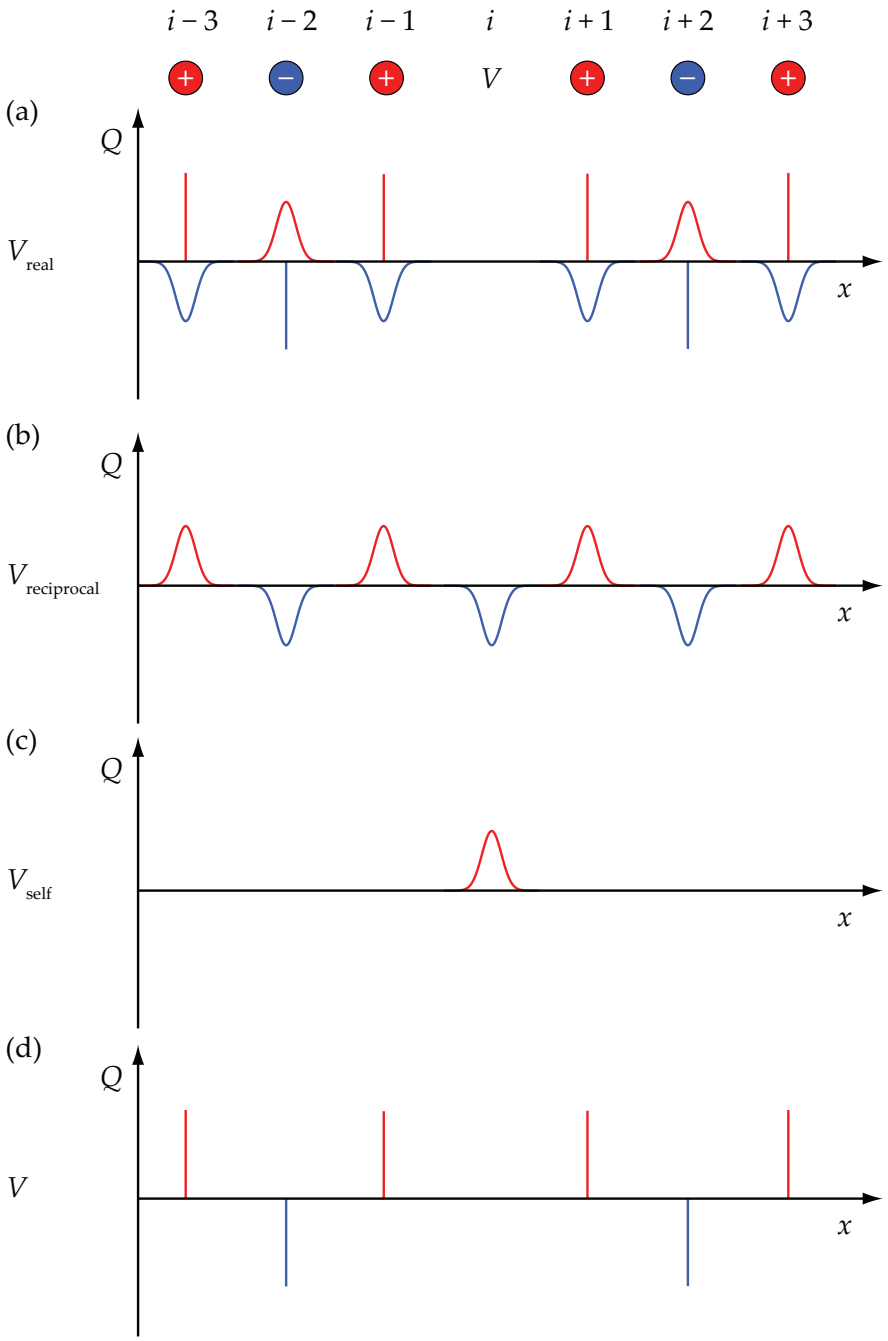

Figure A.3: The components of an Ewald summation to evaluate the potential of the i^{th} ion at the centre of an infinite 1D chain of alternating charges. All graphs show the electric charge Q as a function of distance x along the chain. (a) The real-space potential V_{real} arises from the delta functions of charge in conjunction with the screening Gaussian distributions of opposite sign. The central ion i is excluded from this sum. (b) The reciprocal space potential, $V_{\text{reciprocal}}$, is summed over an infinite lattice of Gaussians, with opposite sign to those in real space. Being periodic in real space, it is impossible to exclude the central charge i. (c) The self-term, V_{self}, cancels the extraneous Gaussian at i in $V_{\text{reciprocal}}$. (d) The resulting potential V is thus calculated from a charge distribution containing only the original δ-functions.

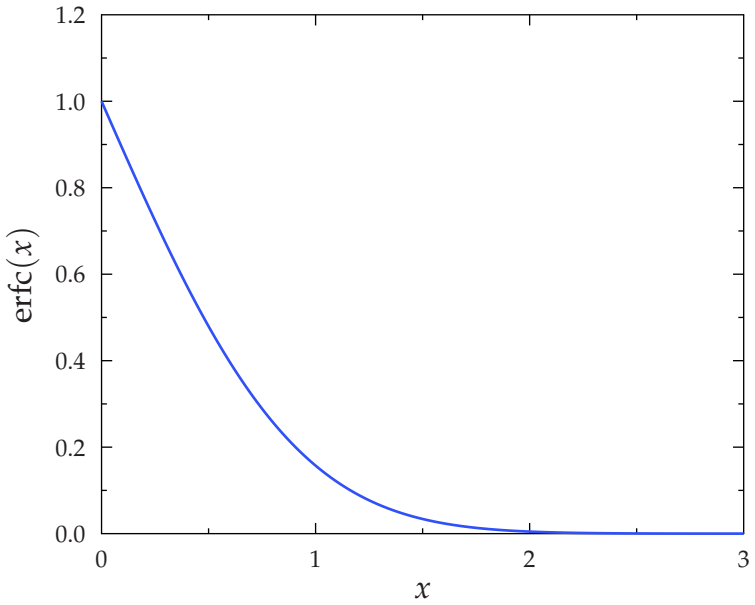

Figure A.4: The complementary error function, $\mathrm{erfc}(x) = (2/\sqrt{\pi}) \int_x^\infty \mathrm{e}^{-s^2} \mathrm{d}s$.

The first stage of Ewald summation is then shown in Fig. A.3 (a): we reduce the range of the interactions in real space by adding screening charge distributions over every ion. A Gaussian screening distribution is usually chosen, though the choice of function is essentially arbitrary. The integral of this Gaussian charge density is identical to that of the δ-function point charge it screens, but is of opposite sign. This means that the net electric charge seen at large distances is zero, thus eliminating long-range interactions. The distribution used is

$$f_i(\boldsymbol{r}) = q_i(\alpha^2/\pi)^{\frac{3}{2}} \mathrm{e}^{-\alpha^2(r-r_i)^2}, \tag{A.6}$$

which means that the Gaussian is defined in terms of a screening parameter α. Higher α implies a narrower Gaussian, more sharply peaked around the δ-function it screens, and therefore shrouds it more effectively.

The modified charge distribution in real space is therefore

$$\rho_i'(\boldsymbol{r}) = q_i\delta(\boldsymbol{r} - \boldsymbol{r}_i) - q_i(\alpha^2/\pi)^{\frac{3}{2}} \mathrm{e}^{-\alpha^2(r-r_i)^2}. \tag{A.7}$$

Evaluating the potential at a point $\boldsymbol{r}$ due to this new distribution now involves three terms: the Coulomb term from the point charge at $\boldsymbol{r}_i$; the charge from the Gaussian inside the sphere centred on $\boldsymbol{r}_i$ with radius $|\boldsymbol{r} - \boldsymbol{r}_i|$, which is equivalent to that charge collapsed onto another δ-function at $\boldsymbol{r}_i$; and the remaining Gaussian charge, outside this sphere. This must then be summed over all ions. Thus,

$$V_{\mathrm{real}} = \sum_{j \neq i} q_j \left(\frac{1}{r_j} - \frac{1}{r_j} \int_0^{r_j} \rho(\boldsymbol{r}) \mathrm{d}\boldsymbol{r} - \int_{r_j}^\infty \frac{\rho(\boldsymbol{r})}{r} \mathrm{d}\boldsymbol{r} \right), \tag{A.8}$$

which simplifies pleasingly to

$$V_{\text{real}} = \sum_{j \neq i} \frac{q_j}{r_j} \text{erfc}(\alpha r_j), \tag{A.9}$$

where the complementary error function $\text{erfc}(x) = (2/\sqrt{\pi}) \int_x^\infty \text{e}^{-s^2} \text{d}s$ (see Fig. A.4). The ion i does not interact with itself, and thus the sum is defined over $j \neq i$. Since $0 < r_j < \infty$, the complementary error function takes values $1 < \text{erfc}(\alpha r_j) < 0$, and premultiplying by it will reduce the Coulombic potential. It is worth emphasising that the Gaussian screening charges and their width as parameterised by α have no physical significance whatsoever—the screening parameter is chosen purely for convenience, with an eye to making sure that the sums converge, and do so as rapidly as possible.

The next stage is to remove the Gaussian distributions, leaving us with the original distribution of point charges we were attempting to sum over. This is shown in Fig. A.3 (b). The reason that this is not an exercise in pointless mathematical circularity is that the lattice of Gaussians can be summed in reciprocal space. Evaluating this sum takes several stages but, by taking Fourier transforms of potential and charge, solving the Poisson equation and then manipulating the resulting expression, a sum in reciprocal space results [125]:

$$V_{\text{reciprocal}} = \frac{4\pi}{\Delta} \sum_{\boldsymbol{G} \neq \boldsymbol{0}} \frac{S(\boldsymbol{G})}{G^2} \text{e}^{\text{i}\boldsymbol{G}\cdot\boldsymbol{r} - G^2/4\alpha^2}, \tag{A.10}$$

where $\Delta = \boldsymbol{a} \cdot \boldsymbol{b} \times \boldsymbol{c}$ is the volume of the primitive unit cell in real space, $\boldsymbol{G}$ are the reciprocal lattice vectors and $S(\boldsymbol{G})$ is the structure factor in units of charge [$S(\boldsymbol{G}) = \sum_p q_p \text{e}^{\text{i}\boldsymbol{G}\cdot\boldsymbol{r}_p}$, where the index p implies summation over the atoms in the primitive unit cell].

Components of a sum in reciprocal space are necessarily periodic in real space, and consequently it is not possible to exclude the Gaussian on the i^{th} atom, which is compensating for a Gaussian which we excluded in the V_{real} term. So, finally, the *self term* must be included, which removes this contribution:

$$V_{\text{self}} = \int_0^\infty (4\pi r^2 \text{d}r)(\rho_i(r)/r) = \frac{2q_i\alpha}{\sqrt{\pi}}. \tag{A.11}$$

This is shown in Fig. A.3 (c).

The resulting formula for the potential on the ion i is, then

$$\begin{aligned} V_i &= V_{\text{real}} + V_{\text{reciprocal}} + V_{\text{self}} \\ &= \sum_{j \neq i} \frac{q_j}{r_j} \text{erfc}(\alpha r_j) + \frac{4\pi}{\Delta} \sum_{\boldsymbol{G} \neq \boldsymbol{0}} \frac{S(\boldsymbol{G})}{G^2} \text{e}^{\text{i}\boldsymbol{G}\cdot\boldsymbol{r} - G^2/4\alpha^2} - \frac{2q_i\alpha}{\sqrt{\pi}}. \end{aligned} \tag{A.12}$$

This can be transformed into a formula for the Madelung constant by referring all distances r to the nearest-neighbour distance r_0. Evaluating the potential at a lattice site is then a question of evaluating these two sums, and the self term. The final distribution of charge being summed over is thus, as shown in Fig. A.3 (d), the same as the original.

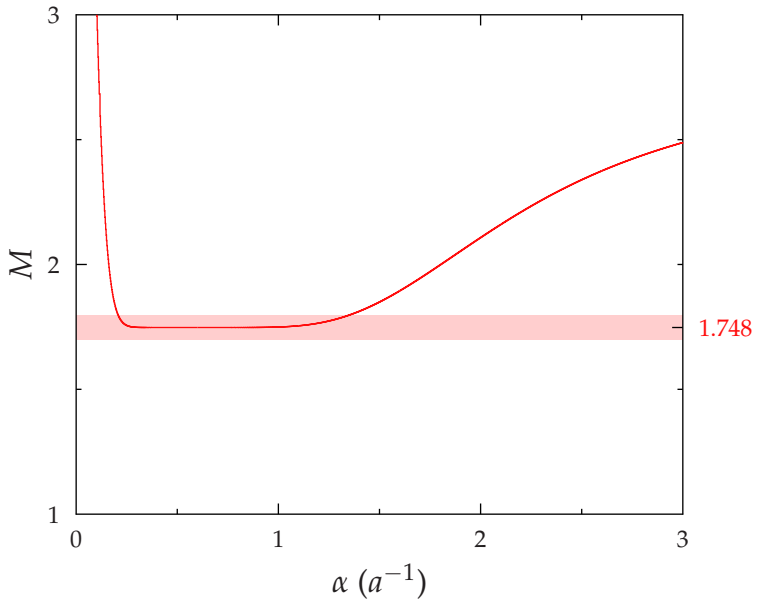

Figure A.5: Optimising an Ewald summation for the 3D NaCl lattice in the screening parameter α. Real space and reciprocal space spheres were fixed at $r_{\text{real}} = 5a$ and $r_{\text{reciprocal}} = 5a^*$, respectively. The sum converges by these sphere sizes for a relatively wide range of α values. The right y-axis label indicates the true value, $M = 1.748$.

As was mentioned above, choice of α is entirely pragmatic—its value is chosen to optimise the computational efficiency of the Ewald sum. Obtaining a result as quickly as possible is then a three-way optimisation between sphere size in real space, sphere size in reciprocal space and convergence parameter α. A large value of α screens real-space charges more effectively, reducing the size of real-space sphere required, but has the opposite effect in reciprocal space. It can be shown that convergence occurs at the same rate in real and reciprocal space when $\alpha = \sqrt{\pi}/a$, where a is the cubic lattice parameter [126]. However, typically the reciprocal-space sum is more computationally efficient, and thus a larger value of α is often chosen to bias the summation to reciprocal space. (As a rule of thumb, α is usually sufficiently large to screen all but the charges in one unit cell in real space.) Various algorithms, such as one in Ref. 127, exist to optimise the three parameters, but their exact values are not crucial because Ewald summations tend to converge in a relatively large region of $(r_{\text{real}}, r_{\text{reciprocal}}, \alpha)$-space. An example optimisation in α is shown in Fig. A.5.

A.4 Ewald summation for dipole-field simulations

In order to make use of Ewald summation for dipole-field simulations, a threefold generalisation of the Ewald method is required. Firstly, the muon will not sit at an atomic site, but at an interatomic position somewhere in the crystal. Generalising Ewald's formula to work out the potential at any position is simple [127]:

1. We now sum over all ions, the $j \neq i$ condition no longer being relevant since we are not at an ion site i.

2. We remove the self-term.

We also need to generalise the sum to work for dipoles rather than monopoles and, further, fields rather than potentials. Ewald summation can be extended to calculate fields, field gradients and so on, and to dipoles or higher-order multipoles. Though the process is conceptually similar to monopole potential Ewald summation, it is rather more mathematically involved. Details can be found in e.g. Refs. 128, 127, 125.

Appendix B

The magnetic propagation vector

The magnetic propagation vector formalism allows compact description of any periodic magnetic structure [129]. Magnetic periodicity often has a lower spatial frequency than crystal translation: even a relatively simple antiferromagnetic structure might be two unit cells in each dimension, creating an eight-fold increase in the number of moments which have to be specified in the magnetic unit cell. The magnetic unit cell becomes infinitely large if the magnetic structure is incommensurate along any axis. This limitation can be circumvented by using magnetic propagation vectors, sometimes referred to as $\boldsymbol{k}$-vectors, which allow large unit cells to be represented as a small number of Fourier components.

The $\boldsymbol{k}$-vector formalism is described in the familiar crystallographic notation. A crystal comprises an infinite array of atoms j at positions $\boldsymbol{R}_j$ each comprising the addition of a lattice translation vector $\boldsymbol{T}_l$ and a basis vector $\boldsymbol{r}_p$:

$$\begin{aligned} \boldsymbol{R}_j &= \boldsymbol{T}_l + \boldsymbol{r}_p \\ &= n_{l_\mathrm{a}}\boldsymbol{a} + n_{l_\mathrm{b}}\boldsymbol{b} + n_{l_\mathrm{c}}\boldsymbol{c} + x_p\boldsymbol{a} + y_p\boldsymbol{b} + z_p\boldsymbol{c}, \end{aligned} \tag{B.1}$$

where $\boldsymbol{a}$, $\boldsymbol{b}$ and $\boldsymbol{c}$ are the three non-coplanar lattice vectors; $n_{l_{\mathrm{a,b,c}}} \in \mathbb{Z}$ index the infinite three-dimensional array of unit cells; and $0 \leq x_p, y_p, z_p < 1$ together describe the fractional coordinates of the atom p in the primitive unit cell. Magnetic order is then superposed using the formalism of Bloch waves, which allows decomposition of any periodic property into a Fourier series. This Fourier series is most easily expressed in terms of reciprocal lattice vectors $\boldsymbol{k}$, whose components are multiples of the three reciprocal lattice vectors

$$\boldsymbol{a}^* = \frac{2\pi}{\Delta}\boldsymbol{b} \times \boldsymbol{c} \tag{B.2}$$

etc., where $\Delta = \boldsymbol{a} \cdot \boldsymbol{b} \times \boldsymbol{c}$ is the volume of the unit cell. Since the crystal properties are periodic in real space, only wavevectors in the first Brillouin zone need to be considered.

In the case of an ordered magnetic system, the periodic property is the atoms' magnetic moments $\boldsymbol{\mu}_j$. These are computed by a Fourier summation

$$\boldsymbol{\mu}_j = \sum_{\{\boldsymbol{k}\}} \boldsymbol{m}_{p,\boldsymbol{k}} e^{-i\boldsymbol{k}\cdot\boldsymbol{T}}, \tag{B.3}$$

where $\boldsymbol{m}_{p,\boldsymbol{k}}$ is the Fourier component with wavevector $\boldsymbol{k}$ corresponding to an atom p in the unit cell. The sum is taken over the set of wavevectors $\{\boldsymbol{k}\}$, as explained below; in many systems, this set consists of a single element. In general, $\boldsymbol{m}_{p,\boldsymbol{k}}$ is a complex vector, but $\boldsymbol{k}$ must be real (though it may be incommensurate with the lattice). An arbitrarily complicated periodic magnetic system can be described with every atom in the primitive unit cell being assigned a unique set of indefinitely many $\boldsymbol{m}_{p,\boldsymbol{k}}$ and $\boldsymbol{k}$ vectors. Thankfully, most systems can be described with fewer parameters than this!

The resulting magnetic moment $\boldsymbol{\mu}_j \in \mathbb{R}^3$ because it represents a physical magnetic moment on the j^{th} atom. However, $\boldsymbol{m}$ and $\boldsymbol{k}$ can be complex vectors, meaning that the Fourier components are in general complex. In non-trivial cases these vectors must be chosen carefully in order to ensure that the resulting magnetic structure contains only real moments.

Elucidating $\boldsymbol{m}$s and $\boldsymbol{k}$s from experimental data, particularly from neutron diffraction, can be done by considering the exchange interactions and symmetry of a system using representational theory [130]; this is beyond the scope of this thesis.

B.1 Examples

Ferromagnetic and simple antiferro- or ferrimagnetic structures can be simply described in this formalism, with a single wavevector $\boldsymbol{k}$ and therefore a single $\boldsymbol{m}_p \equiv \boldsymbol{m}_{p,\boldsymbol{k}} \in \mathbb{R}^3$ for each atom q. In this case, $\boldsymbol{m}_p \equiv \boldsymbol{\mu}_p$; they represent the actual magnetic moments of the atoms in the zeroth unit cell. The wavevector $\boldsymbol{k}$ describes how these moments transform between unit cells. In order that $\boldsymbol{\mu}_j \in \mathbb{R}^3$, the imaginary component of the complex exponential must be zero. This requires values of $\boldsymbol{k}$ such that $\boldsymbol{k}\cdot\boldsymbol{T} = n\pi$, where $n \in \mathbb{Z}$. Eq. (B.3) then reduces to

$$\boldsymbol{\mu}_j = \boldsymbol{m}_p \cos(\boldsymbol{k}\cdot\boldsymbol{T}). \tag{B.4}$$

Since the sine component has vanished, the cosine is necessarily equal to ± 1, and so adjacent moments can either be identical or opposite, and equal in magnitude. In these cases, the propagation vector will inevitably be perpendicular to the planes of ferromagnetism in the material. Simple examples of structures of this type can be seen in Fig. B.1 (a)–(c).

The trivial case, $\boldsymbol{k} = \boldsymbol{0}$, can be used to describe any magnetic system where the spatial and magnetic unit cells are equivalent. Eq. (B.4) simplifies even further to

$$\boldsymbol{\mu}_j = \boldsymbol{m}_p, \tag{B.5}$$

implying that any atom will have the same moment as its equivalent in the zeroth unit cell. Ferromagnets are a subset of this trivial description with the further precondition that mutiple moments within the crystallographic unit cell must be equal in magnitude and direction. It is also possible to envisage antiferro- and

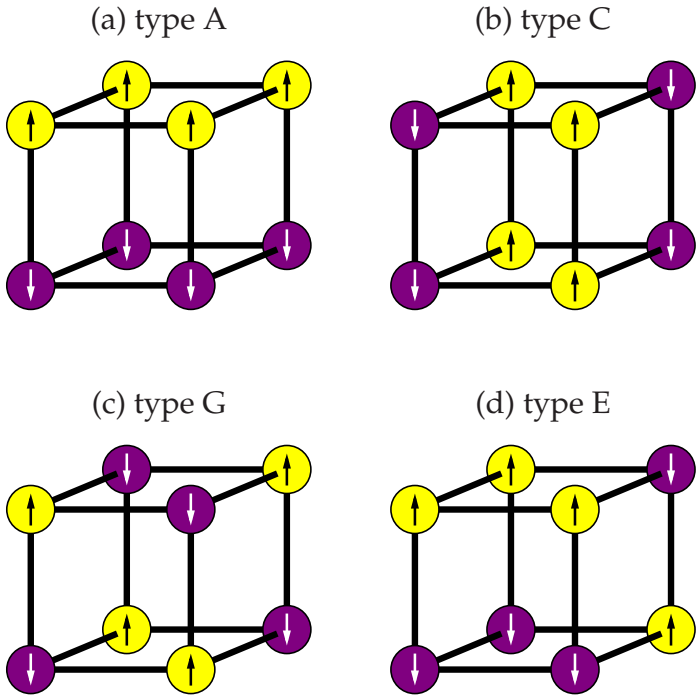

Figure B.1: Four antiferromagnetic structures on a simple cubic lattice with one moment per unit cell [34, 131]. (a), (b) and (c) have simple propagation vectors, perpendicular to planes of ferromagnetism within the material; $\boldsymbol{m}_{\mathrm{a,b,c}} = (0, 0, \mu)$, $\boldsymbol{k}_{\mathrm{a}} = \left(0, 0, \frac{1}{2}\right)$, $\boldsymbol{k}_{\mathrm{b}} = \left(\frac{1}{2}, \frac{1}{2}, 0\right)$, $\boldsymbol{k}_{\mathrm{c}} = \left(\frac{1}{2}, \frac{1}{2}, \frac{1}{2}\right)$. (d) is a 'zig-zag' structure, requiring two propagation vectors and basis vectors to describe: $\boldsymbol{k}^1_{\mathrm{d}} = -\boldsymbol{k}^2_{\mathrm{d}} = \left(\frac{1}{4}, \frac{1}{4}, \frac{1}{2}\right)$, $\boldsymbol{m}_{\mathrm{d},k_1} = \left(0, 0, \frac{1+\mathrm{i}}{2}\mu\right)$, $\boldsymbol{m}_{\mathrm{d},k_2} = \boldsymbol{m}^*_{\mathrm{d},k_1} = \left(0, 0, \frac{1-\mathrm{i}}{2}\mu\right)$.

ferrimagnets with multiple moments per unit cell being described with this trivial propagation vector.

However, the propagation vector formalism can be turned to describing *any* periodic magnetic structure, and is consequently capable of representing significantly more complex examples than these. One slightly more subtle example is shown in Fig. B.1 (d), a zig-zag magnetic structure which does not contain obvious planes of ferromagnetism. This requires two propagation vectors and two corresponding complex basis vectors to specify. It is possible to specify structures with modulated moment size and/or varying moment orientation (e.g. sine structures, helical structures *etc.*) which vary either commensurately or incommensurately with the lattice by appropriate application of propagation vectors [129].

References

[1] S. J. Blundell. Spin-polarized muons in condensed matter physics. *Contemporary Physics* **40**, 3, 175–192 (1999). DOI:10.1080/001075199181521.

[2] S. P. Cottrell C. Johnson. Radio frequency muon spin resonance user guide, www.isis.stfc.ac.uk/groups/muons/radio-frequency-musr-manual7737.pdf.

[3] B. Hitti, S.R. Kreitzman, T.L. Estle, R.L. Lichti and E.C. Lightowlers. Electron–muon dynamics in n-type silicon. *Hyperfine Interactions* **105**, 321–325 (1997). DOI:10.1023/A:1012680127464.

[4] S. Cottrell, S. Cox, J. Lord and C. Scott. Radio-frequency μ^+SR experiments at the ISIS pulsed muon facility. *Applied Magnetic Resonance* **15**, 469–476 (1998). DOI:10.1007/BF03162029.

[5] S. F. J. Cox. Implanted muon studies in condensed matter science. *Journal of Physics C: Solid State Physics* **20**, 22, 3187 (1987). DOI:10.1088/0022-3719/20/22/005.

[6] E. Roduner. Muon spin resonance—a variant of magnetic resonance. *Applied Magnetic Resonance* **13**, 1–14 (1997). DOI:10.1007/BF03161967.

[7] P. Dalmas de Réotier and A. Yaouanc. Muon spin rotation and relaxation in magnetic materials. *Journal of Physics: Condensed Matter* **9**, 43, 9113 (1997). DOI:10.1088/0953-8984/9/43/002.

[8] A. Schenck. *Muon Spin Rotation Spectroscopy: Principles and Applications in Solid State Physics*. Boston (1985). ISBN 0852745516.

[9] Kenzo Nakamura and Particle Data Group. Review of particle physics. *Journal of Physics G: Nuclear and Particle Physics* **37**, 7A, 075021 (2010). DOI:10.1088/0954-3899/37/7A/075021.

[10] R. F. Kiefl, W. A. MacFarlane, G. D. Morris, P. Amaudruz, D. Arseneau, H. Azumi, R. Baartman, T. R. Beals, J. Behr, C. Bommas, J. H. Brewer, K. H. Chow, E. Dumont, S. R. Dunsiger, S. Daviel, L. Greene, A. Hatakeyama, R. H. Heffner, Y. Hirayama, B. Hitti, S. R. Kreitzman, C. D. P. Levy, R. I. Miller, M. Olivo and R. Poutissou. Low-energy spin-polarized radioactive beams as a nano-scale probe of matter. *Physica B: Condensed Matter* **326**, 1-4, 189–195 (2003). DOI:10.1016/S0921-4526(02)01600-9.

[11] G. Audi, O. Bersillon, J. Blachot and A. H. Wapstra. The evaluation of nuclear and decay properties. *Nuclear Physics A* **729**, 1, 3–128 (2003). DOI:10.1016/j.nuclphysa.2003.11.001.

[12] Carl D. Anderson and Seth H. Neddermeyer. Cloud chamber observations of cosmic rays at 4300 meters elevation and near sea-level. *Physical Review* **50**, 4, 263–271 (1936). DOI:10.1103/PhysRev.50.263.

[13] David H. Frisch and James H. Smith. Measurement of the relativistic time dilation using mu-mesons. *American Journal of Physics* **31**, 5, 342–355 (1963). DOI:10.1119/1.1969508.

[14] Richard L. Garwin, Leon M. Lederman and Marcel Weinrich. Observations of the failure of conservation of parity and charge conjugation in meson decays: the magnetic moment of the free muon. *Physical Review* **105**, 4, 1415–1417 (1957). DOI:10.1103/PhysRev.105.1415.

[15] T. D. Lee and C. N. Yang. Question of parity conservation in weak interactions. *Physical Review* **104**, 1, 254–258 (1956). DOI:10.1103/PhysRev.104.254.

[16] W. H. Breunlich, P. Kammel, J. S. Cohen and M. Leon. Muon-catalyzed fusion. *Annual Review of Nuclear and Particle Science* **39**, 1, 311–356 (1989). DOI:10.1146/annurev.ns.39.120189.001523.

[17] Y. Fukuda, T. Hayakawa, E. Ichihara, K. Inoue, K. Ishihara, H. Ishino, Y. Itow, T. Kajita, J. Kameda, S. Kasuga, K. Kobayashi, Y. Kobayashi, Y. Koshio, K. Martens, M. Miura, M. Nakahata, S. Nakayama, A. Okada, M. Oketa, K. Okumura, M. Ota, N. Sakurai, M. Shiozawa, Y. Suzuki, Y. Takeuchi, Y. Totsuka, S. Yamada, M. Earl, A. Habig, J. T. Hong, E. Kearns, S. B. Kim, M. Masuzawa, M. D. Messier, K. Scholberg, J. L. Stone, L. R. Sulak, C. W. Walter, M. Goldhaber, T. Barszczak, W. Gajewski, P. G. Halverson, J. Hsu, W. R. Kropp, L. R. Price, F. Reines, H. W. Sobel, M. R. Vagins, K. S. Ganezer, W. E. Keig, R. W. Ellsworth, S. Tasaka, J. W. Flanagan, A. Kibayashi, J. G. Learned, S. Matsuno, V. Stenger, D. Takemori, T. Ishii, J. Kanzaki, T. Kobayashi, K. Nakamura, K. Nishikawa, Y. Oyama, A. Sakai, M. Sakuda, O. Sasaki, S. Echigo, M. Kohama, A. T. Suzuki, T. J. Haines, E. Blaufuss, R. Sanford, R. Svoboda, M. L. Chen, Z. Conner, J. A. Goodman, G. W. Sullivan, M. Mori, J. Hill, C. K. Jung, C. Mauger, C. McGrew, E. Sharkey, B. Viren, C. Yanagisawa, W. Doki, T. Ishizuka, Y. Kitaguchi, H. Koga, K. Miyano, H. Okazawa, C. Saji, M. Takahata, A. Kusano, Y. Nagashima, M. Takita, T. Yamaguchi, M. Yoshida, M. Etoh, K. Fujita, A. Hasegawa, T. Hasegawa, S. Hatakeyama, T. Iwamoto, T. Kinebuchi, M. Koga, T. Maruyama, H. Ogawa, A. Suzuki, F. Tsushima, M. Koshiba, M. Nemoto, K. Nishijima, T. Futagami, Y. Hayato, Y. Kanaya, K. Kaneyuki, Y. Watanabe, D. Kielczewska, R. Doyle, J. George, A. Stachyra, L. Wai, J. Wilkes

and K. Young. Measurements of the solar neutrino flux from super-Kamiokande's first 300 days. *Physical Review Letters* **81**, 6, 1158–1162 (1998). DOI:10.1103/PhysRevLett.81.1158.

[18] S. H. Kilcoyne and G. H. Eaton. *Muon Science* (1999).

[19] J. Chappert and R.I. Grynszpan. Muons and pions in materials research. North-Holland (1984).

[20] E. Morenzoni, E. M. Forgan, H. Glückler, T. J. Jackson, H. Luetkens, Ch. Niedermayer, T. Prokscha, T.M. Riseman, M. Birke, A. Hofer, J. Litterst, M. Pleines and G. Schatz. Muon spin rotation and relaxation experiments on thin films. *Hyperfine Interactions* **133**, 179–195 (2001).

[21] S. T. Bramwell, S. R. Giblin, S. Calder, R. Aldus, D. Prabhakaran and T. Fennell. Measurement of the charge and current of magnetic monopoles in spin ice. *Nature* **461**, 956–959 (2009). DOI:10.1038/nature08500 arXiv:0907.0956.

[22] S. F. J. Cox. The shallow-to-deep instability of hydrogen and muonium in II–VI and III–V semiconductors. *Journal of Physics: Condensed Matter* **15**, 46, R1727 (2003). DOI:10.1088/0953-8984/15/46/R01.

[23] P. J. C. King, S. P. Cottrell, S. F. J. Cox, G. H. Eaton, A. D. Hillier, J. S. Lord, F. L. Pratt, T. Lancaster and S. J. Blundell. New science with pulsed muons—development ideas at ISIS. *Physica B: Condensed Matter* **326**, 1–4, 260–264 (2003). DOI:10.1016/S0921-4526(02)01622-8.

[24] Tom Lancaster. *Muon-spin rotation and its application to magnetic systems of differing dimensionality*. D.Phil. thesis University of Oxford (2004).

[25] F. L. Pratt. WIMDA: a muon data analysis program for the Windows PC. *Physica B: Condensed Matter* **289-90**, 710–714 (2000). DOI:10.1016/S0921-4526(00)00328-8.

[26] J. Major, J. Mundy, M. Schmolz, A. Seeger, K. Döring, K. Fürderer, M. Gladisch, D. Herlach and G. Majer. Zero-field muon spin rotation in monocrystalline chromium. *Hyperfine Interactions* **31**, 259–264 (1986). DOI:10.1007/BF02401569.

[27] L. P. Le, A. Keren, G. M. Luke, B. J. Sternlieb, W. D. Wu, Y. J. Uemura, J. H. Brewer, T. M. Riseman, R. V. Upasani, L. Y. Chiang, W. Kang, P. M. Chaikin, T. Csiba and G. Grüner. Muon-spin-rotation and relaxation studies in $(TMTSF)_2$-X compounds. *Physical Review B* **48**, 10, 7284–7296 (1993). DOI:10.1103/PhysRevB.48.7284.

[28] R. S. Hayano, Y. J. Uemura, J. Imazato, N. Nishida, T. Yamazaki and R. Kubo. Zero- and low-field spin relaxation studied by positive muons. *Physical Review B* **20**, 3, 850–859 (1979). DOI:10.1103/PhysRevB.20.850.

[29] Michael J. Pitcher, Tom Lancaster, Jack D. Wright, Isabel Franke, Andrew J. Steele, Peter J. Baker, Francis L. Pratt, William Trevelyan Thomas, Dinah R. Parker, Stephen J. Blundell and Simon J. Clarke. Compositional control of the superconducting properties of LiFeAs. *Journal of the American Chemical Society* **132**, 30, 10467–10476 (2010). DOI:10.1021/ja103196c.

[30] ISIS muon instrument comparison, www.isis.stfc.ac.uk/groups/muons/muon-instrument-comparison6972.html.

[31] M. I. J. Probert and A. J. Fisher. Ab initio studies of magnetism in the organic radical p-NPNN. *Journal of Physics: Condensed Matter* **9**, 17, 3635 (1997). DOI:10.1088/0953-8984/9/17/012.

[32] Paul P. Ewald. Die Berechnung optischer und elektrostatischer Gitterpotentiale. *Annalen der Physik* **369**, 3, 253–287 (1921). DOI:10.1002/andp.19213690304.

[33] L. W. McKeehan. Magnetic dipole fields in unstrained cubic crystals. *Physical Review* **43**, 11, 913–923 (1933). DOI:10.1103/PhysRev.43.913.

[34] Stephen J. Blundell. *Magnetism in condensed matter*. Oxford University Press (2001). ISBN 0-19-850591-4.

[35] P. F. Meier. On the hyperfine field values measured at positive muons in metals. *Solid State Communications* **17**, 8, 987–989 (1975). DOI:10.1016/0038-1098(75)90236-7.

[36] Tom Lancaster, Stephen J. Blundell, Francis L. Pratt, C. H. Gardiner, William Hayes and Andrew T. Boothroyd. A μ^+SR study of the rare earth antiferromagnet PrO_2. *Journal of Physics: Condensed Matter* **15**, 49, 8407–8415 (2003). DOI:10.1088/0953-8984/15/49/017.

[37] S. J. Blundell, T. Lancaster, F. L. Pratt, P. J. Baker, W. Hayes, J.-P. Ansermet and A. Comment. Phase transition in the localized ferromagnet EuO probed by μ^+SR. *Physical Review B* **81**, 9, 092407 (2010). DOI:10.1103/PhysRevB.81.092407.

[38] D. Noakes. Numerical modelling of realistic dipole field distributions at muon sites in solids. *Hyperfine Interactions* **31**, 47–52 (1986). DOI:10.1007/BF02401538.

[39] T. Lancaster, S. J. Blundell, F. L. Pratt and M. Kurmoo. μ^+SR studies of the weak ferromagnets $CoCO_3$ and $NiCO_3$. *Physica B: Condensed Matter* **326**, 1-4, 522–526 (2003). DOI:10.1016/S0921-4526(02)01681-2.

[40] T. Lancaster, S. J. Blundell, P. J. Baker, M. L. Brooks, W. Hayes, F. L. Pratt, R. Coldea, T. Sörgel and M. Jansen. Anomalous temperature evolution of the internal magnetic field distribution in the charge-ordered triangular antiferromagnet $AgNiO_2$. *Physical Review Letters* **100**, 1, 017206 (2008). DOI:10.1103/PhysRevLett.100.017206.

[41] Jun Sugiyama, Martin Månsson, Yutaka Ikedo, Tatsuo Goko, Kazuhiko Mukai, Daniel Andreica, Alex Amato, Kingo Ariyoshi and Tsutomu Ohzuku. μ^+SR investigation of local magnetic order in $LiCrO_2$. *Physical Review B* **79**, 18, 184411 (2009). DOI:10.1103/PhysRevB.79.184411.

[42] Stephen J. Blundell. Dipole-field distributions in complex magnetic materials. *Physica B* **404**, 5-7, 581–584 (2009). DOI:10.1016/j.physb.2008.11.126.

[43] Léon Van Hove. The occurrence of singularities in the elastic frequency distribution of a crystal. *Physical Review* **89**, 6, 1189–1193 (1953). DOI:10.1103/PhysRev.89.1189.

[44] J. Brewer, R. Kiefl, J. Carolan, P. Dosanjh, W. Hardy, S. Kreitzman, Q. Li, T. Riseman, P. Schleger, H. Zhou, E. Ansaldo, D. Noakes, L. Le, G. Luke, Y. Uemura, K. Hepburn-Wiley and C. Stronach. Site of the positive muon in $YBa_2Cu_3O_7$. *Hyperfine Interactions* **63**, 177–181 (1991). DOI:10.1007/BF02396001.

[45] Q. Li and J. Brewer. Theoretical study of μ^+site in $YBa_2Cu_3O_x$ site in $YBa_2Cu_3O_x$. *Hyperfine Interactions* **63**, 169–175 (1991). DOI:10.1007/BF02396000.

[46] K. Aggarwal, L. Asch, F. Gygax, O. Hartmann, G. Kalvius, A. Kratzer, F. Litterst, K. Mattenberger, A. Schenck and O. Vogt. A μ^+SR study of UP and UTe. *Hyperfine Interactions* **51**, 933–942 (1989). DOI:10.1007/BF02407805.

[47] C. G. Shull and J. Samuel Smart. Detection of antiferromagnetism by neutron diffraction. *Physical Review* **76**, 1256–1257 (1949). DOI:10.1103/PhysRev.76.1256.2.

[48] Andrew L. Goodwin, Matthew G. Tucker, Martin T. Dove and David A. Keen. Magnetic structure of MnO at 10 K from total neutron scattering data. *Physical Review Letters* **96**, 4, 047209 (2006). DOI:10.1103/PhysRevLett.96.047209.

[49] H. Shaked, J. Faber and R. L. Hitterman. Low-temperature magnetic structure of MnO: a high-resolution neutron-diffraction study. *Physical Review B* **38**, 16, 11901–11903 (1988). DOI:10.1103/PhysRevB.38.11901.

[50] Erik Lidström and Ola Hartmann. Paramagnetic fluctuations in MnO. *Journal of Physics: Condensed Matter* **12**, 23, 4969 (2000). DOI:10.1088/0953-8984/12/23/306.

[51] Y. J. Uemura, T. Yamazaki, Y. Kitaoka, M. Takigawa and H. Yasuoka. Positive muon spin precession in magnetic oxides MnO and V_2O_3; local fields and phase transition. *Hyperfine Interactions* **17–19**, 339–343 (1984). DOI:10.1007/BF02065922.

[52] Y. J. Uemura, J. Imazato, N. Nishida, R. S. Hayano, M. Takigawa and T. Yamazaki. Paramagnetic shift of μ^+ in MnO and its time dependence. *Hyperfine Interactions* **8**, 725–728 (1981). DOI:10.1007/BF01037552.

[53] K. Nishiyama, S. Ohira, W.K. Dawson and W. Higemoto. Low temperature μ^+SR studies in NiO and CoO. *Hyperfine Interactions* **104**, 349–355 (1997). DOI:10.1023/A:1012681305657.

[54] Thomas Bayes and Richard Price. An essay towards solving a problem in the doctrine of chances. by the late Rev. Mr. Bayes, F.R.. Communicated by Mr. Price, in a letter to John Canton, A.M.F.R.S. *Philosophical Transactions* **53**, 370–418 (1763). DOI:10.1098/rstl.1763.0053.

[55] Devinderjit Sivia and John Skilling. *Data Analysis: A Bayesian Tutorial*. OUP 2nd edition (2006). ISBN 978-0-19-856832-2.

[56] A. P. Dawid and J. Mortera. Coherent analysis of forensic identification evidence. *Journal of the Royal Statistical Society. Series B (Methodological)* **58**, 2, 425–443 (1996).

[57] Maarten H. P. Ambaum. Significance tests in climate science. *Journal of Climate* **23**, 22, 5927–5932 (2010). DOI:10.1175/2010JCLI3746.1.

[58] Python programming language, `http://www.python.org/`.

[59] Bilbao crystallographic server, `http://www.cryst.ehu.es/`.

[60] I. David Brown and Brian McMahon. CIF: the computer language of crystallography. *Acta Crystallographica Section B: Structural Science* **58**, 1, 317–324 (2002). DOI:10.1107/S0108768102003464.

[61] POV-Ray: The persistence of vision raytracer, `http://www.povray.org/`.

[62] Andrew J. Steele. MµCalc, `http://andrewsteele.co.uk/mmcalc/`.

[63] J. E. Greedan, D. B. Willson and T. E. Haas. Metallic nature of osmium dioxide. *Inorganic Chemistry* **7**, 11, 2461–2463 (1968). DOI:10.1021/ic50069a059.

[64] Katharine E. Stitzer, Mark D. Smith and Hans-Conrad zur Loye. Crystal growth of Ba_2MOsO_6 (M = Li, Na) from reactive hydroxide fluxes. *Solid State Sciences* **4**, 3, 311–316 (2002). DOI:10.1016/S1293-2558(01)01257-2.

[65] Katharine E. Stitzer, Ahmed El Abed, Mark D. Smith, Matthew J. Davis, Seung-Joo Kim, Jacques Darriet and Hans-Conrad zur Loye. Crystal growth of novel osmium-containing triple perovskites. *Inorganic Chemistry* **42**, 4, 947–949 (2003). DOI:10.1021/ic026124p.

[66] A. S. Erickson, S. Misra, G. J. Miller, R. R. Gupta, Z. Schlesinger, W. A. Harrison, J. M. Kim and I. R. Fisher. Ferromagnetism in the Mott insulator Ba_2NaOsO_6. *Physical Review Letters* **99**, 1, 016404 (2007). DOI:10.1103/PhysRevLett.99.016404.

[67] Arthur W. Sleight, John Longo and Roland Ward. Compounds of osmium and rhenium with the ordered perovskite structure. *Inorganic Chemistry* **1**, 2, 245–250 (1962). DOI:10.1021/ic50002a010.

[68] H. J. Xiang and M.-H. Whangbo. Cooperative effect of electron correlation and spin–orbit coupling on the electronic and magnetic properties of Ba_2NaOsO_6. *Physical Review B* **75**, 5, 052407 (2007). DOI:10.1103/PhysRevB.75.052407.

[69] K.-W. Lee and W. E. Pickett. Orbital-quenching–induced magnetism in Ba_2NaOsO_6. *Europhysics Letters* **80**, 3, 37008 (2007). DOI:10.1209/0295-5075/80/37008.

[70] Andrew J. Steele, Peter J. Baker, Tom Lancaster, Francis L. Pratt, Isabel Franke, Saman Ghannadzadeh, Paul A. Goddard, William Hayes, D. Prabhakaran, and Stephen J. Blundell. Low-moment magnetism in the double perovskites Ba_2MOsO_6 (M = Li, Na). *Physical Review B* **84**, 144416 (2011). DOI:10.1103/PhysRevB.84.144416 arXiv:1103.1039.

[71] M. A. B. Whitaker. Exact expressions for ferromagnetic magnetization in the mean field theory. *American Journal of Physics* **57**, 1, 45–47 (1989). DOI:10.1119/1.15865.

[72] M. D. Kuz'min. Landau-type parametrization of the equation of state of a ferromagnet. *Physical Review B* **77**, 18, 184431 (2008). DOI:10.1103/PhysRevB.77.184431.

[73] M. L. Brooks, S. J. Blundell, T. Lancaster, W. Hayes, F. L. Pratt, P. P. C. Frampton and P. D. Battle. Unconventional magnetic properties of the weakly ferromagnetic metal $BaIrO_3$. *Physical Review B* **71**, 22, 220411 (2005). DOI:10.1103/PhysRevB.71.220411.

[74] Andrew J. Steele, Tom Lancaster, Stephen J. Blundell, Peter J. Baker, Francis L. Pratt, Chris Baines, Marianne M. Conner, Heather I. Southerland, Jamie L. Manson and John A. Schlueter. Magnetic order in quasi–two-dimensional molecular magnets investigated with muon-spin relaxation. *Physical Review B* (page 064412) (2011). DOI:10.1103/PhysRevB.84.064412 arXiv:1104.3505.

[75] Efstratios Manousakis. The spin-$\frac{1}{2}$ Heisenberg antiferromagnet on a square lattice and its application to the cuprous oxides. *Reviews of Modern Physics* **63**, 1, 1–62 (1991). DOI:10.1103/RevModPhys.63.1.

[76] N. D. Mermin and H. Wagner. Absence of ferromagnetism or antiferromagnetism in one- or two-dimensional isotropic Heisenberg models. *Physical Review Letters* **17**, 22, 1133–1136 (1966). DOI:10.1103/PhysRevLett.17.1133.

[77] V. L. Berezinskii. *Sov. Phys. JETP* **32**, 493 (1971).

[78] Pinaki Sengupta, Anders W. Sandvik and Rajiv R. P. Singh. Specific heat of quasi–two-dimensional antiferromagnetic Heisenberg models with varying interplanar couplings. *Physical Review B* **68**, 9, 094423 (2003). DOI:10.1103/PhysRevB.68.094423.

[79] Stephen J. Blundell, Tom Lancaster, Francis L. Pratt, Peter J. Baker, Michael L. Brooks, Christopher Baines, Jamie L. Manson and Christopher P. Landee. μ^+SR as a probe of anisotropy in low-dimensional molecular magnets. *Journal of Physics and Chemistry of Solids* **68**, 11, 2039–2043 (2007). DOI:10.1016/j.jpcs.2007.08.042.

[80] P. A. Goddard, J. Singleton, P. Sengupta, R. D. McDonald, T. Lancaster, S. J. Blundell, F. L. Pratt, S. Cox, N. Harrison, J L Manson, H I Southerland and J A Schlueter. Experimentally determining the exchange parameters of quasi–two-dimensional Heisenberg magnets. *New Journal of Physics* **10**, 8, 083025 (2008). DOI:10.1088/1367-2630/10/8/083025.

[81] T. Lancaster, S. J. Blundell, M. L. Brooks, P. J. Baker, F. L. Pratt, J. L. Manson, C. P. Landee and C. Baines. Magnetic order in the quasi-one-dimensional spin-$\frac{1}{2}$ molecular chain compound copper pyrazine dinitrate. *Physical Review B* **73**, 2, 020410 (2006). DOI:10.1103/PhysRevB.73.020410.

[82] T. Lancaster, S. J. Blundell, M. L. Brooks, P. J. Baker, F. L. Pratt, J. L. Manson, M. M. Conner, F. Xiao, C. P. Landee, F. A. Chaves, S. Soriano, M. A. Novak, T. P. Papageorgiou, A. D. Bianchi, T. Herrmannsdorfer, J. Wosnitza and J. A. Schlueter. Magnetic order in the $S = \frac{1}{2}$ two-dimensional molecular antiferromagnet copper pyrazine perchlorate $Cu(Pz)_2(ClO_4)_2$. *Physical Review B* **75**, 9, 094421 (2007). DOI:10.1103/PhysRevB.75.094421.

[83] Stephen J. Blundell and Francis L. Pratt. Organic and molecular magnets. *Journal of Physics: Condensed Matter* **16**, 24, R771 (2004). DOI:10.1088/0953-8984/16/24/R03.

[84] F. Xiao, F. M. Woodward, C. P. Landee, M. M. Turnbull, C. Mielke, N. Harrison, T. Lancaster, S. J. Blundell, P. J. Baker, P. Babkevich and F. L. Pratt. Two-dimensional XY behavior observed in quasi–two-dimensional quantum Heisenberg antiferromagnets. *Physical Review B* **79**, 13, 134412 (2009). DOI:10.1103/PhysRevB.79.134412.

[85] P. Sengupta, C. D. Batista, R. D. McDonald, S. Cox, J. Singleton, L. Huang, T. P. Papageorgiou, O. Ignatchik, T. Herrmannsdörfer, J. L. Manson, J. A. Schlueter, K. A. Funk and J. Wosnitza. Non-monotonic field dependence of the Néel temperature in the quasi-two-dimensional magnet $[Cu(HF_2)(pyz)_2]BF_4$. *Physical Review B* **79**, 6, 060409 (2009). DOI:10.1103/PhysRevB.79.060409.

[86] C. Yasuda, S. Todo, K. Hukushima, F. Alet, M. Keller, M. Troyer and H. Takayama. Néel temperature of quasi–low-dimensional Heisen-

berg antiferromagnets. *Physical Review Letters* **94**, 21, 217201 (2005). DOI:10.1103/PhysRevLett.94.217201.

[87] Peter Hasenfratz and Ferenc Niedermayer. The exact correlation length of the antiferromagnetic $d = 2 + 1$ Heisenberg model at low temperatures. *Physics Letters B* **268**, 2, 231–235 (1991). DOI:10.1016/0370-2693(91)90809-5.

[88] B. B. Beard, R. J. Birgeneau, M. Greven and U.-J. Wiese. Square-lattice Heisenberg antiferromagnet at very large correlation lengths. *Physical Review Letters* **80**, 8, 1742–1745 (1998). DOI:10.1103/PhysRevLett.80.1742.

[89] M. A. Kastner, R. J. Birgeneau, G. Shirane and Y. Endoh. Magnetic, transport, and optical properties of monolayer copper oxides. *Reviews of Modern Physics* **70**, 3, 897–928 (1998). DOI:10.1103/RevModPhys.70.897.

[90] Jamie L. Manson, Marianne M. Conner, John A. Schlueter, Tom Lancaster, Stephen J. Blundell, Michael L. Brooks, Francis L. Pratt, Thomas Papageorgiou, Andreas D. Bianchi, Jochen Wosnitza and Myung-Hwan Whangbo. $[Cu(HF_2)(pyz)_2]BF_4$ (pyz = pyrazine): long-range magnetic ordering in a pseudo-cubic coordination polymer comprised of bridging HF_2^- and pyrazine ligands. *Chemical Communications* , 47, 4894–4896 (2006). DOI:10.1039/b608791d.

[91] Jamie L. Manson, John A. Schlueter, Kylee A. Funk, Heather I. Southerland, Brendan Twamley, Tom Lancaster, Stephen J. Blundell, Peter J. Baker, Francis L. Pratt, John Singleton, Ross D. McDonald, Paul A. Goddard, Pinaki Sengupta, Cristian D. Batista, Letian Ding, Changhoon Lee, Myung-Hwan Whangbo, Isabel Franke, Susan Cox, Chris Baines and Derek Trial. Strong h···f hydrogen bonds as synthons in polymeric quantum magnets: Structural, magnetic, and theoretical characterization of $[Cu(HF_2)(pyrazine)_2]SbF_6$, $[Cu_2F(HF)(HF_2)(pyrazine)_4](SbF_6)_2$, and $[CuAg(H_3F_4)(pyrazine)_5](SbF_6)_2$. *Journal of the American Chemical Society* **131**, 19, 6733–6747 (2009). DOI:10.1021/ja808761d.

[92] Jamie L. Manson, Saul H. Lapidus, Peter W. Stephens, Peter K. Peterson, Kimberly E. Carreiro, Heather I. Southerland, Tom Lancaster, Stephen J. Blundell, Andrew J. Steele, Paul A. Goddard, Francis L. Pratt, John Singleton, Yoshimitsu Kohama, Ross D. McDonald, Rico E. Del Sesto, Nickolaus A. Smith, Jesper Bendix, Sergei A. Zvyagin, Jinhee Kang, Changhoon Lee, Myung-Hwan Whangbo, Vivien S. Zapf and Alex Plonczak. Structural, electronic, and magnetic properties of quasi-1D quantum magnets $[Ni(HF_2)(pyz)_2]X$ (pyz = pyrazine; $X = PF_6^-$, SbF_6^-) exhibiting Ni–FHF–Ni and Ni–pyz–Ni spin interactions. *Inorganic Chemistry* **50**, 13, 5990–6009 (2011). DOI:10.1021/ic102532h.

[93] F. L. Pratt, P. J. Baker, S. J. Blundell, T. Lancaster, M. A. Green and M. Kurmoo. Chiral-like critical behavior in the antiferromagnet cobalt glycerolate. *Physical Review Letters* **99**, 1, 017202 (2007). DOI:10.1103/PhysRevLett.99.017202.

[94] T. Lancaster, S. J. Blundell, D. Andreica, M. Janoschek, B. Roessli, S. N. Gvasaliya, K. Conder, E. Pomjakushina, M. L. Brooks, P. J. Baker, D. Prabhakaran, W. Hayes and F. L. Pratt. Magnetism in geometrically frustrated $YMnO_3$ under hydrostatic pressure studied with muon spin relaxation. *Physical Review Letters* **98**, 19, 197203 (2007). DOI:10.1103/PhysRevLett.98.197203.

[95] Tom Lancaster, Stephen J. Blundell, Francis L. Pratt, Michael L. Brooks, Jamie L. Manson, Euan K. Brechin, Cyril Cadiou, David Low, Eric J. L. McInnes and Richard E. P. Winpenny. Muons as a probe of magnetism in molecule-based low dimensional magnets. *Journal of Physics: Condensed Matter* **16**, 40, S4563 (2004). DOI:10.1088/0953-8984/16/40/009.

[96] T. Lancaster, S. J. Blundell, M. L. Brooks, P. J. Baker, F. L. Pratt, J. L. Manson and C. Baines. Muon-spin relaxation study of the spin-$\frac{1}{2}$ molecular chain compound $Cu(HCO_2)_2(C_4H_4N_2)$. *Physical Review B* **73**, 17, 172403 (2006). DOI:10.1103/PhysRevB.73.172403.

[97] A. Amato. Heavy-fermion systems studied by μ^+SR technique. *Reviews of Modern Physics* **69**, 4, 1119–1180 (1997). DOI:10.1103/RevModPhys.69.1119.

[98] T. Lancaster, S. J. Blundell, P. J. Baker, M. L. Brooks, W. Hayes, F. L. Pratt, J. L. Manson, M. M. Conner and J. A. Schlueter. Muon–fluorine entangled states in molecular magnets. *Physical Review Letters* **99**, 26, 267601 (2007). DOI:10.1103/PhysRevLett.99.267601.

[99] T. Lancaster, F. L. Pratt, S. J. Blundell, I. McKenzie and H. E. Assender. Muon–fluorine entanglement in fluoropolymers. *Journal of Physics: Condensed Matter* **21**, 34, 346004 (2009).

[100] J. H. Brewer, S. R. Kreitzman, D. R. Noakes, E. J. Ansaldo, D. R. Harshman and R. Keitel. Observation of muon-fluorine "hydrogen bonding" in ionic crystals. *Physical Review B* **33**, 11, 7813–7816 (1986). DOI:10.1103/PhysRevB.33.7813.

[101] David M. Grant and Robin K. Harris. *Encyclopedia of Nuclear Magnetic Resonance, Volume 9, Advances in NMR*. Wiley (2002). ISBN 9780471490821.

[102] N. Tsyrulin, F. Xiao, A. Schneidewind, P. Link, H. M. Ronnow, J. Gavilano, C. P. Landee, M. M. Turnbull and M. Kenzelmann. Two-dimensional square-lattice $S = \frac{1}{2}$ antiferromagnet $Cu(pz)_2(ClO_4)_2$. *Physical Review B* **81**, 13, 134409 (2010). DOI:10.1103/PhysRevB.81.134409.

[103] M. Reehuis, C. Ulrich, K. Prokeš, A. Gozar, G. Blumberg, Seiki Komiya, Yoichi Ando, P. Pattison and B. Keimer. Crystal structure and high-field magnetism of La_2CuO_4. *Physical Review B* **73**, 14, 144513 (2006). DOI:10.1103/PhysRevB.73.144513.

[104] Sudip Chakravarty, Bertrand I. Halperin and David R. Nelson. Two-dimensional quantum Heisenberg antiferromagnet at low temperatures. *Physical Review B* **39**, 4, 2344–2371 (1989). DOI:10.1103/PhysRevB.39.2344.

[105] Olexei I. Motrunich. Variational study of triangular lattice spin-$\frac{1}{2}$ model with ring exchanges and spin liquid state in κ-$(ET)_2Cu_2(CN)_3$. *Physical Review B* **72**, 4, 045105 (2005). DOI:10.1103/PhysRevB.72.045105.

[106] A. A. Katanin and A. P. Kampf. Spin excitations in La_2CuO_4: Consistent description by inclusion of ring exchange. *Physical Review B* **66**, 10, 100403 (2002). DOI:10.1103/PhysRevB.66.100403.

[107] Francesc Lloret, Giovanni De Munno, Miguel Julve, Juan Cano, Rafael Ruiz and Andrea Caneschi. Spin polarization and ferromagnetism in two-dimensional sheetlike cobalt(II) polymers: $[Co(L)_2(NCS)_2]$ (L = pyrimidine or pyrazine). *Angewandte Chemie International Edition* **37**, 1–2, 135–138 (1998). DOI:10.1002/(SICI)1521-3773(19980202)37:1/2<135::AID-ANIE135>3.0.CO;2-4.

[108] Derek S. Middlemiss, Lorreta M. Lawton, Carole A. Morrison and Chick C. Wilson. Hybrid functional study of the magnetism and electronic structure of a novel coordination polymer: $[Cu(HF_2)(pyz)_2]BF_4$. *Chemical Physics Letters* **459**, 1-6, 119–123 (2008). DOI:10.1016/j.cplett.2008.05.040.

[109] H. A. Algra, L. J. de Jongh and R. L. Carlin. One- and two-dimensional image Heisenberg antiferromagnetism in $Cu(C_5H_5NO)_6(ClO_4)_2$ and $Cu(C_5H_5NO)_6(BF_4)_2$, respectively. *Physica B & C* **93**, 1, 24–34 (1978). DOI:10.1016/0378-4363(78)90107-9.

[110] D. Reinen and S. Krause. Cooperative Jahn–Teller ordering and magnetic structure—pyridine-*N*-oxide complexes of Cu^{2+}: $Cu(ONC_5H_5)_6X_2$ [$X = ClO_4^-$, BF_4^-]. *Solid State Communications* **29**, 10, 691–699 (1979). DOI:10.1016/0038-1098(79)91008-1.

[111] J. S. Wood, C. P. Keijzers, E. De Boer and A. Buttafava. Dynamic and cooperative Jahn–Teller distortions in copper pyridine *N*-oxide complexes, $Cu(pyo)_6X_2$ (X = tetrafluoroborate(1−), perchlorate(1−), and nitrate(1−): structural and EPR studies of pure and zinc-doped systems. *Inorganic Chemistry* **19**, 8, 2213–2225 (1980). DOI:10.1021/ic50210a004.

[112] R. Burriel, A. Lambrecht and R. L. Carlin. Susceptibilities of the two-dimensional Heisenberg antiferromagnet. *Journal of Applied Physics* **67**, 9, 5853–5854 (1990).

[113] Jamie L. Manson, Kevin H. Stone, Heather I. Southerland, Tom Lancaster, Andrew J. Steele, Stephen J. Blundell, Francis L. Pratt, Peter J. Baker, Ross D. McDonald, Pinaki Sengupta, John Singleton, Paul A. Goddard, Changhoon Lee, Myung-Hwan Whangbo, Michelle M. Warter, Charles H. Mielke and Peter W. Stephens. Characterization of the antiferromagnetism in $Ag(pyz)_2(S_2O_8)$ (pyz = pyrazine) with a two-dimensional square lattice of ag^{2+} ions. *Journal of the American Chemical Society* **131**, 13, 4590–4591 (2009). DOI:10.1021/ja9005223.

[114] R. A. Walton and R. W. Matthews. Coordination compounds of silver(II): V. preparation and characterization of new pyrazine and pyrazine carboxylate complexes and some related silver(I), copper(II), cobalt(II), and nickel(II) derivatives. *Inorganic Chemistry* **10**, 7, 1433–1438 (1971). DOI:10.1021/ic50101a023.

[115] F. M. Woodward, C. P. Landee, J. Giantsidis, M. M. Turnbull and C. Richardson. Structure and magnetic properties of $(5BAP)_2CuBr_4$: magneto-structural correlations of layered $S = \frac{1}{2}$ Heisenberg antiferromagnets. *Inorganica Chimica Acta* **324**, 1-2, 324–30 (2001). DOI:10.1016/S0020-1693(01)00671-5.

[116] M. Greven, R. J. Birgeneau, Y. Endoh, M. A. Kastner, M. Matsuda and G. Shirane. Neutron scattering study of the two-dimensional spin $S = 1/2$ square-lattice Heisenberg antiferromagnet $Sr_2CuO_2Cl_2$. *Zeitschrift für Physik B Condensed Matter* **96**, 465–477 (1995). DOI:10.1007/BF01313844.

[117] G. Aeppli, S. M. Hayden, H. A. Mook, Z. Fisk, S.-W. Cheong, D. Rytz, J. P. Remeika, G. P. Espinosa and A. S. Cooper. Magnetic dynamics of La_2CuO_4 and $La_{2-x}Ba_xCuO_4$. *Physical Review Letters* **62**, 17, 2052–2055 (1989). DOI:10.1103/PhysRevLett.62.2052.

[118] Paul M. Chaikin and Tom C. Lubensky. *Principles of Condensed Matter Physics*. Cambridge University Press (1995). ISBN 0521794501.

[119] Jamie L. Manson, Marianne M. Conner, John A. Schlueter, Amber C. McConnell, Heather I. Southerland, Isabelle Malfant, Tom Lancaster, Stephen J. Blundell, Michael L. Brooks, Francis L. Pratt, John Singleton, Ross D. McDonald, Changhoon Lee and Myung-Hwan Whangbo. Experimental and theoretical characterization of the magnetic properties of cuf2(h2o)2(pyz) (pyz = pyrazine): A two-dimensional quantum magnet arising from supersuperexchange interactions through hydrogen bonded paths. *Chemistry of Materials* **20**, 24, 7408–7416 (2008). DOI:10.1021/cm8016566.

[120] T. Lancaster, S. J. Blundell, M. L. Brooks, F. L. Pratt and J. L. Manson. Muon-spin relaxation studies of the low-dimensional molecular compounds $mn(dca)_2(pyz)$ and $fe(ncs)_2(pyz)_2$. *Physica B* **374–375**, 118–121 (2006). DOI:10.1016/j.physb.2005.11.030.

[121] Erwin Madelung. Das elektrische Feld in Systemen von regelmäßig angeordneten Punktladungen. *Physikalische Zeitschrift* **XIX**, 524–533 (1918).

[122] Robert P. Grosso, Justin T. Fermann and William J. Vining. An in-depth look at the Madelung constant for cubic crystal systems. *Journal of Chemical Education* **78**, 9, 1198 (2001). DOI:10.1021/ed078p1198.

[123] David Borwein, Jonathan M. Borwein and Keith F. Taylor. Convergence of lattice sums and madelung's constant. *Journal of Mathematical Physics* **26**, 11, 2999–3009 (1985). DOI:10.1063/1.526675.

[124] S. W. de Leeuw, J. W. Perram and E. R. Smith. Simulation of electrostatic systems in periodic boundary conditions. i. lattice sums and dielectric constants. *Proceedings of the Royal Society of London. A. Mathematical and Physical Sciences* **373**, 1752, 27–56 (1980). DOI:10.1098/rspa.1980.0135.

[125] Charles Kittel. *Introduction to solid state physics*. Wiley 9th edition (2005).

[126] B.R.A. Nijboer and F.W. De Wette. On the calculation of lattice sums. *Physica* **23**, 1-5, 309–321 (1957). DOI:10.1016/S0031-8914(57)92124-9.

[127] William Smith. Point multipoles in the Ewald summation (revisited). *CCP5 Newsletter* , 46, 18 (1998).

[128] Thomas M. Nymand and Per Linse. Ewald summation and reaction field methods for potentials with atomic charges, dipoles, and polarizabilities. *The Journal of Chemical Physics* **112**, 14, 6152–6160 (2000). DOI:10.1063/1.481216.

[129] A. Wills. Magnetic structures and their determination using group theory. *Journal de Physique IV* **11**, Pr9–133–Pr9–158 (2001). DOI:10.1051/jp4:2001906.

[130] Andrew S. Wills. Symmetry in the solid state; working beyond the space group. *Journal of Materials Chemistry* **15**, 245–252 (2005). DOI:10.1039/B404156A.

[131] J. B. Goodenough. *Magnetism and the chemical bond*. Wiley (1963).